POLITECNICO
MILANO 1863

SCUOLA DI INGEGNERIA INDUSTRIALE
E DELL'INFORMAZIONE

Space Weather Data Processing and Impact on Critical Systems

Tesi di Laurea Magistrale in
Space Engineering - Ingegneria Spaziale

Author: **José Manuel Muñoz Díaz**

Student ID: 276257
Advisor: Prof. Pierluigi di Lizia
Co-advisors: Aurora López Rubio, Ángel Gallego Torrego
Academic Year: 2025-26

This research was carried out at GMV during an internship program. © The copyright of this document is vested in GMV. The publication of this document is hereby authorised by GMV.

Abstract

Space Weather describes the physical and phenomenological conditions of the Sun, the interplanetary medium and the near-Earth environment that may affect technological and biological systems. The increasing dependence of modern society on space and ground-based infrastructures makes the monitoring and assessment of Space Weather impacts operationally essential. This thesis addresses the integration of available measurements, physical models and risk indicators into practical tools capable of evaluating these impacts both retrospectively and in near-real time.

Three complementary tools have been developed. The first one estimates effective radiation dose rates at flight altitudes caused by Space Weather phenomena, deriving operational indicators for aviation support. The tool operates in near-real time and for post-flight analysis, providing dose estimations within defined altitude limits.

The second tool evaluates internal and surface charging risks in geostationary orbit using satellite electron flux measurements. Internal charging is associated with high energy electron fluxes, while surface charging relates to low energy fluxes. A real-time mode produces internal charging risk assessment, and a long-term mode supports anomaly characterization.

The third tool estimates local geomagnetic disturbance levels through the computation of K indices from geomagnetic data measured by stations distributed around the world. The results show that reliable local K estimations can be obtained within defined latitudinal bounds.

Overall, this work demonstrates the feasibility of integrating heterogeneous Space Weather data and models. The main contribution lies in the design and validation of flexible tools capable of supporting both scientific analysis and practical risk awareness.

Keywords: Space Weather, Space Weather Impacts, Aviation Radiation Dose, Geostationary Satellite Charging, Geomagnetic Disturbances

Sommario

La meteorologia spaziale o Space Weather descrive le condizioni fisiche e fenomenologiche del Sole, del mezzo interplanetario e dell'ambiente circumterrestre che possono influenzare sistemi tecnologici e biologici. La crescente dipendenza della società moderna da infrastrutture spaziali e terrestri rende il monitoraggio e la valutazione degli impatti dello Space Weather operativamente essenziali. Questa tesi affronta l'integrazione di misure disponibili, modelli fisici e indicatori di rischio nello sviluppo di strumenti pratici in grado di valutare tali impatti sia in modalità retrospettiva sia in tempo quasi reale.

Sono stati sviluppati tre strumenti complementari. Il primo stima i ratei di dose efficace alle quote di volo causati da fenomeni di Space Weather, derivando indicatori operativi a supporto dell'aviazione. Lo strumento opera sia in tempo quasi reale sia per analisi post-volo, fornendo stime di dose entro limiti di quota definiti.

Il secondo strumento valuta il rischio di carica interna e superficiale in orbita geostazionaria sulla base di misure del flusso di elettroni satellitari. La carica interna è associata a flussi di elettroni ad alta energia, mentre la carica superficiale è correlata a flussi a bassa energia. Una modalità in tempo reale consente la valutazione del rischio di carica interna, mentre una modalità di analisi a lungo termine supporta la caratterizzazione di eventuali anomalie.

Il terzo strumento stima il livello locale di disturbo geomagnetico mediante il calcolo degli indici K a partire da dati geomagnetici misurati da stazioni distribuite a livello globale. I risultati mostrano che è possibile ottenere stime affidabili dell'indice K locale entro determinati limiti latitudinali.

Nel complesso, il lavoro dimostra la fattibilità dell'integrazione di dati e modelli eterogenei di Space Weather. Il contributo principale risiede nella progettazione e validazione di strumenti flessibili, capaci di supportare sia l'analisi scientifica sia la consapevolezza operativa del rischio.

Parole chiave: Space Weather, Meteorologia spaziale, Impatti dello Space Weather, Radiazione in aviazione, Carica satellitare in GEO, Disturbi geomagnetici

Contents

Abstract i

Sommario iii

Contents v

1 Introduction 1

2 Literature review 3

2.1 Space Weather overview . . . 3
2.1.1 Solar cycle and solar activity . . . 3
2.1.2 Earth's magnetosphere . . . 5
2.1.3 The Van Allen radiation belts . . . 5
2.2 Space Weather phenomena and NOAA scales . . . 6
2.2.1 Geomagnetic storms and G-Scale . . . 7
2.2.2 Radio blackouts and R-Scale . . . 9
2.2.3 Solar radiation storms and S-Scale . . . 10
2.2.4 Galactic cosmic rays (GCR) . . . 10
2.2.5 Ground level enhancements (GLE) . . . 11
2.3 Radiation dose at flight altitudes . . . 12
2.3.1 Radiation dose indicators . . . 13
2.3.2 D-Index and alert thresholds . . . 14
2.3.3 The Neutron Monitor Database (NMDB) . . . 15
2.3.4 GLE detection . . . 16
2.3.5 Models for radiation dose computation . . . 17
2.4 Internal and surface charging in GEO satellites . . . 22
2.4.1 Internal charging and risk indicators . . . 22
2.4.2 Surface charging and risk indicators . . . 25
2.5 Geomagnetic indices . . . 26

2.5.1 The geomagnetic disturbance index, K . . . 27
2.5.2 INTERMAGNET . . . 29
2.5.3 Efects of geomagnetic disturbances . . . 30

3 Radiation dose estimation at flight altitudes 33
3.1 Method . . . 33
3.1.1 Preliminary study of AniMAIRE for GCR model . . . 36
3.1.2 Preliminary study on GLE detection . . . 38
3.1.3 Preliminary study on GLE scenario dose computation . . . 42
3.2 Results . . . 48
3.3 Conclusions . . . 50

4 Internal and surface charging in geostationary orbit 53
4.1 Particle flux monitoring in GEO and data availability . . . 53
4.1.1 Instruments for particle detection in GEO . . . 53
4.1.2 Data applicability for operational service . . . 55
4.2 Data analysis for internal charging . . . 56
4.3 Data analysis for surface charging . . . 62
4.4 Method . . . 65
4.5 Results . . . 68
4.5.1 Real time operation (internal charging) . . . 68
4.5.2 Long term analysis (internal and surface charging) . . . 69
4.6 Conclusions . . . 71

5 Local geomagnetic disturbance indices 73
5.1 Geomagnetic observatory data studies . . . 73
5.1.1 Local K results calculation . . . 74
5.1.2 Correlation between local K results . . . 75
5.1.3 Averaging of local K values . . . 78
5.1.4 Conclusions from the studies . . . 81
5.2 Method . . . 82
5.3 Results . . . 84
5.4 Conclusions . . . 86

6 Conclusions and future work 89
6.1 Radiation dose estimation at flight altitudes . . . 89
6.2 Internal and surface charging in GEO . . . 90
6.3 Local geomagnetic disturbance indices . . . 91

Bibliography **93**

A Appendix A **101**
A.1 GCR maps from WASAVIES and AniMAIRE . . . 101
A.1.1 30 km of altitude . . . 101
A.1.2 56 km of altitude . . . 102
A.1.3 94 km of altitude . . . 103
A.2 Figures from GLE detection studies . . . 104
A.3 Figures from Radiation Dose studies . . . 109
A.3.1 GLE 73 . . . 109
A.3.2 GLE 74 . . . 110
A.3.3 GLE 75 . . . 112
A.3.4 GLE 76 . . . 114
A.3.5 GLE 77 . . . 116
A.4 Very energetic solar particle events without GLE . . . 117
A.5 Low energy differential electron fluxes from GOES 19 . . . 119
A.6 Kp values for solar storm periods . . . 122

List of Figures **125**

List of Tables **129**

List of Symbols **131**

Acknowledgements **133**

1 | Introduction

According to the National Oceanic and Atmospheric Administration (NOAA), Space Weather consists of the description of the variation of the space environment that separates the Sun and the Earth, focusing on the different phenomena that impact technologies, both in orbit and on ground [49]. The European Space Agency (ESA) cites the European Space Weather definition from the COST (European Cooperation in Science & Technology) Action 724, as "the physical and phenomenological state of natural space environments". In consequence, "the associated discipline aims, through observation, monitoring, analysis and modeling, at understanding and predicting the state of the Sun, the interplanetary and planetary environments, and the solar and non-solar driven perturbations that affect them, and also at forecasting and nowcasting the potential impacts on biological and technological systems" [14].

Both definitions mention the impact of Space Weather in humankind, as the ultimate motivation of Space Weather studies is, further from increasing scientific knowledge, understanding, preventing and mitigating the consequences in technology and health that this kind of phenomena can lead to.

The main Space Weather source of phenomena is the Sun, which continuously emits radiation and a stream of particles (the solar wind). These particles carry the magnetic field generated by the Sun throughout the Solar System, which is known as the Interplanetary Magnetic Field (IMF). Different Space Weather phenomena (like solar flares, coronal mass ejections, solar energetic proton events, high-speed solar wind streams, among others) are generated from the conditions on the solar surface and corona. Solar activity is guided by an 11-year cycle, with higher and lower periods (solar maximum and minimum, respectively). Not only the Sun is a source for Space Weather events, as other sources such as galactic cosmic rays (GCR) coming from outside our Solar System do alter the near-Earth space environment [14].

The impacts of Space Weather phenomena on technology and health will be carefully discussed in following Sections, and some examples can be cited, such as HF radio communications degradation and even blackout, anomalies and failures in satellites, geomag-

netically induced currents (GIC) that may degrade power grid operations, decrease of GNSS accuracy, increase of drag in LEO satellites and increase of radiation that may pose a risk for astronauts and aircraft crews. Other consequences of Space Weather are the Aurora Borealis and Australis over both polar regions and even at lower latitudes during higher activity periods [14, 49].

The motivation of this work arises therefore from the need of a world extremely dependent on technology to be aware of Space Weather events and their potential impacts. Not only does their direct impact constitute a real risk, but the combination of degraded technologies and other external factors can be fateful. Classical examples about extreme Space Weather impacts include the power blackout in Quebec during the 1989 strong geomagnetic storm [7] and the Carrington event, considered the most intense geomagnetic storm ever recorded, in 1859, that even set to fire several telegraph stations due to the induced currents [64]. The most recent strong Space Weather events, at the moment of writing in February 2026, are the solar storms of November 2025 and January 2026, both of them taking place during the development of this work. The characteristics of the latter and the mitigation measures taken by different operators avoided major effects, apart from radio communication disruptions [16, 19].

The objective of the work is the development of tools related to Space Weather impacts, by integrating available data, models and risk indicators, and seeking the capacity of studying the impacts a posteriori as well as operating the tool for nowcast or near-real time purposes. The impacts addressed by those tools are radiation dose at flight levels (Chapter 3), internal and surface charging in geostationary orbit (Chapter 4) and geomagnetic perturbations, measured through the local K indices (Chapter 5). Each tool has been developed accompanied by several short studies concerning different aspects of their use and the setting of some of their parameters. The structure of each chapter depends on the procedure followed for the tool design, integrating the results and conclusions from the studies with the method, results and conclusions about the tool itself. The Literature Review in Chapter 2 deals with the theoretical aspects of Space Weather, focusing first on the origin and impacts of the main phenomena and their characterization in terms of the NOAA scales, in relation with the studied impacts. Then, the basic theoretical aspects regarding radiation dose, GEO charging and geomagnetic disturbances are discussed, introducing the elements that are later used for the development of the tools. Finally, Chapter 6 collects the general conclusions about the work and possible future developments.

2 | Literature review

2.1. Space Weather overview

2.1.1. Solar cycle and solar activity

Solar activity follows an 11-years cycle that shapes Space Weather. During that period, known as the solar cycle, solar activity rises to a maximum and decreases again to a minimum. After this cycle, Sun's north and south pole switch places, so after around 22 years (two solar cycles), they come back to their original place. Each cycle receives a number, since the beginning of counting in 1755 with solar cycle 1 [49]. At the moment of writing, late 2025 – early 2026, the Solar Cycle 25 is experimenting its declining phase after the solar maxima.

A capital indicator of the solar cycle evolution are the sunspots, which are dark areas at the Sun's photosphere, resulting from intense magnetic flux arising from the interior of the Sun. Areas along that magnetic flux are called active regions, which can be observed as faculae and plage in the photosphere and chromosphere, and can contain sunspots or not. These regions are the main responsible for Space Weather events. Sunspots can last from hours to months and experiment a huge variation within the solar cycle [49]. Figure 2.1 shows the evolution of the solar cycles since the 18^{th} century in terms of the sunspot number, whose minima (maxima) are determined by the minimum (maximum) number of sunspots.

Solar activity denotes several events like solar flares, coronal mass ejections (CME), high speed solar wind or solar energetic particles [46].

The solar wind is a continuous flow of plasma from the Sun, composed mainly by electrons and protons, carrying solar magnetic field lines. This magnetic field is said to be frozen-in-flux and is called Interplanetary Magnetic Field (IMF). The solar wind can show different speeds and densities, depending on the region where it is produced. In the equatorial plane, where the Earth orbits, solar wind has a typical "low" speed of 400 km/s, while the presence of active regions and coronal holes can modify its characteristics, with high speed

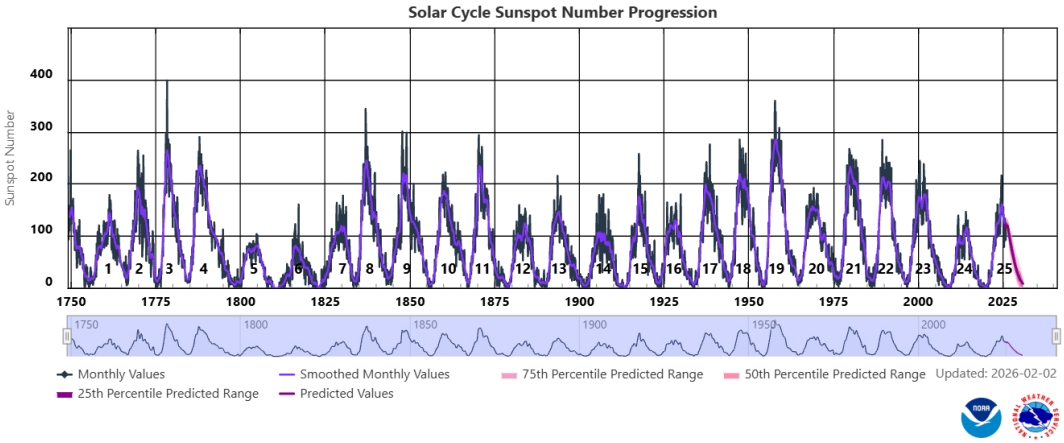

Figure 2.1: Solar cycle progression from Solar Cycle 1 to Solar Cycle 25 (until February 2026). Source: NOAA Space Weather Prediction Center (https://www.swpc.noaa.gov/products/solar-cycle-progression).

and southward orientation of the solar magnetic field lines being responsible for Space Weather phenomena when interacting with the Earth's magnetosphere. As mentioned, the presence of coronal holes, which are cooler and less dense open magnetic field regions on the solar corona, allow the solar wind to escape more easily, creating high speed streams (HSS). Contrarily to sunspots, coronal holes have their maximum number and last longer during solar minima [49].

Coronal mass ejections (CME) are massive ejections of plasma from the solar corona, carrying a stronger magnetic field than the IMF. The fastest CMEs can arrive to Earth in 15-18 hours, while slower ones may take a few days. The fast movement of CMEs can generate shock waves in the plasma, accelerating particles and increasing the risk of radiation storms. Furthermore, parameters of the CMEs like the strength and direction of the carried magnetic field have a critical importance on the strength of the geomagnetic activity caused by the event [49].

Solar flares are huge expulsions of electromagnetic radiation from the Sun that can last from minutes to hours, traveling at the speed of light, so their effects on Earth cannot be observed in advance and affect the sunlit side of the planet [49].

Flares and CMEs tend to be related, specially when the strength of the events is high, being both originated by magnetic activity at the Sun. They are also related to solar energetic particles (SEP), an enhanced flux of energetic protons, heavy ions and electrons, coming directly from the flare origin in the corona or accelerated by shock waves produced by CMEs [9].

These concepts are illustrated by the recent solar storms that took place during the development of this work. The solar storm of November 2025 consisted first on a solar flare that arrived to Earth on 2025/11/11, followed by a CME that reached Earth the next day, causing strong geomagnetic and radiation storms [16]. Similarly, the solar storm of January 2026 was originated by a solar flare followed by a CME, implying intense activity from 19 to 21 January and potential impacts on Earth [19].

2.1.2. Earth's magnetosphere

The magnetosphere is the region of space surrounding Earth defined by the interaction between the Interplanetary Magnetic Field (IMF) carried by the solar wind and the Earth's magnetic field. The Earth's magnetic field can be described as a dipole in first instance, with its magnetic axis inclined about 11° with respect to the rotation axis. The shape of the magnetosphere is the result of the solar wind compressing the Earth's magnetic field on the dayside, confined within 10 Earth radii. On the nightside, the magnetosphere is stretched within a tube shape, extending up to 60 Earth radii, in the region known as magnetotail. The boundary between the solar wind and the Earth's magnetic field is called the magnetopause [49]. A representation of the magnetosphere is depicted in Figure 2.2.

The limits of the magnetosphere are therefore dynamic, as they depend on the described interaction, and the consequences of this complex behavior include the creation of different regions of fields, particles (e.g the Van Allen belts) and electric currents inside the magnetosphere. The arrival of solar wind with certain characteristics and events like flares and CMEs, and their interaction with the Earth's magnetic field leads to changes in the conditions of the magnetosphere, which is the origin of the different Space Weather phenomena as perceived from Earth [49].

2.1.3. The Van Allen radiation belts

The Van Allen or Earth radiation belts are regions in Earth's magnetosphere composed by high energy particles captured by the Earth's magnetic field. Two different belts are distinguished: the Inner belt, dominated by high energy protons (order of more than 10 MeV) and with presence of energetic electrons too (order of MeV), and the Outer belt, dominated by energetic electrons. These belts are caused by the interaction between the solar wind and Earth's magnetic field and plasma environment, and the region separating them is called Slot-Region. The Inner belt is not much affected by solar activity, due to Magnetospheric shielding. The radial extent of the belts is extremely dynamic; the Inner

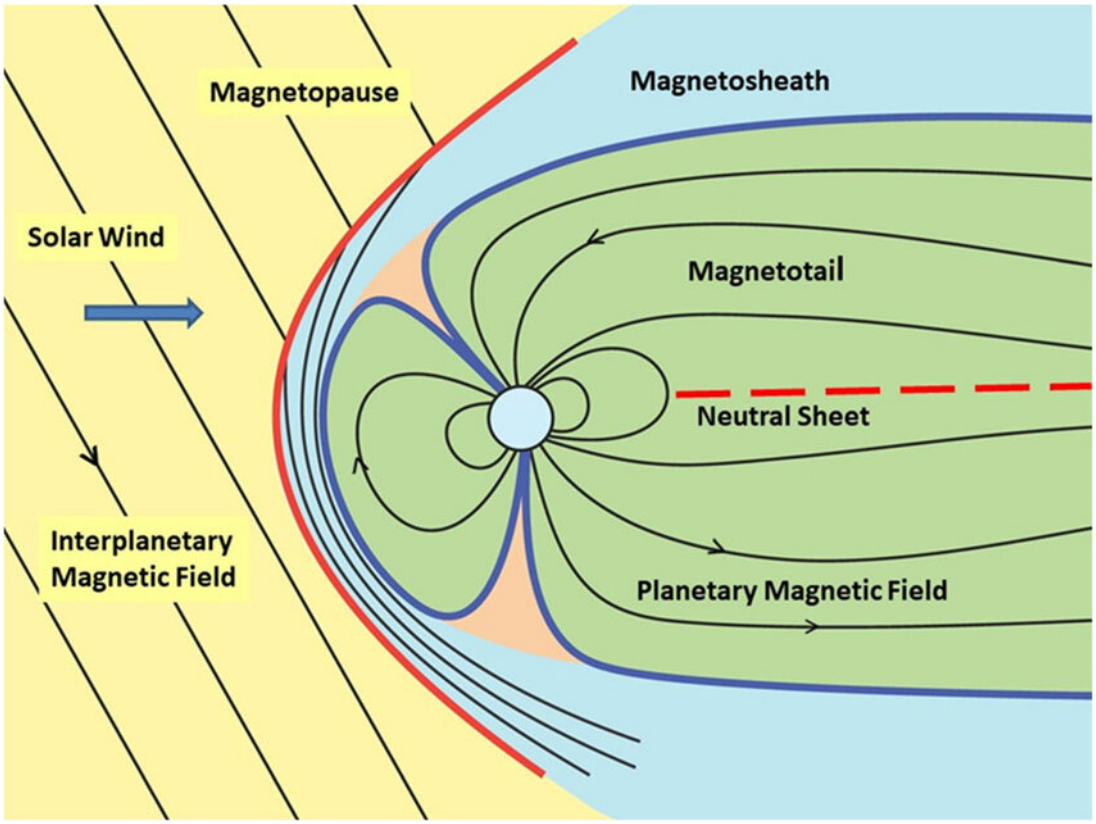

Figure 2.2: Structure of Earth's magnetosphere. Reproduced from [65] without changes, licensed under CC BY 4.0 (https://creativecommons.org/licenses/by/4.0/).

belt electron content ranges from 1.5 to 3 Earth radii (that is from around 10000 to 19000) and its proton content from 1.1 to 3 Earth radii, while the Outer belt (mainly electrons) ranges from about 3 to 10 Earth radii (around 19000 to 64000 km). The presence of this high energy particles can have hazardous effects in satellites and astronauts, and even affect chemical processes in the atmosphere [33, 49].

The variation of the Outer belt within the solar cycle is consistent with the solar wind structures evolution along it. While CME associated storms, more frequent around solar maxima, enhance the flux in the inner portion of the Outer belt, coronal hole HSS tend to enhance the outer portion and therefore the GEO region during solar minima [45].

2.2. Space Weather phenomena and NOAA scales

After having defined how Space Weather is originated from the interaction between solar activity and Earth's magnetic field, the Space Weather phenomena perceived from Earth and their respective impacts are considered, along with the scales defined by the National Oceanic and Atmospheric Administration (NOAA) to assess their risks. The focus is on

phenomena related to the impacts studied in this work, while other important impacts remain out of scope and are only mentioned or not included.

A scheme representing the relationships between solar activity, Space Weather phenomena and impacts is depicted in Figure 2.3. The already described solar activity events (flares, CME, HSS) are connected to their solar origin in active regions and coronal holes, and to other derived events that take place on Earth as a consequence, the solar energetic particles (SEP) and ground level enhancements (GLE), which will be described later. Also galactic cosmic rays (GCR) are included as a non solar source of Space Weather. All of these events have direct impacts on technologies and health and the scheme shows the coupled connections between events and impacts. To complete the scheme, the NOAA scales are added, as a frame where the impacts are included, with some of them belonging to more than one scale. Each of the scales addresses a particular Space Weather phenomena (geomagnetic storms, solar radiation storms, radio blackouts), that consist on the perception from Earth of the interaction between the solar activity events and the Earth's magnetic field. Those phenomena will be described in what follows together with the scales and it has to be noticed that, as the scheme displays, the phenomena can be produced by different events. As an example, a geomagnetic storm can be produced by both a CME or a HSS, with the first one producing the strongest values in the G scale (and therefore more risk and potential damage of the impacts) and the second one producing weaker values.

2.2.1. Geomagnetic storms and G-Scale

Geomagnetic storms consist of intense disturbances of the Earth's magnetosphere as a result of a very effective energy transmission from the solar wind. The variations in solar wind conditions related to this are its speed and the direction of the magnetic field lines that are carried in the solar wind plasma. If the solar wind magnetic field is directed southwards, which is opposite to the dayside Earth's magnetic field directed northwards, the magnetic merging is more efficient and more energy is injected into the magnetosphere. Furthermore, the merging rate also increases with the solar wind speed. Other aspects that can also have an influence are solar wind density and temperature [9, 35, 49].

Coronal mass ejections (CME) from the Sun cause the largest geomagnetic storms, when up to thousands of millions of tons of plasma, carrying Sun's magnetic field lines, arrive to Earth, lasting from tens of hours to days. Another cause of geomagnetic storms are high speed solar wind streams (HSS), generally coming from coronal holes, that can even inject more energy in the magnetosphere but over a longer interval, causing less intense

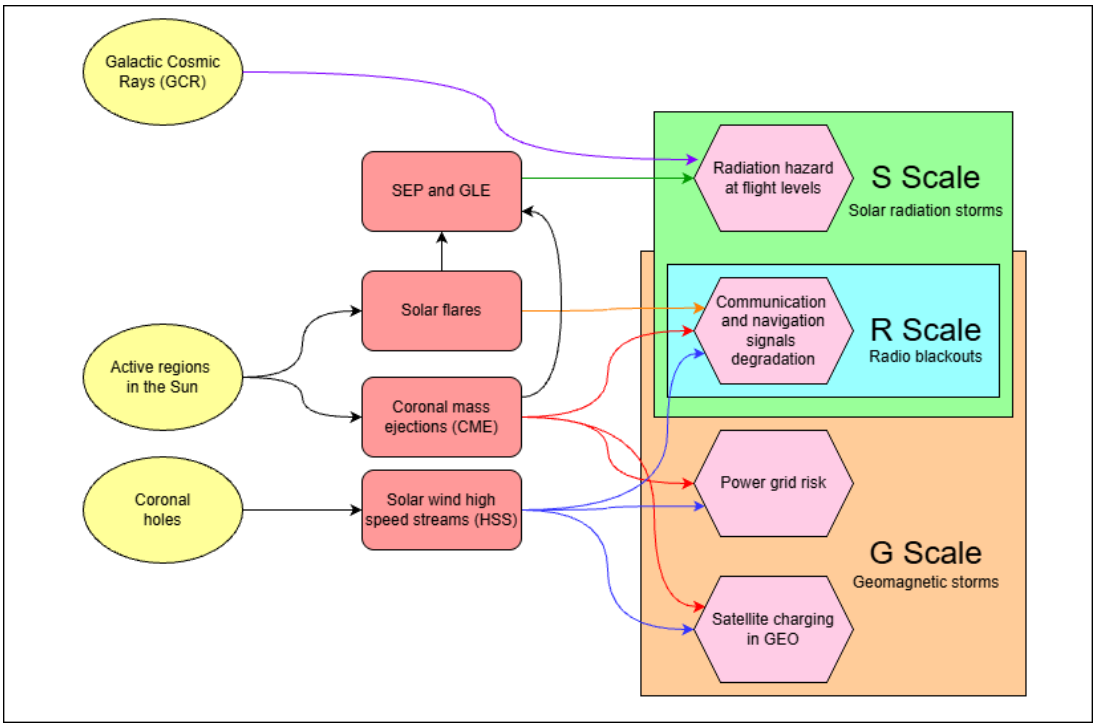

Figure 2.3: Relationships between space weather events and impacts.

storms [49].

Geomagnetic storms are the origin of the enhancement of the magnetospheric currents intensity, whose associated magnetic activity will cause disturbances on ground. Those disturbances can be measured by geomagnetic observatories on Earth's surface, being in most cases not bigger than 300 nT, depending on the magnetic latitude of the station. The planetary geomagnetic disturbance index, Kp, is produced by the ground measurements of the magnetic disturbances and potential impacts are related to this index by the NOAA's G Scale, as depicted in Table 2.1. Typical impacts include voltage control problems in power systems, undesired behavior and charging in spacecrafts, induced pipeline currents and degradation or lost of high and low frequency radio and GNSS. The most harmful effects during a G5 event could lead to the collapse of power grid systems and communication blackout for days. Geomagnetic storms also produce an increase in density of the atmosphere, which enhances the drag in LEO satellites [9, 48, 49].

To go further, geomagnetic substorms are another type of geomagnetic activity, which can happen (one or more) during a geomagnetic storm or isolated, having different characteristics according to the situation. During isolated substorms, which are not part of geomagnetic storms, the solar wind energy is transported from the dayside of the magnetosphere to the nightside (magnetotail), through the magnetic reconnection, and is

released there when stability is lost, causing the onset of the substorm. The magnetic energy is then turned into kinetic energy of the plasma, implying the formation of auroras and enhancement of ionospheric currents, during the expansion phase, and coming back finally to the initial state during the recovery phase [9].

Table 2.1: NOAA Space Weather Scales (G, S, and R) from [48].

Geomagnetic storms (G Scale) Measure: Kp Index		
Scale	**Kp Threshold**	**Avg. Frequency (per cycle)**
G5 Extreme	Kp 9	4
G4 Severe	Kp 8 (incl. 9-)	100
G3 Strong	Kp 7	200
G2 Moderate	Kp 6	600
G1 Minor	Kp 5	1700

Solar radiation storms (S Scale) Measure: Flux level of > 10 MeV particles		
Scale	**Flux Threshold** ($cm^{-2}s^{-1}sr^{-1}$)	**Avg. Frequency (per cycle)**
S5 Extreme	10^5	Fewer than 1
S4 Severe	10^4	3
S3 Strong	10^3	10
S2 Moderate	10^2	25
S1 Minor	10	50

Radio blackouts (R Scale) Measure: GOES X-ray peak brightness by class and flux		
Scale	**Flux Threshold** (Wm^{-2})	**Avg. Frequency (per cycle)**
R5 Extreme	X20 (2×10^{-3})	Fewer than 1
R4 Severe	X10 (10^{-3})	8
R3 Strong	X1 (10^{-4})	175
R2 Moderate	M5 (5×10^{-5})	350
R1 Minor	M1 (10^{-5})	2000

2.2.2. Radio blackouts and R-Scale

A major effect of solar flares is called the radio blackout, consisting in the interruption of high frequency communication in the sunlit side of Earth, implying also outages of low frequency and GNSS navigation signals in such region. This is a result of the arrival

of large levels of electromagnetic energy, with X-ray and extreme ultraviolet (EUV) enhancing the ionization in the lower ionospheric layers and leading to the degradation or absorption of the waves [48, 49].

The R Scale quantifies the effects of the radio blackouts in terms of the flare intensity, with M and X classes being the most intense ones, together with the corresponding flux values measured in the 0.1–0.8 nm range in W m^{-2} [48] as depicted in Table 2.1.

2.2.3. Solar radiation storms and S-Scale

Large-scale magnetic eruptions, that often involve a CME and a solar flare, cause the acceleration of charged particles (mainly protons) in the solar atmosphere, reaching extremely high velocities. At their arrival to Earth, those protons can penetrate the magnetosphere and reach the atmosphere, being guided by the magnetic field lines towards the poles. This is known as a solar radiation storm [49].

These particles coming from the Sun are called solar energetic particles (SEP) and their presence directed to Earth is referred to as a SEP event or SPE (Solar Proton Events).The arrival of high energy SEP fluxes to the atmosphere can unleash a ground level enhancement (GLE), which implies an enhancement of radiation environment that can be dangerous for human health above a certain altitude, depending on the strength of the phenomenon [31].

The NOAA's S Scale characterizes the strength of a solar radiation storm, as shown in Table 2.1. The flux of more than 10 MeV protons is measured by the GOES satellites and according to the flux level in a logarithmic scale, the storm can be classified from S1 to S5. The effects of solar radiation storms can be biological and affect to satellite operations and communication systems. Extreme cases in S5 events would imply high radiation hazard for passengers and crew in high flight levels and high latitudes, electronic errors in satellites and high frequency and GNSS blackout in very high latitudes [48].

2.2.4. Galactic cosmic rays (GCR)

Originating outside the Solar System from sources like supernovae, neutron stars or black holes, among others, the galactic cosmic rays (GCR) suppose a constant background source of energetic particles that permanently reach Earth. These particles consist on fully ionized nuclei (no presence of electrons), from every element, being mainly characterized by hydrogen (around 89%), and therefore high energetic protons [21, 49].

Due to the ionization of the particles, Sun's strong magnetic field, dragged by solar wind,

modulate the flux of GCR and its spectrum at Earth. This implies that, during high solar activity, near solar maximum, low-energy GCR particles are modulated and therefore cannot reach Earth, implying a GCR minimum. On the other hand, near solar minimum, GCR particles can reach Earth more easily, implying then a GCR maximum. The flux, anyway, is relatively constant in energy and composition and the variation is slow in time, following the mentioned 11-year cycle, opposite to the Sun's [49].

The GCR particles arriving to Earth interact with atoms in the upper atmosphere and unleash showers of secondary particles that can even reach ground and be detected. These are known as extensive air showers (EAS) and are the cause for ionizing radiation due to GCR. Those secondary particles, mainly neutrons, can be detected by neutron monitors (NM) to measure cosmic radiation produced by GCR [12, 21, 39].

Furthermore, a Forbush decrease is a transient depression in the intensity of GCR observed at Earth, primarily caused by the passage of CMEs and their associated interplanetary shocks. The decrease begins with the arrival of the interplanetary shock. The region immediately following the shock contains highly turbulent magnetic fields. This turbulence scatters cosmic rays, reducing their intensity before the arrival of the CME itself. Upon the entry of the CME material, the strong, closed magnetic field loop structure it carries acts as a barrier, effectively excluding GCR from its interior [10].

A recent example of a Forbush decrease took place during the solar storm of January 2026 [26]. Another interesting example occurred during GLE 74 in May 2024, with a Forbush decrease in GCR intensity produced by the arrival of a CME and a consecutive GLE resulting from the solar radiation storm associated to the CME and flare [2, 20]. The latter is represented through the neutron count rates measurements in several stations in Figure 2.4 (left), where it can be seen that higher neutron count rates originated by GCR experimented an important decrease due to the Forbush decrease and finally a punctual increase, during the GLE duration, to finally return and stabilize around lower values that at the beginning.

2.2.5. Ground level enhancements (GLE)

As mentioned in relation with solar radiation storms, the arrival of solar energetic particles (SEP) to the atmosphere can enhance the radiation environment at flight altitudes and pose a risk to human health and even produce failures in electronic devices. This is due to the additional extensive air showers, triggered by the SEP, added to the ones caused by GCR. This phenomena is known as ground level enhancement (GLE) and can be detected from a significant increase in the neutron count rate of many neutron monitor stations,

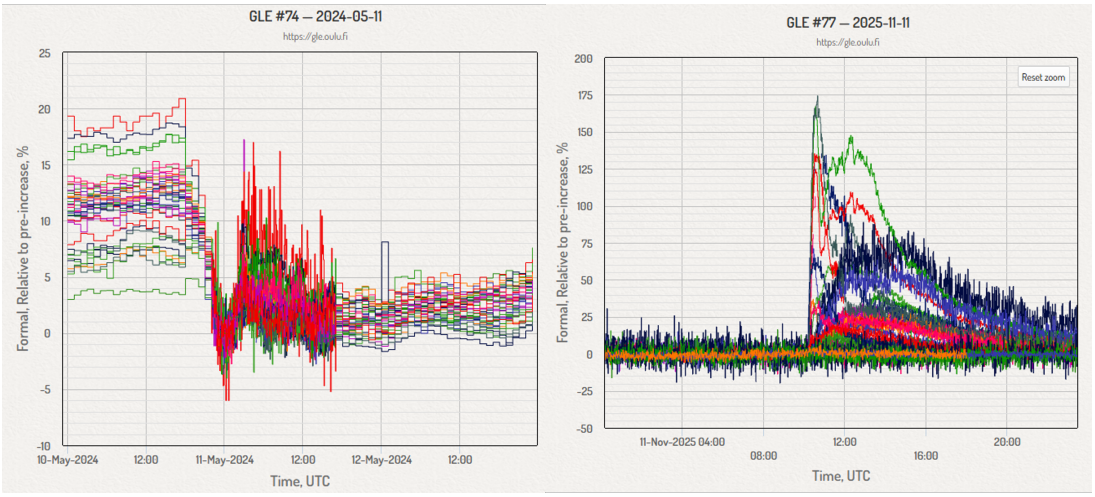

Figure 2.4: Neutron count rates during GLE 74 (2024/05/11) and GLE 77 (2025/11/11). Source: International GLE database ([67]).

lasting from tens of minutes to a few hours [12, 21]. Since the 1940's and at the time of writing, 77 GLE have been detected through the neutron count rate increase at the mentioned stations. Particularly, the 77$^{\text{th}}$ GLE took place on 2025/11/11 during the development of this work, as a consequence of the solar storm of November 2025 [16]. This can be seen in Figure 2.4 (right), where a huge increase of the neutron count rates in several stations show the strength of this GLE event.

GLE events differ to each other in intensity and direction of arrival of the particles, implying the anisotropy of the phenomena as seen from Earth's surface. This implies that some stations may measure higher increase than others and that radiation dose peaks can be localized in determined regions [12, 23]. Direction of the particles is modulated by the Earth magnetic field as they are charged and therefore experience the Lorentz force, as well as by the rigidity of the particles, which is proportional to their momentum divided by their charge [32].

2.3. Radiation dose at flight altitudes

Space Weather impact on human health is mainly related to ionizing radiation due to both galactic cosmic rays (GCR) and energetic solar particles. Thanks to the geomagnetic field, critical radiation effects are confined to high latitudes regions and high altitudes, but risks are increased when solar activity is strong, particularly in presence of solar radiation storms. In absence of the latter, radiation dose at flight altitudes is explained by the arrival to Earth of GCR, which consist on a very slow varying source. However, levels of radiation dose can be strongly increased during the development of solar radiation

storms, during the arrival of solar energetic particles (SEP), giving rise to ground level enhancements (GLE). Estimation of the radiation dose indicators implies then modeling both scenarios: GCR and GLE.

The present Section develops the Literature Review about the Radiation Dose impacts, as the basis for Chapter 3. The main useful indicators for radiation dose for health and electronic failures, risk indicators to assess radiation dose at flight levels, the Neutron Monitor Database (NMDB), algorithms related to GLE detection and models for radiation dose computation are described in what follows.

2.3.1. Radiation dose indicators

Some quantities and indicators to assess the effects of radiation dose both in health and in electronic devices are defined as follows:

- **Effective dose (E) in Sv:** The ICRP defines the effective dose (in Sievert, i.e. $Sv = J/kg$) as "the tissue-weighted sum of the equivalent doses in all specified tissues and organs of the body" [25]. It is used for radiation protection purposes. In cosmic radiation its value is typically expressed in μSv and its rate (in $\mu Sv/h$) is used to identify the effective dose per unit of time [34].
- **Ambient dose equivalent ($H^*(10)$) in Sv:** An operational quantity used for area monitoring of external radiation, measured as well in Sievert. It is an experimentally accesible value, which is important on validation of the numerical models for dose computations [34].
- **Dose equivalent (H) in Sv:** Defined by the ICRP as the product of the absorbed dose (D) and the quality factor (Q) at a specific point in tissue ($H = D \cdot Q$). The quality factor Q characterizes the biological effectiveness of radiation. Unlike the protection quantities (such as effective dose), dose equivalent is an operational quantity; it serves as the basis for defining measurable quantities—such as the ambient dose equivalent $H^*(10)$—used in area and personal monitoring to demonstrate compliance with radiation limits [25]. Again, in cosmic radiation its value is typically expressed in μSv and its rate (in $\mu Sv/h$).
- **Single event upset (SEU):** A SEU is a specific type of non-destructive error that occurs in memory elements. It characterizes a single particle strike in a memory element that leads to a bit flip, causing data corruption, and affects circuits like Static Random-Access Memories (SRAM). Atmospheric neutrons are a direct cause of these SEU in aircraft avionics [54, 56]. A SEU rate expressed in $s^{-1}bit^{-1}$ can be

defined to assess their possibility of occurrence.

- **Single event latch-up (SEL):** A SEL is a potentially destructive effect primarily observed in bulk CMOS (Complementary Metal-Oxide Semiconductor) technology, consisting on a high-current state caused by the activation of parasitic structures within the silicon layout. A power cycle is necessary to restore the functionality of the circuit [56]. Similarly to SEU, a SEL rate can be expressed in $s^{-1}device^{-1}$.
- **Neutron flux:** Neutron flux can be measured in neutrons/cm^2/s. Around 50% of the radiation at flight altitudes is composed by neutrons [31], so neutron fluxes of neutron over certain energies can be an interesting operational proxy.

A very illustrative example of impact caused by radiation effects took place during the development of this work. On October 30, 2025, JetBlue flight 1230, an Airbus A320 flying from Cancun to Newark, experienced a sudden, uncommanded pitch-down event while cruising at 35,000 feet. The pilots were able to regain control and perform an emergency landing in Tampa, Florida, but the abrupt maneuver resulted in injuries to at least 15 passengers. The investigation identified the root cause as a single event upset within the aircraft's elevator aileron computer (ELAC), related to intense solar radiation, during the solar maximum period of Solar Cycle 25. Approximately one month after the event, the industry initiated one of its most significant recalls in history, resulting in the grounding of over 6,000 airplanes. This decision caused major flight cancellations and disruptions during the highly active travel period immediately following Thanksgiving in late November 2025. To address the vulnerability of onboard electronics to space radiation, every affected aircraft required a software update, while approximately 900 planes needed the installation of entirely new computer hardware [1, 5].

2.3.2. D-Index and alert thresholds

According to NOAA scales, an operational D index is proposed in [40] to assess the radiation dose. It has been used since 2014 to provide several airlines with this information. It uses the effective radiation dose rate due to the solar contribution (measured in $\mu Sv/h$) as a proxy to identify radiation hazard at flight altitudes (possible values for D are depicted in Table 2.2). Radiation due to the GCR background is therefore not considered for the index as it is the solar contribution the one that can produce hazardous levels during strong solar activity. Need for this kind of index arises form the fact that solar radiation storms do not always unchain a GLE event, so the S-Scale is not precise enough to assess radiation dose at flight levels. This index can be used at any flight altitude by using the corresponding radiation dose expected at that altitude.

The threshold of 20 μSv/h is of particular operational importance. This value defines the onset of the D3 (Moderate) category and was selected to align with the trigger levels of the FAA Solar Radiation Alert system for altitudes between 30.000 ft (9 km) and 70.000 ft (21 km) [40]. At this specific dose rate, mitigation procedures such as altitude reduction become recommended for high-latitude flights.

Also ICAO defines two thresholds for Space Weather advisory: an effective dose greater than 30 $\mu Sv/h$ reached at FL460 or below (more than around 14 km) leads to a Moderate alert, while greater than 80 $\mu Sv/h$ at any flight level leads to a Severe alert [28].

Table 2.2: Values of the Space Weather D-index from D0 to D5, their classification, and corresponding dose rate intervals (from [40]).

Index D	**Classification**	**Effective Dose Rate due to solar contribution** ($E[\mu Sv/h]$)	**Comparable Exposure**
D0	Quiet	$E_{sol} < 5$	Variation of natural background at cruising altitudes
D1	Nominal	$5 \leq E_{sol} < 10$	Natural background at high latitudes up to FL400
D2	Minor	$10 \leq E_{sol} < 20$	Natural background at high latitudes between FL400 and FL600
D3	Moderate	$20 \leq E_{sol} < 40$	Average dose rate inside the International Space Station (ISS)
D4	Strong	$40 \leq E_{sol} < 80$	Average dose rate during an extra-vehicular activity (EVA) on the ISS
D5	Severe	$80 \leq E_{sol} < 160$	Dose of a North Atlantic return flight per hour

2.3.3. The Neutron Monitor Database (NMDB)

Neutron monitor (NM) stations are standard ground-based detectors designed to measure variations in cosmic ray intensity, through the detection of secondary particles, mainly neutrons, produced by cosmic rays interacting with upper atmosphere atoms [38, 39].

The Real-time Neutron Monitor Database (NMDB), originally developed under the European Union's 7th Framework Programme, was established to create a centralized, high-resolution repository for cosmic ray data collected by the worldwide network of Neutron Monitor stations. Before the implementation of the NMDB, data access was often frag-

mented, differing by station, and frequently subject to time delays. The NMDB addresses these limitations by standardizing data formats and providing measurements updated every minute. By pooling data from international stations in real time, the database effectively utilizes the Earth as a single, planetary-scale multidirectional detector [38].

Data from NMDB is offered through the Neutron Monitor Event Search Tool (NEST)[1], where 58 neutron monitor stations can be operative. The sensitivity of each NMDB station to different cosmic ray energies is determined by its geomagnetic cut-off rigidity (R_c) typically expressed in GV. This allows the Earth's magnetic field to be utilized as a global spectrometer. In this configuration, equatorial stations (where $R_c > 11$ GV) effectively filter out lower-energy particles, whereas polar stations (with $R_c \approx 0$ GV) provide an open window for virtually the entire cosmic ray energy spectrum [61]. NEST allows neutron count rates consultations at desired periods of time and selecting the stations, and it is accessible through API. A near-real time relation of neutron count rates is offered directly in .txt format[2] with last data from the operating Neutron Monitors, providing more than one hour of last data with one value of count rates per minute.

Several models to estimate radiation dose at flight altitudes (MAIRE+, NAIRAS, WASAVIES) use as proxies the neutron count rate measured at the different stations composing the network [23, 41, 58].

Neutron count rates are also a fundamental proxy in GLE detection, as many stations experiment a considerable increase of them during such events [55]. The official neutron monitor database during GLE[3] is provided by the Oulu Cosmic Ray Station of the University of Oulu, Finland [67].

2.3.4. GLE detection

GLE detection in real time is crucial to stay aware of the ionizing radiation dose at which human beings might be exposed at certain altitudes, as well as the possibility of failure in electronic devices.

As mentioned before, the detection of this phenomenon will rely on the measurement of a considerable increase in neutron count rate at many neutron monitor stations. The affected stations and the neutron count rate increases will depend on the direction of arrival of the particles and strength of the event, due to GLE's anisotropic nature [12].

Historically, the detection of a GLE has simply required the measurement of neutron count

[1]NEST can be accessed through http://www.nmdb.eu/nest/.
[2]Available at urlhttps://www.nmdb.eu/rt/realtime.txt
[3]GLE database can be accessed through https://gle.oulu.fi/#/.

rate increases by at least two differently located neutron monitors, showing near-time coincidence and statistically significant enhancements. However, this definition has become limited and potentially problematic following the installation of modern high-altitude polar stations. Due to their location, these stations benefit from negligible geomagnetic shielding and reduced atmospheric cut-off, making them significantly more sensitive to lower-energy particles than standard sea-level detectors. Under the original definition, an event detected by two high-altitude stations would be classified as a GLE, including weak events that would have gone unnoticed in previous solar cycles. Therefore, a revised definition can be made: for an event to be classified as a GLE, the increase must still be registered by at least two differently located neutron monitors, but at least one of these monitors must be located near sea level. Furthermore, this ground-based detection should be corroborated by a corresponding enhancement in proton flux as measured by space-borne instruments, like the SEISS-SGPS instrument on-board of the GOES-R series (16, 17, 18 and 19) satellites[4] [55]. This is the definition used by the official GLE database by University of Oulu (see Section 2.3.3).

Another approach for GLE detection is the one followed by GLE Alert++ [5] tool, developped by Athens Neutron Monitor Station (A.Ne.Mo.S), consisting of a real-time detection algorithm that utilizes 1-minute resolution data from NMDB. The algorithm operates by first identifying persistent intensity increases above a dynamic baseline in individual neutron monitors, and subsequently triggering a system-wide alert only when at least three different stations confirm such increases within a fifteen-minute window [62].

2.3.5. Models for radiation dose computation

Finally, some models for radiation dose computation that have been considered for the Radiation Dose Estimation Chapter are described. MAIRE+, WASAVIES and NAIRAS are designed to compute radiation dose rates considering the GCR background and the possible contribution from GLE events, and using neutron count rates from several stations as inputs, as well as satellite data [23, 41, 42, 58]. Only WASAVIES considers the anisotropy of the GLE [58]. Meanwhile, AniMAIRE and CRAC:DOMO are prepared for radiation dose rates computations from a given particle spectra and anisotropy parameters, which typically require a previous study of the GLE characteristics [12, 43]. Furthermore, some statistical models can be extracted from CRAC:DOMO to be used as

[4]Historical data from the GOES-R instruments can be accessed through https://data.ngdc.noaa.gov/platforms/solar-space-observing-satellites/goes/ as well as through Space Weather Data Portal https://lasp.colorado.edu/space-weather-portal/ and near-real time data from the GOES-R instruments can be accessed through https://services.swpc.noaa.gov/json/goes/.

[5]Available at ESA Space Weather Service Network: https://swe.ssa.esa.int/anemos-federated.

a nowcast indicator of maximum effective dose during a GLE event [44].

MAIRE+ model

MAIRE+ (Model for Atmospheric Ionizing Radiation Effects) is an operational model developed under the UK Space Weather Instrumentation, Measurement, Modeling and Risk (SWIMMR) programme to provide real-time nowcasts of the aviation radiation environment. Its primary objective is to estimate radiation levels from ground level up to 20 km altitude across the globe, covering both GCR and GLE scenarios. MAIRE+ calculates not only particle fluxes and effective dose rates but also single event effects (SEE) in avionics electronics, such as single event upsets (SEU) and latch-ups (SEL) [23].

The system functions in GCR mode by default, operating a parallel detection algorithm to switch to GLE mode. It monitors data from the Oulu neutron monitor in Finland and the GOES 16 satellite, and the GLE mode is activated only if the Oulu count rate increases by more than 8% above its baseline and the >500 MeV proton flux measured by GOES increases by more than 50% simultaneously [23].

To compute the radiation dose indicators in GCR scenario, the model only needs the neutron count rate in Oulu as input. When the GLE mode is triggered, the system characterizes the solar particle spectrum using a simplified two-station method focused on the European sector. It uses real-time data from the Oulu and Dourbes (Belgium) neutron monitors as inputs. If an event is detected at Oulu but is too weak to trigger a significant increase at Dourbes, the model adopts a fallback scenario, assuming a conservative worst-case soft spectrum to ensure safety margins are maintained [23].

The model's performance has been validated against historical in-flight data. While the model performed well for GCR conditions, the validation highlighted limitations regarding anisotropy, as the model assumes that the GLEs are isotropic, which is a conservative approach. Furthermore, the model relies on European neutron monitors and, consequently, while the choice of European stations maximizes accuracy for UK airspace, it introduces uncertainty for global nowcasting during anisotropic events [23].

An experimental version of MAIRE+ called MAIRE-S is available online[6] provided by the University of Surrey, offering near real-time dose rates and SEU global maps.

[6] Available at https://spaceweather.surrey.ac.uk/maire-s_nowcast.php

AniMAIRE model

AniMAIRE (Anisotropic Model for Atmospheric Ionising Radiation Effects) is an open-source[7] Python toolkit designed to calculate radiation dose rates and single event effects in the atmosphere during GLEs. Developed by the Space Environment and Protection Group at the University of Surrey, it builds upon the physics of the MAIRE+ model but introduces the capability to handle anisotropic solar energetic particle (SEP) events, where particle flux varies significantly with direction. AniMAIRE allows users to input direction-dependent particle spectra and pitch angle distributions to produce more accurate dose rate maps [12, 13]. As a toolkit, AniMAIRE offers functions for radiation dose indicators computation, but does not include any GLE detection logic for nowcasting, as the other models do.

While the initial implementation of AniMAIRE relied on the MAGNETOCOSMICS software to perform magnetospheric transport calculations, the toolkit has subsequently adopted OTSO as its default engine for these tasks [13]. As a modern, open-source successor to MAGNETOCOSMICS, OTSO computes particle trajectories using numerical integration through magnetic field models. By integrating OTSO, AniMAIRE determines the necessary filtering functions, required to modulate the isotropic GCR background for local geomagnetic conditions [12, 32].

To execute the simulations, AniMAIRE provides a few functions dependent on the particle spectra, accepting other inputs related to position and time, and additional parameters. The function *run_from_spectra* serves as the main entry point for the toolkit, allowing users to input custom proton or alpha particle spectra alongside specific magnetospheric conditions. For standard spectral forms often encountered in solar physics, the library also includes convenience wrappers such as *run_from_power_law_gaussian_distribution* and *run_from_double_power_law_gaussian_distribution*, which automate the definition of spectral shapes and pitch angle distributions [13]. Also a function that implements the MAIRE+ logic for particle spectra computation, *run_maireplus_spectrum*, using neutron count rate increases in two different neutron monitor is offered, assuming an isotropic structure of the GLE. For GCR, the function *run_from_DLR_cosmic_ray_model* to do the computations from the Oulu neutron count rate as input. The outputs generated by these functions include effective dose (E) in μSv/hr, ambient dose equivalent ($H^*(10)$) in μSv/hr, and dose equivalent in μSv/hr. Additionally, the toolkit computes metrics relevant to avionics reliability, specifically single event upset (SEU) rates in upsets/second/bit and single event latch-up (SEL) rates in latch-ups/second/device, as well as neutron fluxes

[7] Available in GitHub: https://github.com/ssc-maire/AniMAIRE-public

across multiple energy thresholds (>1, >10, and >60 MeV) [13].

CRAC:DOMO model and derived statistical models for GLE

CRAC:DOMO (Cosmic Ray Atmospheric Cascade: Dosimetric Model) is a numerical model designed to assess radiation exposure at aviation altitudes, developed by the University of Oulu (Finland). It computes the total radiation dose, accounting for both the continuous GCR background and eventually GLEs, whose anisotropy is considered. The modulation potential is the needed parameter to compute the GCR spectra and its derived radiation dose rates, while the particle spectra and the anisotropy parameters are required for the radiation doses computation during GLE events [31, 43]. Like AniMAIRE, it is a model for dose rates computation, not including a detection logic.

Building upon these physics-based calculations (using a previous model that later became CRAC:DOMO), a statistical model was developed in [44] to serve as a rapid, operational proxy for assessing radiation hazards during ground level enhancements (GLEs). The authors retrospectively analyzed 34 historical GLE events where spectral information was available, computing the maximum effective dose rates at a typical commercial cruising altitude of 35,000 feet (around 11 km). The study revealed a highly significant correlation between the computed maximum effective dose rates at flight altitude and the peak percentage increase in count rates recorded by ground-level neutron monitors. Based on this finding, they proposed a statistical power-law relationship, $E(x) = \exp(a + b\ln(x))$, which allows the neutron monitor count rate increase to function as a convenient real-time proxy. This enables operators to instantly estimate peak effective dose rates using real-time data from the global neutron monitor network, without the need for time-consuming spectral inversion simulations during an evolving event. It is important to notice that this model assesses only the effective dose rate due to solar particles, so the GCR contribution must be added to compute the total effective dose. Furthermore, it is only valid at the forementioned 35,000 ft altitude and refers to the maximum effective dose in the whole globe (reachable near the poles), which normally will differ much from the ones at lower latitudes [44].

NAIRAS model

NAIRAS (Nowcast of Aerospace Ionizing Radiation System) is a physics-based operational model developed by NASA to predict ionizing radiation exposure for aerospace applications, spanning from the Earth's surface to deep space. Its primary objective is to provide real-time nowcasts and forecasts of dosimetric and radiative flux quantities

to assess human health risks and single event effects (SEEs) on flight electronics. Version 3, now operating at the Community Coordinated Modeling Center (CCMC)[8], offers real-time global predictions and a "run-on-request" capability for retrospective analysis. To characterize the radiation environment, the model assimilates real-time data inputs: GCR are modeled using 4 neutron monitor counts, while solar energetic particle spectra are inferred from GOES integral proton fluxes; and trapped radiation is modeled from solar radio flux and neutron monitor data [41, 42]. NAIRAS does not take into account the anisotropy of GLE, modeling them by directly using satellite data. Instead of using a detection mechanism to differ between GCR and GLE scenario like MAIRE+ and WASAVIES do, it considers GLE events by including the solar energetic particle contribution from satellite data.

NAIRAS has been validated against experimental data from the RaD-X balloon campaign[9] and spaceflight missions such as the International Space Station (ISS). Its validation shows an agreement to within 30% on the domain between 0 and 40 km of altitude [41, 42].

WASAVIES model

WASAVIES (Warning System for Aviation Exposure to Solar Energetic Particles) is a physics-based system developed by National Institute of Information and Communications Technology (NICT), Japan Atomic Energy Agency (JAEA), National Institute of Polar Research (NIPR), Hiroshima University, National Institute of Technology Ibaraki College, and Nagoya University, under the framework of Project for Solar-Terrestrial Environment Prediction (PSTEP), to estimate radiation exposure at aviation altitudes. The primary objective of the system is to provide real-time nowcasts and forecasts of radiation dose rates globally [47, 58].

The system functions in GCR mode by default and it continuously checks for the onset of a solar event to switch to SEP mode. Every 5 minutes, the system downloads the latest count rates from 13 neutron monitors and proton fluxes from the GOES satellites. The system detects a GLE and activates SEP mode if two specific thresholds are met simultaneously: the count rates of more than two NM stations increase by at least 4% above their background level and the proton flux of energies greater than 100 MeV measured by GOES exceeds 1 pfu. The radiation environment caused by GCR at different altitudes is computed at the end of each day. This results in a baseline global dose map to which any additional solar radiation is added during a GLE event. Upon activation of the SEP

[8] Available at https://ccmc.gsfc.nasa.gov/models/NAIRAS~3.0/
[9] Data available at: https://zenodo.org/records/14927669

mode, the system switches to a real-time analysis cycle that repeats every five minutes. It calculates through a complex procedure the parameters that characterize the GLE, considering the anisotropy of the event. The derived radiation dose rates are summed with the baseline GCR dose to generate the total effective dose rate [58].

The WASAVIES model is technically capable of estimating radiation doses throughout the entire atmosphere, from sea level up to a maximum altitude of 86 km. Its reliability is most robust at ground level and standard aviation altitudes (approximately 12 km), where it has been successfully validated against neutron monitor data and in-flight dose measurements. However, for higher altitudes, the model's precision degrades. Furthermore, the model assumes the GCR dose rate is constant during the GLE event and therefore does not account for Forbush decreases in real-time [58].

WASAVIES is available online[10], offering near real-time interactive effective dose rate maps of the world at ten different altitudes from 1 meter to 94 km (higher altitudes shall be less accurate according to what has been said). For GCR scenario a single map is displayed during the day, while for GLE scenario both nowcast and forecast maps are depicted.

2.4. Internal and surface charging in GEO satellites

The satellites located in geostationary orbit (GEO) at 35786 km of altitude from Earth's equator face a radiation environment mostly composed by the electrons located in the Outer radiation belt and the solar protons arriving during solar proton events [33]. Figure 2.5 shows the presence of GEO orbit in the periphery of the Outer radiation belt.

In GEO, internal charging is the main source of anomalies and it is due to high energy electrons, as well as total dose effects. Moreover, high-energy solar protons are responsible for single event effects and displacement damage [33]. Meanwhile, low energy electrons are the main cause of spacecraft surface charging [24].

This Section introduces the internal and surface charging risks in GEO, together with some of their risk indicators, that will be studied in detail in Chapter 4.

2.4.1. Internal charging and risk indicators

High-energy electrons in the Earth's radiation belts, typically in the mega-electron volt (MeV) range, present a significant risk of internal satellite charging. Unlike lower-energy

[10] Available at https://wasavies.nict.go.jp/index_e.html

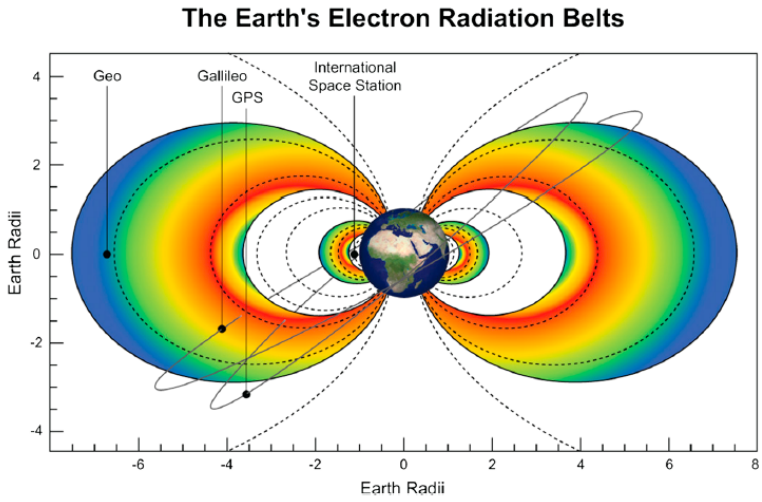

Figure 2.5: Earth radiation belts (electron content) and different orbit locations. Source: Reproduced from [24], with permission from the American Geophysical Union (https://www.agu.org/publications/authors/policies).

particles, these relativistic electrons possess sufficient energy to penetrate the spacecraft's outer skin. Once inside, they can accumulate within insulating materials—such as cables and ungrounded conductors—leading to internal electrostatic charging [24].

This accumulation creates high electric fields within the spacecraft's components. If those fields exceed the dielectric breakdown threshold of the material, they can trigger an electrostatic discharge (ESD). Such discharges may result in permanent damage to the dielectric material, component failure, or the generation of phantom commands that cause uncontrolled spacecraft behavior [24].

Several studies show an important correlation between satellite anomalies and high-energy electron fluence of energy greater than 2 MeV at geostationary orbit [24]. The Space Weather Prediction Center (SWPC) offers the GOES integral electron flux data of energy greater than 2 MeV and emits alerts when it exceeds 1000 particle flux units (pfu), i.e. particles $cm^{-2}s^{-1}sr^{-1}$ [53]. Moreover, the Spanish Space Weather Services (SeNMEs), provided by the Space Weather Group from Universidad de Alcalá, uses an E-Scale with an associated color code, distinguishing quiet, low, moderate, intense and severe activity based on ≥ 2 MeV integral electron flux from GOES [60]. Both the SWPC alert threshold and the SeNMEs E-Scale are represented in Table 2.3.

Electron fluxes at geostationary orbit exhibit distinct spatial variability, that manifests as a diurnal cycle, typically characterized by peak flux intensities near local noon and minima near local midnight. This asymmetry is attributed to the non-uniform structure

of the magnetospheric magnetic field; solar wind pressure compresses the dayside magnetosphere, creating a stronger magnetic field at noon compared to the weaker field found at midnight [53].

High energy electron fluence (flux integrated over time) can also be used as risk indicator, specifically used to assess mode switch anomalies in GEO, with the satellite switching from normal operation mode to a different mode due to a phantom command produced by an ESD. This anomaly took place more than 200 times from 1991 to 2000 and was studied in [71], introducing a traffic light code based on 2-day fluences from GOES-7 data, collected in Table 2.3. The amber color is chosen as the apparent threshold for the anomaly studied, while the 2-days fluence is used because charging times of more than 30 hours were needed to trigger the anomaly [71]. Furthermore, a similar code was introduced in [24] using instead 1-day fluence and it is also represented in Table 2.3. The benefit of this code is to provide early warning for satellite operators to monitor the environment for the next 24 hours [24].

Table 2.3: Internal charging risk criteria. Top: Fluence-based criteria from [71] and [24]. Bottom: Instantaneous flux-based criteria from [60] and [53].

Electron fluence criteria (>2 MeV) for internal charging Accumulation over time ([particles cm^{-2} sr^{-1}])		
Risk Classification	**2-Day Fluence**	**1-Day Fluence**
Low (Green)	$< 10^8$	$< 5 \times 10^7$
Medium (Amber)	$10^8 - 10^9$	$5 \times 10^7 - 5 \times 10^8$
High (Red)	$\geq 10^9$	$\geq 5 \times 10^8$

Electron flux criteria (>2 MeV) for internal charging Real-time intensity ([pfu = particles cm^{-2} s^{-1} sr^{-1}])	
E Scale (SeNMEs)	**Flux Threshold**
Quiet (Green)	$< 10^3$
E1 – Low (Yellow)	$10^3 - 10^4$
E2 – Moderate (Orange)	$10^4 - 10^5$
E3 – Intense (Red)	$10^5 - 10^6$
E4 – Severe (Dark Orchid)	$\geq 10^6$
SWPC alert threshold	$\geq 10^3$

2.4.2. Surface charging and risk indicators

Surface charging is the other significant risk in terms of satellite charging in GEO and is mainly due to low energy electrons, whose population in such orbit increases considerably during geomagnetic activity.

In sunlight, there is a balance of currents between the satellite and the surrounding plasma, with incident charged particles and backscattered or emitted particles and photoelectrons. A positive potential is created, which attracts electrons back, remaining in an equilibrium state and forming a sheath around the satellite. However, when substorms take place, electrons of energies of tens of kilo-electron volts are injected into the magnetosphere and may stick to the satellite surface, creating large negative potentials. This, in addition to only part of the satellite being in sunlight, can cause a high difference of potential along the surfaces of the spacecraft. The consequent electric field can then result in an electrostatic discharge (ESD) if it overcomes the breakdown field of the materials, potentially causing damage to the surface or underlying components of the satellite [24]. The absence of sunlight during eclipses becomes then also a risk factor for satellite charging [11, 36].

During substorms, those low energy electrons from the magnetotail are injected into the near Earth region, specially in local midnight and early dawn [11, 24]. This dependence between geomagnetic activity and the enhancement of the low energy electron population implies a high correlation between the Kp coefficient and the electron flux of less than 100 keV, which is supported by GEO anomalies analysis [11]. In general, anomalies related to surface charging are more likely to occur during higher values of Kp, between midnight and dawn, during the equinoxes and the decreasing phase of solar cycle [11, 36, 63].

Risk indicators for surface charging are also derived from electron flux measurements in the Literature. [63] analyzes 13 years of data from the Los Alamos National Laboratory (LANL) geosynchronous satellites and extracts and finds out a threshold of $1.4 \cdot 10^3$ particles cm^{-2} s^{-1} sr^{-1} eV^{-1} for 8 keV electron flux associated with surface charging risk. Furthermore, [36] concludes from the analysis of 16 years of LANL data that surface charging events are highly correlated with electron flux between 10 and 50 keV, and defines two ESD risk levels thresholds from that flux: significant risk begins at $1 \cdot 10^8$ pfu while high risk at $2 \cdot 10^8$ pfu. These thresholds are summarized in Table 2.4.

Table 2.4: Surface charging risk criteria derived from LANL data. Top: Differential flux threshold (8 keV) from [63]. Bottom: Integral flux thresholds (10–50 keV) from [36].

Differential electron flux criteria (8 keV) for surface charging Real-time intensity ([particles cm^{-2} s^{-1} sr^{-1} eV^{-1}])	
Risk Classification	**Flux Threshold**
Charging Threshold	$\geq 1.4 \times 10^3$

Integral electron flux criteria (10–50 keV) for surface charging Real-time intensity ([pfu = particles cm^{-2} s^{-1} sr^{-1}])	
Risk Classification	**Flux Threshold**
Significant Risk	$\geq 1 \times 10^8$
High Risk	$\geq 2 \times 10^8$

2.5. Geomagnetic indices

Geomagnetic activity takes place as a consequence of the interaction of solar activity and the Earth's magnetosphere and it can lead to several impacts in technology as was presented in Section 2.2.1. The objective of the present Section is to introduce the geomagnetic indices, particularly the K index and its computation, as the premise for Chapter 5.

As defined by ISGI (International Service of Geomagnetic Indices), the aim of the geomagnetic indices is to describe geomagnetic activity or some of its components [29]. This includes six different indices (aa, am, Kp, Dst, PC, auroral indices) that relate to different magnetospheric phenomena and are endorsed by the International Association of Geomagnetism and Aeronomy (IAGA) [29] . Many more indices exist and allow to measure geomagnetic activity variations in a wide range of time resolution, units and Earth regions.

Three of the IAGA endorsed indices, aa, am and Kp are K-derived planetary indices and aim at measuring global geomagnetic activity in three hour intervals, using data coming from stations located at around $\pm 50°$ of latitude [29]. On the other hand, the Dst index (disturbance storm-time) is an equatorial index that monitors the axis-symmetric (with respect to the geomagnetic field dipole axis) magnetic signature of the magnetospheric currents from equatorial stations data and allows to detect magnetic storm events and

indicate their intensity [29, 69]. The PC (polar cap) index quantifies geomagnetic activity in the polar caps and uses data from polar stations [29]. Finally, the auroral indices (AE, AU, AL, AO) measure the auroral electrojet activity in the northern auroral zone, using data from 12 stations at around 60°-70° of latitude [29].

2.5.1. The geomagnetic disturbance index, K

The planetary geomagnetic disturbance index, or simply, Kp index, aims therefore at globally monitoring subauroral geomagnetic disturbance [35]. Its real time values, as well as its forecast for the three consecutive days, are provided by the Helmhotz Center for Geoscience (GFZ) in [22]. Figure 2.6 shows the values of the Kp index, expressed in 3 hour intervals, during the most recent solar storm at the moment of writing, in January 2026. The geomagnetic disturbance measured by this index includes phenomena like geomagnetic pulsations, bays or substorms, sudden commencements, geomagnetic storms (excluding the recovery phase) and fast changes in magnetospheric currents, and the effects of these disturbances, called K-variations, manifest within intervals of less than 3 hours [35]. Meanwhile, geomagnetic activity that does not include geomagnetic disturbances is composed by phenomena related to regular electromagnetic solar radiation with periods of variation longer than 3 hours, and is typically known as the quiet curve [35].

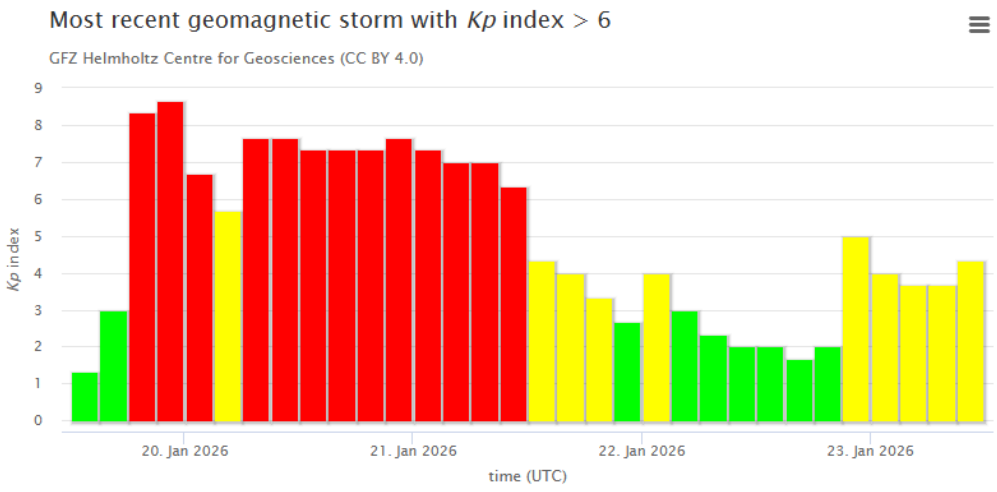

Figure 2.6: Kp values by GFZ during the solar storm of January 2026. Source: [22].

This Kp index is built from the measurements of 11 northern and 2 southern geomagnetic observatories located in auroral latitudes (between 44° and 60°), whose local K indices are computed, standardized and averaged to produce such global index [29, 35]. Each observatory can produce a local K index, defined on 3 hour intervals of the UT day (0-3,

3-6, 6-9, 9-12, ...) and is computed from the horizontal components of the measured magnetic field. Typical configurations for the geomagnetic measurements are XYZ (X along the geographic north and Y along the geographic East) and HDZ (H along the local magnetic north and D along the local magnetic East). To derive the K index, the quiet curve has to be estimated for the horizontal geomagnetic components and subtracted to them, in order to obtain the geomagnetic disturbance [35]. For every 3 hour interval, the horizontal component with a higher disturbance variation is selected and converted from nanoTesla (nT, as typical unit for geomagnetic measurements) to the quasi-logarithmic K index scale from 0 to 9. The nT range values to transform to the K scale are specific for each observatory and are proportional to a reference observatory (Niemegk, Germany). This proportionality is defined by a K9 value, characteristic of each observatory, such that the frequency distribution of the possible K values is as close as possible to the one from Niemegk, where K2 to K4 happen for more than 50% of the cases [35]. Figure 2.7 shows the K9 limits of different stations[11] located all around the globe, ordered by corrected geomagnetic latitude and with information about the station altitude. It can be seen the exponential increase in K9 with the magnetic latitude, while altitude does not have a clear effect on it. This behavior is due to the proximity of higher latitude stations to the magnetic poles, where the magnetospheric shielding is thinner and therefore geomagnetic variations show stronger effects.

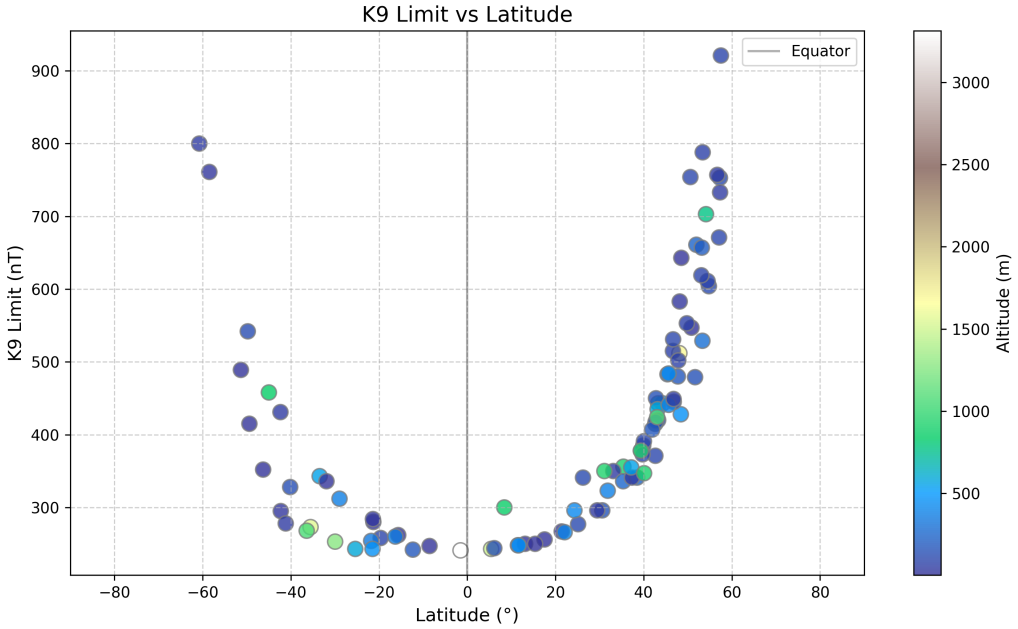

Figure 2.7: K9 limits for different geomagnetic stations according to their corrected geomagnetic latitude.

[11] Data from the ISGI stations database in https://isgi.unistra.fr/mapobs.php

It is known that local geomagnetic activity, and therefore the local K indices, depend on local time and season [35]. Outside the auroral zone, geomagnetic disturbances are higher before or around local midnight than before or around local noon. Within the auroral zone, these variations are even higher [4]. That dependence in local time justifies the need of the standardization of local K indices (which become Ks indices) as a previous step before averaging and computing Kp. Nevertheless, the utility of those Ks indices is only for Kp calculation, and locally the K index is the correct indicator [4].

The most complex part about the local K index computation is the quiet curve estimation, concerning geomagnetic activity that is not related to disturbances, but rather to regular, slower changes; and together with those disturbances they compose the total geomagnetic activity, which is measurable from the stations in terms of the local magnetic field components. IAGA endorses four algorithms to compute the quiet curve: FMI method (Finnish Meteorological Institute), ASM (Adaptive Smoothing Method), LRNS (Linear-Phase Robust Non-Linear Smoothing) and USGS method (United States Geological Survey). All of them produce the K index values based on the two horizontal components of the magnetic field, excluding the Z component. GFZ uses the FMI algorithm to compute the local K indices of the 13 stations contributing to Kp with their 1 minute magnetic field measurements [35].

2.5.2. INTERMAGNET

INTERMAGNET is the global net of Earth's magnetic field monitoring observatories. It allows collaboration between geomagnetic observatories to provide data in near real-time and establishes standard specifications for the equipment and measurements. The INTERMAGNET website offers a data viewer and download, and data is also available through the Heliophysics data API (HAPI). Data typically include the three magnetic field components and the magnitude, as measured by each station [27]. Figure 2.8 displays as an example the geomagnetic data from the San Pablo observatory in Toledo (Spain) from 18 to 22 January 2026, particularly X, Y, Z components and the magnitude of the magnetic field, from top to bottom. The effects of the geomagnetic storm are perceptible from the end of 19th January with increases of around 300 nT for the X component and 150 nT for the Y component, and subsequent variations in the measurements.

The network of observatories composing INTERMAGNET includes more than a hundred observatories all around the globe. It can be seen in Figure 2.9 that the majority of stations are gathered in Europe and North America, while some regions like Africa, the middle East and Center Asia, as well as the oceans only harbor a small number of them.

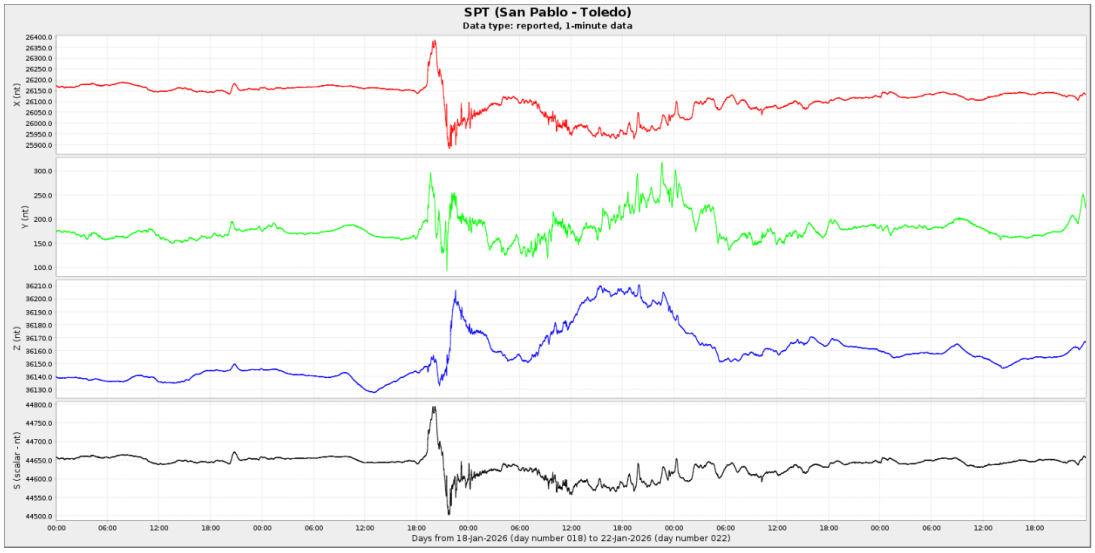

Figure 2.8: Geomagnetic data from San Pablo observatory (Toledo, Spain) from 18 to 22 January 2026. Source: INTERMAGNET [27].

The data provided by the stations are offered in a 1 minute and a 1 second basis, even if many of the stations might show data gaps or not offer data during some periods. Furthermore, the majority of stations work in near-real time, but some of them perform a temporary data embargo generally of 1 day (i.e one day of delay in data availability). A few stations belonging to INTERMAGNET are closed for the moment.

2.5.3. Efects of geomagnetic disturbances

As described in Section 2.2.1, the impacts of the geomagnetic storms can be assessed through the NOAA's G scale, that allocates the range of effects and their intensity to different values of the Kp index.

The effects associated to each value of the G scale are reproduced in what follows directly from NOAA's documentation [48]:

G5 (Extreme) – $Kp = 9$ **Power systems:** Widespread voltage control problems and protective system problems can occur; some grid systems may experience complete collapse or blackouts. **Spacecraft:** Extensive surface charging, problems with orientation, uplink/downlink, and tracking satellites. **Other:** Pipeline currents can reach hundreds of amps, HF radio propagation may be impossible for days, satellite navigation degraded, and aurora seen as low as 40° of geomagnetic latitude.

G4 (Severe) – $Kp = 8$ **Power systems:** Possible widespread voltage control problems and some protective systems will mistakenly trip out key assets from the grid.

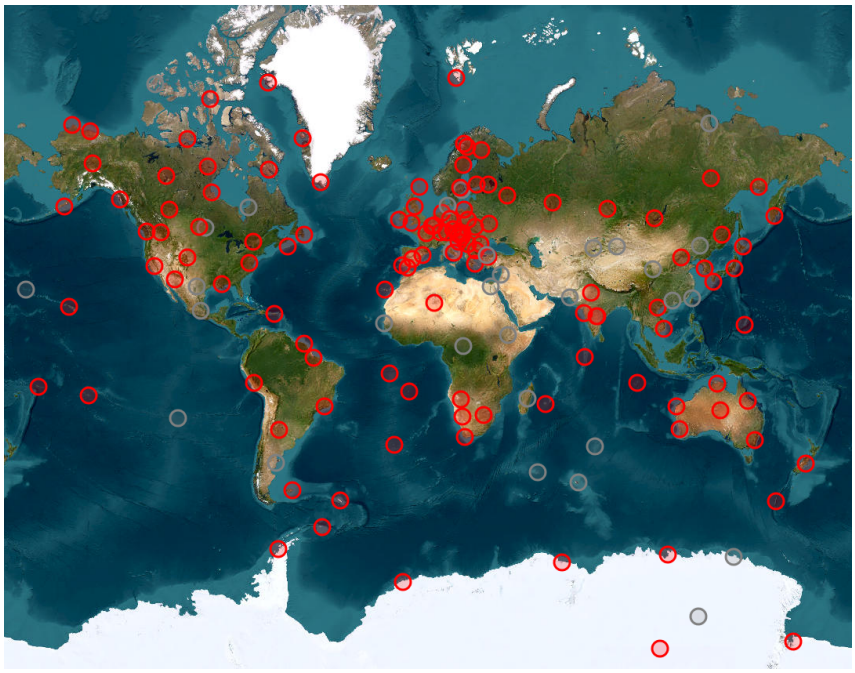

Figure 2.9: Stations belonging to INTERMAGNET. Red dots denote open stations, while grey dots denote closed ones. Source: INTERMAGNET [27].

Spacecraft: Surface charging and tracking problems; corrections may be needed for orientation. **Other:** Induced pipeline currents affect preventive measures, HF radio propagation sporadic, satellite navigation degraded for hours, and aurora seen as low as 45° of geomagnetic latitude.

G3 (Strong) – $Kp = 7$ **Power systems:** Voltage corrections may be required; false alarms triggered on some protection devices. **Spacecraft:** Surface charging may occur on components; drag may increase on low-Earth-orbit satellites. **Other:** Intermittent satellite navigation and low-frequency radio navigation problems; aurora seen as low as 50° of geomagnetic latitude.

G2 (Moderate) – $Kp = 6$ **Power systems:** High-latitude power systems may experience voltage alarms; long-duration storms may cause transformer damage. **Spacecraft:** Corrective actions to orientation may be required by ground control; drag affects orbit predictions. **Other:** HF radio propagation can fade at higher latitudes; aurora seen as low as 55° of geomagnetic latitude.

G1 (Minor) – $Kp = 5$ **Power systems:** Weak power grid fluctuations can occur. **Spacecraft:** Minor impact on satellite operations possible. **Other:** Migratory animals are affected; aurora is commonly visible at high latitudes.

3 | Radiation dose estimation at flight altitudes

As introduced in Section 2.3, the radiation dose level at flight altitudes is an important operational impact of Space Weather on human health and electronic devices. To assess this impact, a tool to compute effective dose rates in near-real time has been developed, as well as for post-flight analysis. The tool integrates already existing algorithms and models in order to provide an example of operational dose rates assessment.

3.1. Method

The tool implements the following:

- Download and parsing of neutron count rates data from several neutron monitor (NM) stations, available at the Neutron Monitor Database, NMDB (see Section 2.3.3).
- Analysis of neutron count rates to detect whether a ground level enhancement (GLE) event is taking place or a Galactic Cosmic Ray (GCR) only situation is happening (see Sections 2.2.4 and 2.2.5). This is applied through the implementation of the GLE Alert+ algorithm (see Section 2.3.4). This algorithm for GLE detection has been implemented in two different ways, to detect both the beginning and the end of the event.
- Computation of effective dose rates through AniMAIRE model (see Section 2.3.5) using the neutron count rates as proxies for the particle spectra. This spectra is used for effective dose calculations inside the model.
- Compute operational indicators (D-Index, ICAO and FAA alert levels, see Section 2.3.2) from effective dose rates.

The scheme displayed in Figure 3.1 shows how the tool works. Its parameters have been defined through a series of preliminary studies, collected in the following Sections.

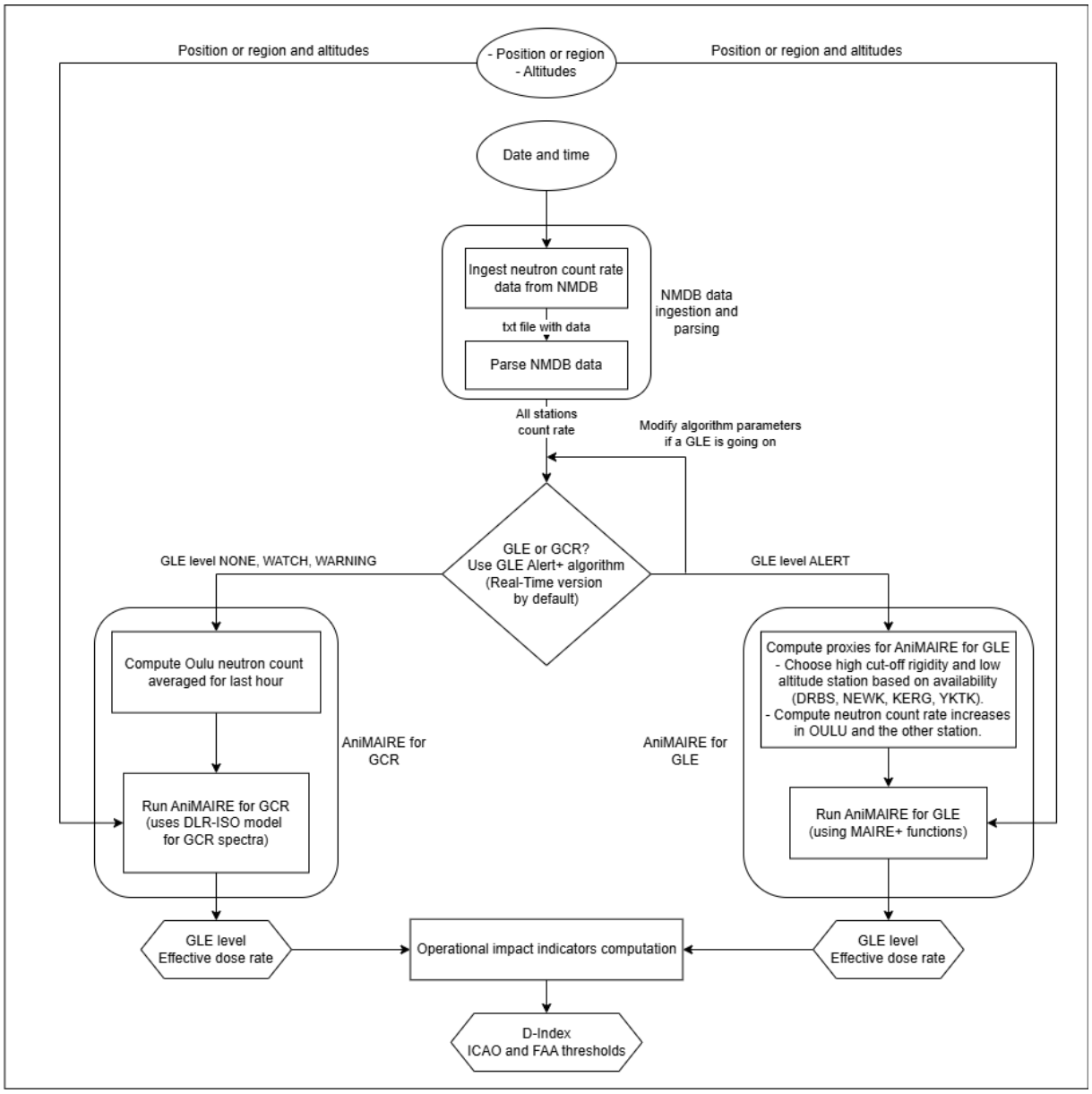

Figure 3.1: Scheme of the developed tool for continuous operation (nowcast)

The tool can be used for nowcast of radiation dose rates at certain altitudes. A single position or a whole region over the globe can be chosen, selecting the resolutions in latitude and longitude. One or several altitudes can also be chosen.

Using the tool for nowcast of radiation dose rates and alert levels starts with an automatic download of neutron count rates data from NMDB, retrieving data from all the available stations at that moment.

The GLE Alert+ algorithm is then applied to detect whether a GLE event is going on. Two versions of the algorithm are implemented, according to the need of detecting a GLE

or detecting the end of it once it has started. This was decided according to the study in Section 3.1.2.

If there is no GLE on going, a GCR scenario is assumed and Oulu neutron count is the only proxy needed for the effective dose computation by using AniMAIRE model. It should be noted that Oulu (located in Finland) is one of the neutron monitor stations in NMDB. The last one hour average Oulu neutron count is computed from the downloaded data from NMDB. When computing the effective dose rate map by AniMAIRE, due to the slow variation of GCR incidence, the same dose rate map can be assumed to be valid for longer periods of time, e.g. one hour. Some models like WASAVIES even provide the same GCR dose map for a whole day. This parameter can be chosen by the user according to the desired accuracy.

Otherwise, if a GLE is detected, AniMAIRE model is used with the MAIRE+ proxies, which are the neutron count rate increases in two different stations. The selection of the stations is described in Section 3.1.3.

It shall be noticed that AniMAIRE model uses the mentioned proxies to build the spectra of particles arriving to the magnetosphere, utilizing magnetospheric computations for particle trajectories and pre-calculated yield functions to determine effective dose rates.

For both cases, GLE detected or not, the effective dose rate is calculated. Also, the D-index (in GCR scenario it is always zero by definition) is calculated, and comments on whether the ICAO or FAA alert levels are overcome are also shown. The GLE level is shown as well, as *watch* and *warning* messages may indicate that a GLE is about to happen.

It is also important to notice that planetary K index (Kp) is an input to the AniMAIRE model for GCR and GLE scenarios, used to characterize the geomagnetic field and can be introduced manually. However, if it is not introduced, it is automatically retrieved by AniMAIRE library for the introduced date, through Celestrak data. In the tool the automatic use of Kp is used for simplicity.

Results are represented in Section 3.2. The results and studies are expressed in terms of effective dose rates in $\mu Sv/h$, as it is the main value used in the different models. Also dose equivalent and ambient dose equivalent can be obtained as output from AniMAIRE functions, as well as neutron fluxes, SEU and SEL rates, even if they are not considered by the tool at the moment (see Section 2.3.1 for radiation dose indicators and Section 2.3.5 for AniMAIRE outputs).

3.1.1. Preliminary study of AniMAIRE for GCR model

In this study, effective dose rates in a GCR scenario will be compared using three different models: WASAVIES, NAIRAS and AniMAIRE. The objective is the validation of the models by mutual comparison and the definition of the limits of use in terms of flight altitudes for the models.

Effective dose rates for a time during a quiet day (2025/11/27 at 00:00:00UT) will be compared for a global region. The data for NAIRAS model over the globe is only available for 20 km of altitude and it is represented in Figure 3.2 It shall be noted that NAIRAS data is offered each hour and uses hourly-averaged data from four different neutron monitor stations.

The same map is represented by using WASAVIES at 18 km (Figure 3.3). This model only offers one GCR map per day, obtained from the daily-average count rates from 13 neutron monitors [47].

Finally, the map is represented by using AniMAIRE at 20 km (Figure 3.4). It should be recalled that AniMAIRE for GCR uses Oulu count rate averaged during the previous hour.

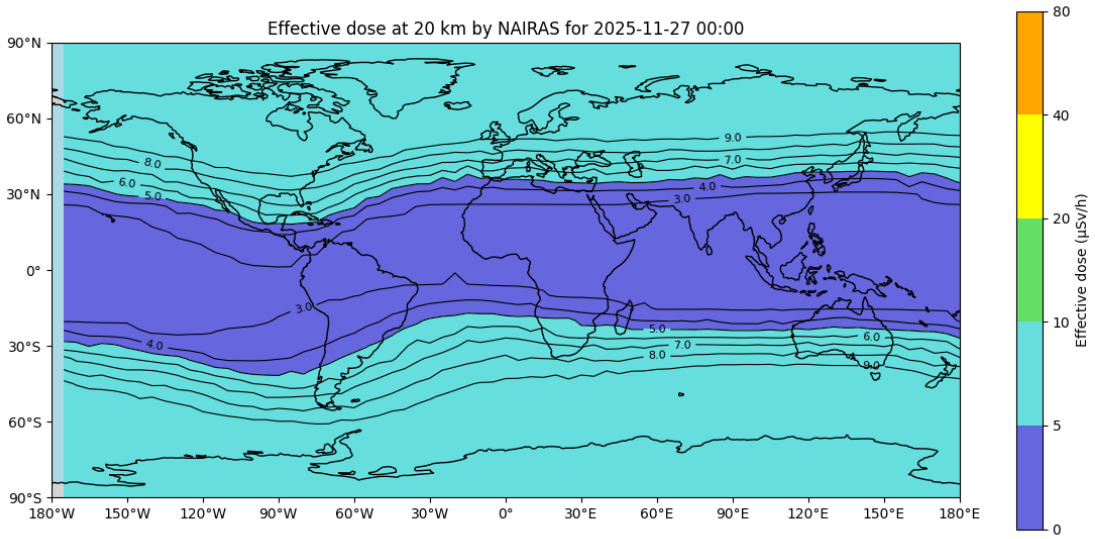

Figure 3.2: Effective radiation dose at 20 km from NAIRAS model

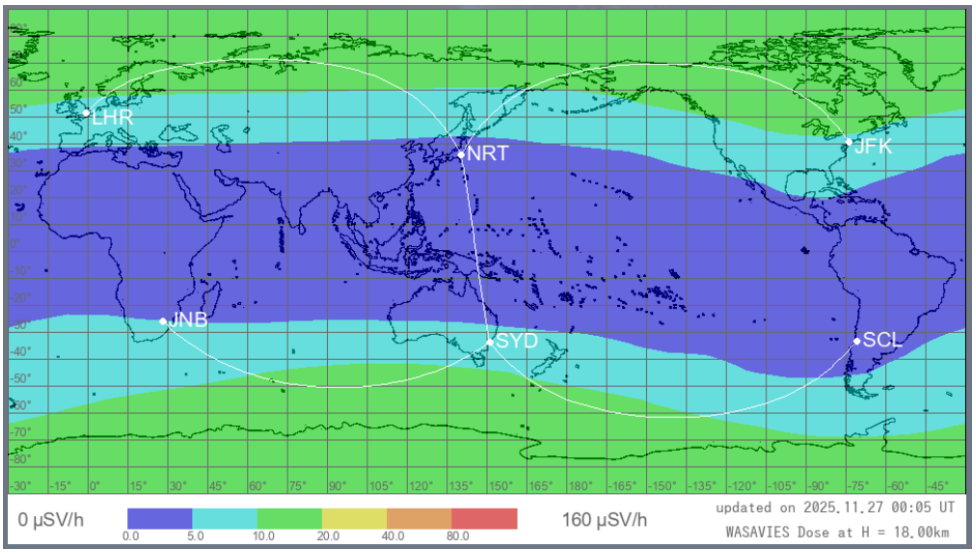

Figure 3.3: Effective radiation dose at 18 km from WASAVIES model. Source: WASAVIES, NICT [47].

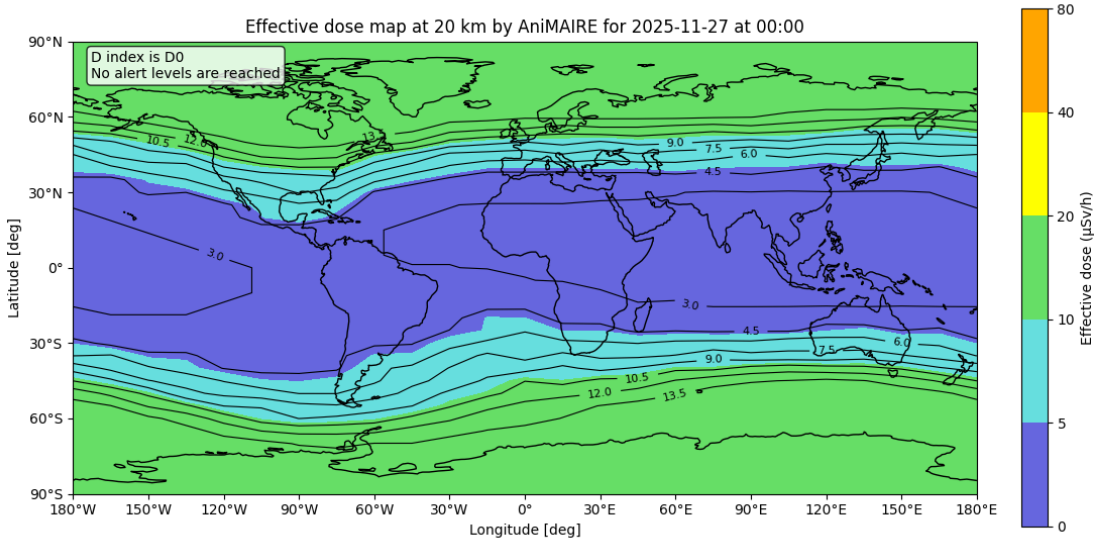

Figure 3.4: Effective radiation dose at 20 km from AniMAIRE model

Comparison of the results show that effective dose rates contour lines follow similar paths along the globe, while differences are perceptible concerning the value of the dose rates. The 10 to 20 $\mu Sv/h$ interval in WASAVIES corresponds to an interval from 12 to 14 $\mu Sv/h$ in AniMAIRE and from 9.6 up to less than 10 $\mu Sv/h$ in NAIRAS. The 5 to 10 $\mu Sv/h$ interval in WASAVIES corresponds to to an interval from 4.5 to 12 $\mu Sv/h$ in AniMAIRE and from 5.6 to 9.6 $\mu Sv/h$ in NAIRAS. Finally, the 0 to 5 $\mu Sv/h$ interval

in WASAVIES corresponds to an interval from 3 to 4.5 $\mu Sv/h$ in AniMAIRE and from 2 to 5.6 $\mu Sv/h$ in NAIRAS. Therefore, agreement of the models is quite good, noticing specially that all of those effective dose rates represent no threat as they remain under both the ICAO and FAA alert thresholds (30 and 20 $\mu Sv/h$, respectively).

Furthermore, as 20 km represent the specified limit of validation of MAIRE+ model according to [23] (which is the basis of AniMAIRE model and uses the same method to compute GCR dose rates), a comparison between the results obtained for higher altitudes with the ones available from WASAVIES is done (the results adn their discussion can be consulted in Appendix A.1). WASAVIES model is valid up to 86 km according to [58] and is offered up to 96 km on WASAVIES website ([47]). After the comparison, it can be concluded that for 30 km of altitude, agreement between both models is still good, at least in terms of orders of magnitude. Meanwhile, for 56 and 94 km, AniMAIRE keeps obtaining similar results that for lower altitudes, with maximum values under 30 $\mu Sv/h$, while WASAVIES shows maximum values of more than 40 $\mu Sv/h$. Attending to the validated altitude limits of both models in their respective papers, these differences imply that AniMAIRE is limited to altitudes of around 30 km when used in GCR mode, being more accurate for less altitude.

3.1.2. Preliminary study on GLE detection

A preliminary study assessing GLE detection through the application of the GLE Alert+ algorithm has been arranged to identify the algorithm behavior for the most recent GLE cases. This algorithm was proposed in [62], based on previous works as [30] and [37]. It is purely based on neutron monitoring data extracted from the Neutron Monitor Database (NMDB).

This algorithm proposes a method for GLE detection based on a moving mean and some parameters to compute a moving threshold for each neutron monitor station, which compared with the last count rate at each station determines whether a GLE is going on or not. The implementation of the algorithm is as follows.

At each step of the algorithm two windows of time are defined: a first window of duration τ_m to compute the mean of the neutron counts and a second window of duration τ_r to assess the most recent time instants. Another parameter τ_d indicates when the computation of the mean ends with respect to the current time instant t. For each t belonging to the τ_r-window, its corresponding moving mean $M(t)$ is computed as:

$$M(t) = \frac{1}{\tau_m} \sum_{\tau=t-\tau_m-\tau_d}^{t-\tau_d} N(\tau) \tag{3.1}$$

where $N(\tau)$ is the neutron count rate at τ.

Using this mean, at each time instant t, the moving threshold $T(t)$ is computed as:

$$T(t) = M(t) + n\sigma(t) \tag{3.2}$$

where $\sigma(t)$ is the standard deviation of $M(t)$ and n is a parameter whose optimal values for each station (39 stations are considered) are collected in [62].

Therefore, at each time instant of the τ_r-window and for each station, $N(t)$ will be compared to its corresponding moving threshold. For a station to be considered in alert state, $N(t) > T(t)$ is required for at least three consecutive time instants belonging to the τ_r-window. To identify a GLE, the state of all the stations is compared for the τ_r-window: if there is only an alert for one station, the general status is called *watch*; two stations in alert define a *warning* status and three or more stations in alert imply a general *alert* status. In this last case a GLE is considered to be going on.

Two versions of the algorithm are considered. The first one, referred to as *Real-Time*, uses the optimal values of the parameters proposed in [62], i.e, $\tau_m = 60$ minutes, $\tau_d = 5$ minutes and $\tau_r = 15$ minutes. On the other hand, a so-called *Long Previous Time* version of the algorithm is also used to assess GLE detection. This last version uses a value of $\tau_d = 20$ hours and the same values as before for $\tau_m = 60$ minutes and $\tau_r = 15$ minutes. Its purpose is to compute the mean before the GLE start, so the increased values of neutron count rates during the GLE do not affect mean computation.

Both algorithms are used to assess GLEs 72 to 77 (occurred from 2017 to 2025). The Figure 3.5 shows the results of the number of stations that are on alert level over time for both configurations of the GLE Alert+ algorithm (Real-time and Long Previous Time) during GLE 77. Data from GOES integral proton flux is also represented on the Figure 3.5 as a complementary proxy for GLE detection. Up to four channels of integral proton flux are included in proton flux units (1 pfu = 1 proton $cm^{-2}s^{-1}sr^{-1}$), referring to protons of more than 10 MeV, 50 MeV, 100 MeV and 500 MeV. Two thresholds are included within the GOES data: 10 pfu define the limit for a proton flux of more than 10 MeV to consider S1 in S-Scale and therefore a non-quiet situation in terms of solar radiation storms; meanwhile 1 pfu for proton flux of more than 100 MeV is used together with

neutron count to detect a GLE in tools like WASAVIES [58].

It is important to notice that GLEs normally take place during solar radiation storms events, but a solar radiation storm does not necessarily unchain a GLE, therefore GOES proton flux cannot be a proxy on its own and neutron count rates are needed to determine whether such an event is happening, as they characterize the particle environment inside the atmosphere. Nevertheless, GOES proton flux can be used as a necessary condition to trigger a GLE detection and avoid false positives based on neutron count rates.

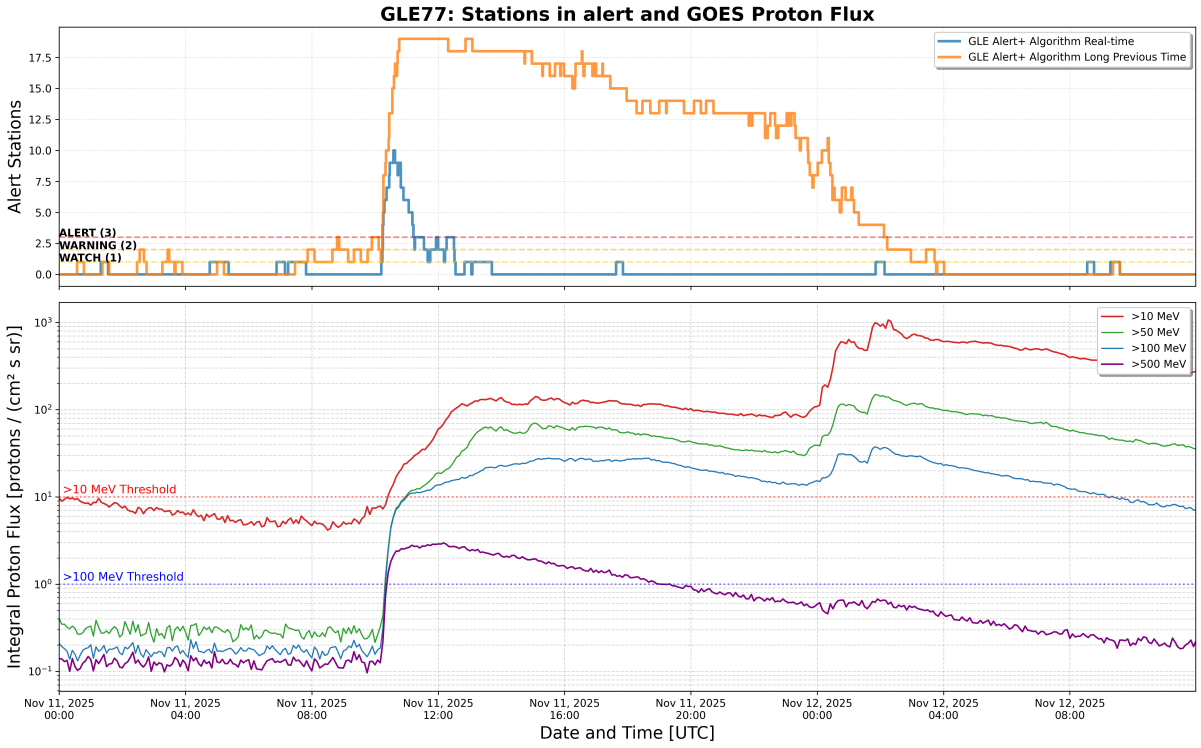

Figure 3.5: GLE detection and GOES proton flux during GLE 77

In Figure 3.5, both versions of GLE Alert+ algorithm are able to detect the GLE. While the Real-Time version quickly stops the alert level as it begins using the increased count rates to compute the mean, the Long-Previous Time version is able to capture the GLE duration as it computes the mean enough time before the GLE start. Meanwhile, integral proton fluxes measured by GOES experiment a sudden big increase for all the energy levels, overcoming the >100 MeV threshold and then slowly decreasing, but taking a longer time to recover its original state than the duration of the GLE.

Figures in which the detection of the other studied GLEs (GLE 72, 73, 74, 75, 76) is represented are shown and discussed in the Appendix A.2, where they can be consulted to complement the selected results. A summary of the detection results for all the studied

GLEs is depicted in Table 3.1, that indicates whether each event was detected by the Real-Time and Long Previous Time algorithms, and if the GOES proton flux exceeded the 1 pfu threshold for the >100 MeV channel.

Table 3.1: Summary of detection results for GLEs 72-77.

Event	**Detection by Real-Time GLE Alert+ algorithm**	**Detection by Long Previous Time GLE Alert+ algorithm**	**GOES proton flux >100 MeV over 1 pfu**
GLE 72 (2017/09/10)	NO	YES	YES
GLE 73 (2021/10/28)	YES	YES	YES
GLE 74 (2024/05/11)	YES	NO	YES
GLE 75 (2024/06/08)	NO	NO	YES
GLE 76 (2024/11/21)	NO	NO	YES
GLE 77 (2025/11/11)	YES	YES	YES

From the obtained results, the following conclusions are achieved:

- The *Real-Time* version of the GLE Alert+ algorithm detects 3 of the 6 assessed GLEs (73, 74, 77) and is only suitable to detect the beginning of the event.
- The *Long Previous Time* version of the GLE Alert+ algorithm detects also 3 of the 6 GLEs (72, 73, 77) and catches the duration of the GLE.
- The *Real-Time* version of the GLE Alert+ algorithm is able to catch the Forbush decrease that preceeded GLE 74, while *Long Previous Time* version failed to catch it. This is due to the fact that GLE 74 consisted on a sudden increase in neutron count rates after the Forbush decrease that affected previous neutron count rates.
- GLEs 75 and 76 could not be captured by any of the versions of the algorithm, as the increases experienced in neutron count rates were not high enough.
- GOES proton flux of more than 10 MeV and 100 MeV overcome their thresholds of 10 pfu and 1 pfu, respectively, for all the GLEs. The time instants at which GOES proton fluxes overcome their corresponding thresholds agree perfectly with the times of detection of the GLEs and with the highest peaks in stations in alert in the cases where no GLE was detected.

- GOES proton flux of more than 500 MeV does not surpass any clear threshold through the different cases, so no trigger mechanism can be extracted from it.
- GOES proton flux does not catch the end of GLE events, as they stay in many cases over the thresholds for a longer time than duration of the GLEs.

In conclusion, it has been decided that the *Real-Time* version of GLE Alert+ Algorithm is suitable to detect the beginning of the GLE, while the *Previous Long Time* version can be used to control the duration of the GLE and trigger the comeback to GCR scenario.

GOES proton flux data for protons of more than 100 MeV is a useful proxy to confirm the presence of a GLE. By examining data for other cases when there was no GLE event[1], like 2024/10/09, 2024/07/23, 2024/02/12 and 2022/01/21, as examples, the 100 MeV threshold of 1 pfu was exceeded. Figures justifying this are collected and discussed in Appendix A.4. Therefore, it could be used as confirmation of the beginning of the GLE to avoid false positives coming from neutron count increases data, but not as a single proxy for GLE detection.

The use of GOES proton flux data would improve the behavior of the algorithm, as thresholds for neutron count rates increase could be lowered in order to detect weaker GLE events, like GLE 75 and GLE 76. However, this would imply adding another data source to the tool, with the consequent complexity and computational cost. To take a decision about using this data or not, the performance of the radiation dose computation model will be studied (in Section 3.1.3). The objective is to know whether dose rates computed with GLE model and GCR model during the weak GLE events differ much to each other.

3.1.3. Preliminary study on GLE scenario dose computation

The following study consists on a comparison of the maximum effective dose rates computed using AniMAIRE model (in GCR and GLE scenarios) and from NAIRAS model during GLEs 73 to 77. The comparison is done at 5, 11, 15, 20 and 40 km of altitude, as those are the altitudes for which NAIRAS provides values. NAIRAS data is only available at NASA CCMC[2] from 2021, so GLEs that took place before GLE 73 (i.e. 2021) cannot be assessed using this model. Furthermore, maximum effective dose rates obtained from the Statistical Models developed in [44] and [31], derived from simulations using the CRAC:DOMO model are also compared with the results. The mentioned models are

[1] Data available at Space Weather Data Portal: https://lasp.colorado.edu/space-weather-portal/.

[2] Available at https://ccmc.gsfc.nasa.gov/models/NAIRAS~3.0/

explained in more detail in Section 2.3.5.

The objective of this study is to determine whether it is reasonable to assess a weak undetected GLE using AniMAIRE in GCR mode instead of GLE mode, as well as to compare both results with the other mentioned models. The conclusions are needed to choose for the detection model between only using the GLE Alert+ algorithm or adding the GOES >100 MeV proton flux data as a confirmation proxy.

AniMAIRE using MAIRE+ logic to compute effective dose rates during GLE events needs to use as input the increase in neutron count rate of Oulu station and another station of higher cut-off rigidity (more than 1 GV) and low altitude, according to [23]. Oulu is considered to be a very reliable station in terms of data supply and all the outputs from AniMAIRE model depend on that station (both for GLE and GCR cases). Meanwhile, by default, according to [23], Dourbes (DRBS) is used as the second station, which optimizes the quality of the results for British airspace, but still provides good results for the rest of the globe. Other stations that could be used instead of Dourbes, would be Newark (NEWK), Kerguelen (KERG) and Yakutsk (YKTK), due to their cut-off rigidity and altitude, similar to Dourbes. All the mentioned stations are summarized in Table 3.2. This becomes a need for effective dose rate estimation during GLE events as any of these stations has been operative during all the studied events.

Table 3.2: Summary of Neutron Count Station Parameters.

Station Code	**Cut-off rigidity (GV)**	**Latitude (deg)**	**Longitude (deg)**	**Altitude (km)**
OULU	0.80	65.05° N	25.47° E	0.015
DRBS	3.18	50.10° N	4.60° E	0.225
NEWK	2.40	39.68° N	75.75° W	0.050
KERG	1.14	49.35° S	70.25° E	0.033
YKTK	1.65	62.01° N	129.43° E	0.105

Maximum effective dose rates have been computed for AniMAIRE model using GCR and GLE modes every 10 minutes during the GLE length (taken from the official GLE database ([67]), see Section 2.3.3). The default combination of stations for GLE mode is Oulu and Dourbes, except when the latter is not available, when other stations are used as just described. NAIRAS data are provided each hour, while Statistical Model results are computed at the same time instants as AniMAIRE.

The results are collected in Table 3.3, where a summary of maximum values of effective

dose rates obtained from each model is displayed. These indicators have been selected given their importance in alert generation during the GLE event, as alerts of enhanced effective dose rate values are based in the thresholds explained in Section 2.3.2. Those thresholds are 20 $\mu Sv/h$ for FAA's alert, 30 $\mu Sv/h$ for ICAO's moderate alert and 80 $\mu Sv/h$ for ICAO's severe alert. Figures 3.6 and 3.7 represent the whole GLE analysis for two selected examples, particularly GLE 75 at 20 km and GLE 77 at 11 km, which are representative of two possible situations concerning GLE events (weaker and stronger events). A more detailed look at the whole GLE analysis (GLEs 73 to 77 at altitudes of 11, 15 and 20 km) can be consulted in Appendix A.3.

Figure 3.6 shows the evolution of the maximum effective dose rates values along GLE 75 at 20 km of altitude. These values have been computed by AniMAIRE in GLE (with two different combination of stations) and GCR mode, and obtained from NAIRAS. Effective dose rates from GLE mode using both different combinations of stations share the same baseline, around the 20 $\mu Sv/h$ value of FAA alert, but the OULU+NEWK set captures higher values at some points, reaching also ICAO's 30 $\mu Sv/h$ moderate alert level. While effective dose rates computed considering GCR only stays under alert levels all the time, NAIRAS reaches its maximum values over the 30 $\mu Sv/h$ threshold. The combination of OULU+NEWK therefore produces closer results to NAIRAS in this case, even if both combinations of stations would display alerts.

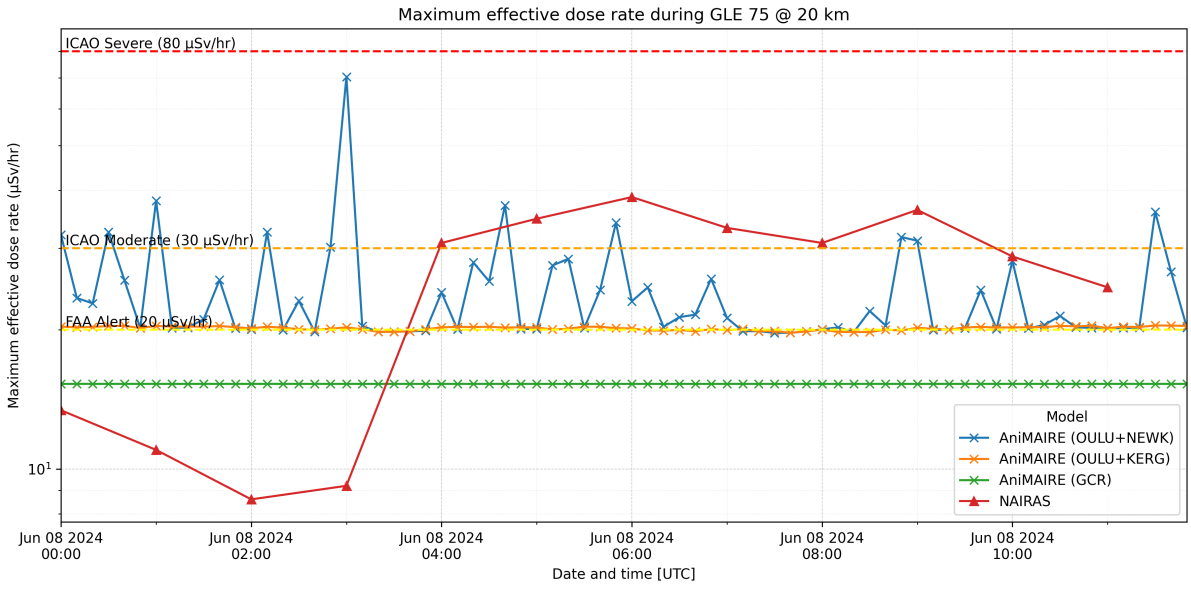

Figure 3.6: GLE results comparison at 20 km for various models during GLE 75

Figure 3.7 represents the evolution of maximum effective dose rates during GLE 77 at 11 km of altitude. While AniMAIRE for GCR stays in very low values, AniMAIRE for

GLE (with the default combination of stations, OULU+DRBS) and the Statistical Model based on CRAC:DOMO simulations show good agreement at the first peak, both of them reaching the 30 $\mu Sv/h$ threshold, even if the latter stays for a longer time over that level. Meanwhile, AniMAIRE for GCR does not capture the higher values of GLE mode and NAIRAS does not reach much higher values than 20 $\mu Sv/h$.

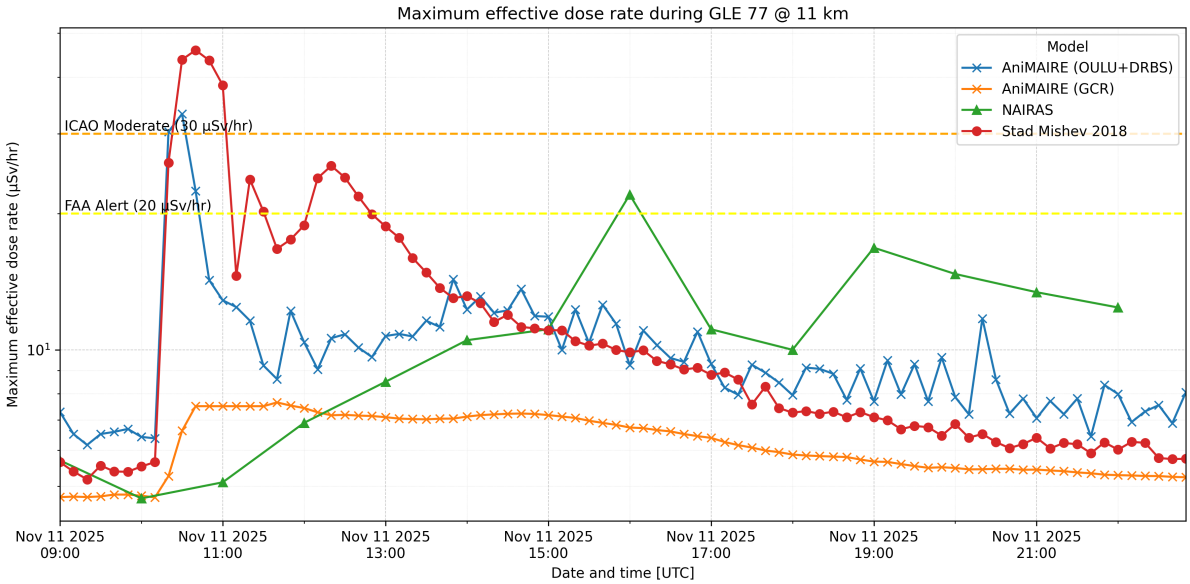

Figure 3.7: GLE results comparison at 11 km for various models during GLE 77

Looking at the maximum values for GLE 75 and 76, it is possible to see that no alert level is reached with NAIRAS up to 15 km of altitude, and GCR mode obtains similar results. At 20 km, NAIRAS reaches alert levels, specially in GLE 75 where the values are over the ICAO Moderate alert for around 6 hours (Figure 3.6). GCR mode for AniMAIRE remains at lower levels, while GLE mode reaches ICAO Moderate alert levels during the whole length of the GLE. It is important to notice that the considered GLE mode results during GLE 76 are the ones computed using OULU and NEWK stations, while OULU and KERG combination does not reach higher values.

GLE 73, which could be captured by the detection algorithm, shows a good agreement between effective dose rates computed through GCR and GLE models, but only the OULU and DRBS combination of stations (which is the considered in the table) reaches alert levels at 15 km, like NAIRAS punctually does. It is noticeable that no information at 20 km of altitude was available for NAIRAS in this case.

Referring to GLE 77, it is clear that GCR mode remains on very low values, while NAIRAS reaches alert levels from 11 km of altitude, and GLE mode overestimates the maximum

Table 3.3: Comparison of maximum effective dose rates calculated by AniMAIRE (GCR and GLE modes), NAIRAS, and the Statistical model for GLEs 73, 74, 75, 76, and 77.

Altitude (km)	**GCR Max** (μSv/h)	**GLE Max** (μSv/h)	**NAIRAS Max** (μSv/h)	**Stat Max** (μSv/h)
GLE 73 (2021/10/28)				
5	1.2180	1.3025	6.8000	–
11	9.6296	12.0480	17.2000	381.9368
15	19.2218	30.0081	22.3000	–
40	64.8397	1626.5920	45.1000	–
GLE 74 (2024/05/11)				
5	0.9484	1.0598	1.1000	–
11	6.6540	7.8186	7.8000	–
15	12.0319	14.7223	18.8000	–
20	16.9716	23.2446	48.4000	–
40	26.1055	187.8263	610.8000	–
GLE 75 (2024/06/08)				
5	1.0349	1.1163	1.2000	–
11	7.5500	9.8752	8.3000	1.6990
15	14.0871	24.5512	17.9000	–
20	20.7909	70.3784	38.7000	–
40	34.9931	1745.1622	1226.1000	–
GLE 76 (2024/11/21)				
5	0.6792	1.0512	1.0000	–
11	5.3857	8.6884	5.9000	0.9822
15	10.4571	20.3835	10.3000	–
20	16.0790	58.6543	23.7000	–
40	28.5370	2203.9794	526.0000	–
GLE 77 (2025/11/11)				
5	0.8630	1.8414	2.1000	–
11	7.6536	33.1612	22.0000	41.4322
15	16.1887	139.0550	71.1000	–
20	27.9960	686.7011	222.2000	–
40	62.1618	31400.6926	2473.5000	–

dose values compared to NAIRAS, but catches the alerts. Furthermore, Figure 3.7 and the analysis in Appendix A.3.5 show that the maximum value for GLE mode is obtained during the first peak and lower values are reached later remaining over alert levels for 15 and 20 km of altitude, as NAIRAS.

GLE 74 is treated apart due to its particular development, as it took place after a Forbush decrease (see Section 2.2.4). This implies that even if it was detected by Real-Time Alert Gle+ algorithm, it remained invisible for Long Previous Time version, so its duration cannot be captured and the scenario would quickly come back to GCR scenario. Moreover, the proxies for GLE model, which are neutron count rate increases, consider a higher baseline so the model will give barely accurate results. Neither the Statistical Model works, as most of the time the neutron count rate increases are negative. This highlights the limitation of the model for this kind of GLE event.

For all the GLEs, at altitudes of 5 km, the values are very similar between GCR and GLE modes, and compared to NAIRAS model. Those values remain far for the alert thresholds, so this altitude does not supply much information for the tool development, as radiation hazard at 5 km seems to be very unlikely.

Considering all the studied GLEs (except for GLE 74) at altitudes of 40 km, which is over the validity limits of AniMAIRE, the maximum effective dose rate values tend to be higher than NAIRAS, and even very much higher in some cases like GLE 73 and 77. Therefore, this model at 40 km should only be used for a extremely conservative perspective, as it would catch the alerts like NAIRAS, but the values show very poor accuracy. GCR mode do not catch the enhanced radiation values at those altitudes.

Furthermore, AniMAIRE in GLE mode has been compared to the Statistical Models based on CRAC:DOMO to study its agreement with historical GLE data for 11 km of altitude. For GLEs 73 (apart from the huge peak recorded at some point, see Figure A.12), 75 and 76, AniMAIRE seems to slightly overestimate the values with respect to the Stadistical model, while for GLE 77 the Stadistical Model predicts a higher and longer peak (see Figure 3.7). The difference between both models remains around 6-7 $\mu Sv/h$ for the last three GLE, and higher due to the huge peak for GLE 73.

The results and conclusions of this study are summarized as follows:

- Weaker GLEs (GLE 75 and 76) can be assessed for alert detection using AniMAIRE in GCR mode as long as altitudes are lower than 20 km.
- Stronger GLEs (GLE 77) would lose alerts at flight altitudes like 11 km by using AniMAIRE in GCR mode. Unless such a GLE is preceded by a Forbush decrease, it would be detected during its length by GLE Alert+.
- If the GLE is preceded by a Forbush decrease, neutron count rate increases could be negative and therefore, results can lose accuracy in GLE mode.
- Agreement between Statistical Model (that represents GLE historical data assessed

with CRAC:DOMO model) and AniMAIRE for GLE is good. AniMAIRE seems to overestimate the results during weaker GLEs and underestimate them during stronger GLEs with relation to Statistical Model.

- Results of AniMAIRE for GLE can be different according to the set of used stations, being the most accurate when the default combination of Oulu and Dourbes is available. Other ways of computing the particle spectra should be explored in the future.
- Results at 5 km show that the radiation environment does not reach hazardous levels at that altitude. GLE and GCR modes produce similar results.
- Results at 40 km show that AniMAIRE model cannot be properly used.
- For nowcast and alert emission, GLE Alert+ seems to work fine comparing with NAIRAS. Therefore, adding GOES data as a trigger condition is not necessary unless accuracy in dose values is required instead of alert emissions.

3.2. Results

In this Section, results of effective dose maps for different dates and regions are displayed, showing the output of the tool. The configuration of the tool to obtain these results employs the parameters and decisions reached in Section 3.1.

Firstly, a global map of effective dose rates for GCR scenario at 11 km corresponding to 2025/12/12 at 12:00:00 UTC is shown in Figure 3.8. For the same day, a map for a specified region that mostly consists of Europe, at 20 km altitude, is shown in Figure 3.9. The chosen resolution for latitude and longitude, being both of them inputs to the tool, is 5° for both. The maps include contour lines indicating some values of effective dose rates.

In both maps, the D-Index is indicated to be zero, as GCR scenario does not involve solar contribution, which shapes that index, and another message states that no alert levels have been reached, referring to FAA alert level of $20\mu Sv/h$, or ICAO alert levels of $30\mu Sv/h$ and $80\mu Sv/h$.

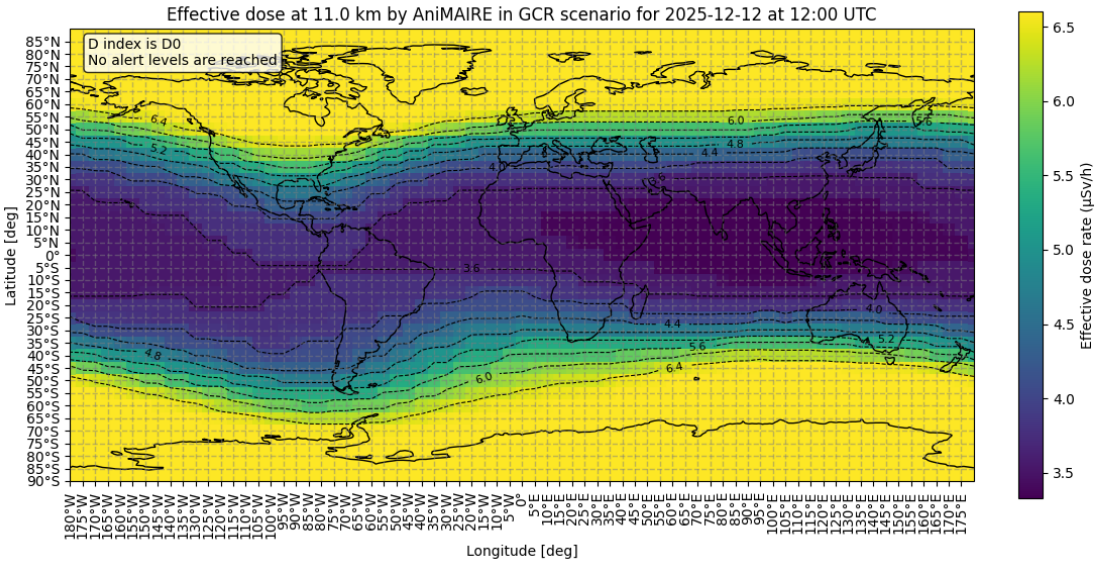

Figure 3.8: Effective dose rate map for GCR at 11 km on 2025/12/12

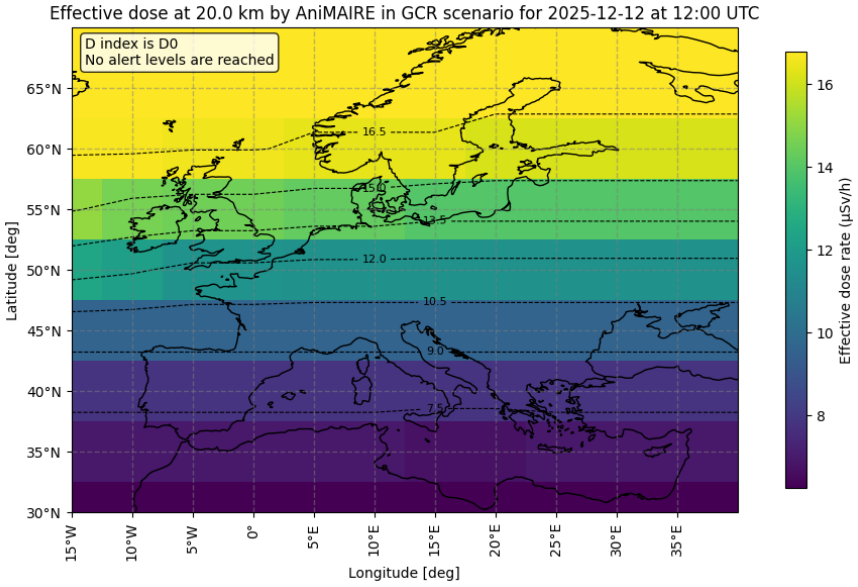

Figure 3.9: Effective dose rate map for GCR at 20 km on 2025/12/12

In Figures 3.10 and 3.11, global maps for effective dose rates and D-Index are shown during the beginning of GLE 77 (2025/11/11) at 20 km of altitude. In this case, the dose rates achieve much higher levels and therefore the messages warn of the alert levels reached and display the maximum value of D-Index. Similarly, contour lines indicating the alert level values are emphasized.

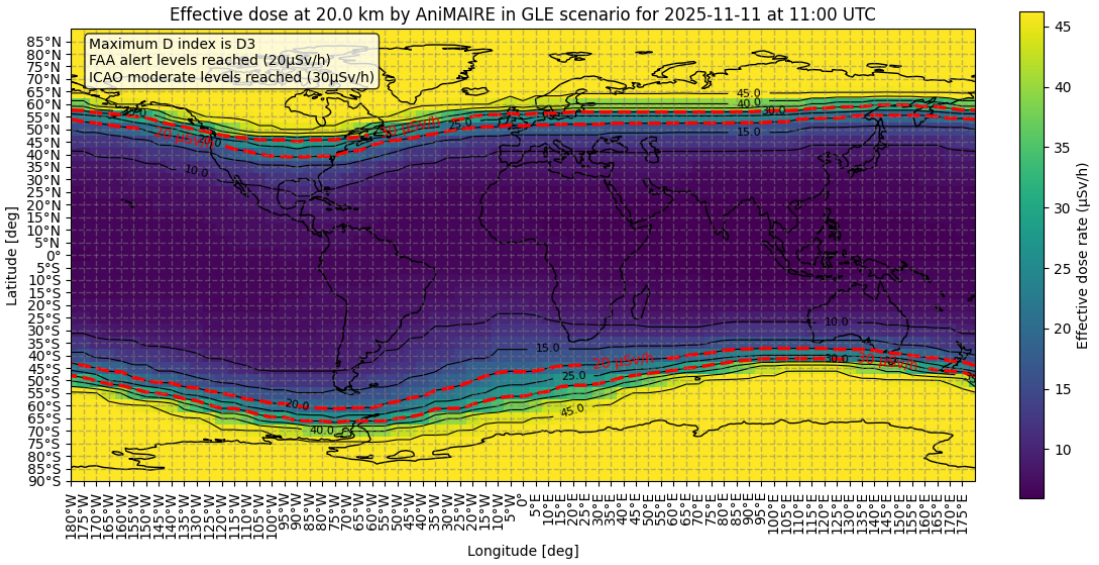

Figure 3.10: Effective dose rate map during GLE 77 (2025/11/11) at 20 km

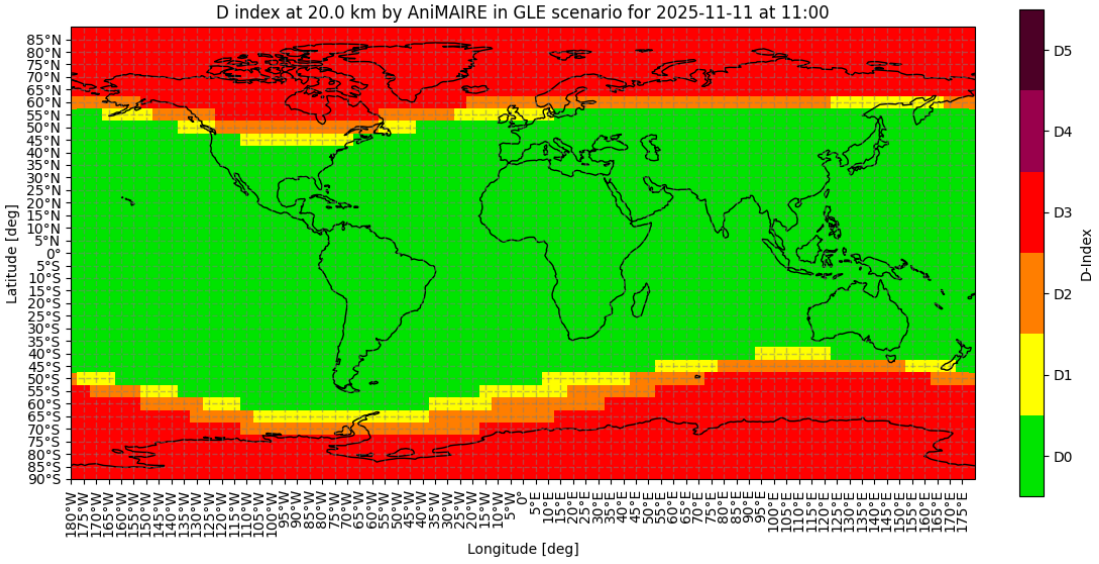

Figure 3.11: D-Index map during GLE 77 (2025/11/11) at 20 km

3.3. Conclusions

Integrating several logics and models related to atmospheric radiation dose assessment, the developed tool can be used to compute effective dose rates at the desired regions and altitudes, both to detect radiation level enhancements that can pose a hazard to human health and to analyze the radiation exposure after a flight.

The validity limits are defined by the conclusions reached during the preliminary studies:

- Implementation of the GLE Alert+ algorithm only works for stronger GLEs and can lose information when there is previous intense activity. Even if the results for effective dose rates are reasonable without detecting the GLE for weaker cases, if a more conservative approach is desired, GOES proton flux can be added as a secondary proxy for GLE detection and aggressivity of GLE Alert+ algorithm increased by reducing the threshold.
- When a Forbush decrease takes place before a GLE, the algorithm fails to capture the duration of the GLE, and inputs for the model lead to underestimated dose rates values, specially at higher altitudes. Nevertheless, the physical meaning of the Forbush decrease implies that GCR impacts are highly decreased by the CME modulation and therefore the radiation induced by solar particles is not added to the GCR environment, but acts on its own. Therefore, it should be studied if the dose rates produced by a GLE after a Forbush decrease are hazardous or the radiation environment remains low due to the absence of GCR.
- When GLE detection fails for weaker events, the GCR model will produce acceptable results up to 20 km, being more accurate at lower altitudes.
- Validity limits of AniMAIRE for GCR are up to around 30 km of altitude, while for GLE validity is expected up to 20 km of altitude. It can be reduced if the event is not detected, but it is still valid at typical flight levels like 11 km.
- The model for effective dose computation is totally dependent on Oulu neutron count rate, as it is used to define the particle spectra both for GCR and GLE. Therefore, the whole effective dose rate computation part of the tool is dependent on this data, which can lead to unavailability in case of lack of Oulu data.
- By definition, D-Index only depends on solar contribution to effective dose, which implies that no value is given when GCR scenario is on going, only during a GLE event. Nevertheless, alert levels of effective radiation dose are still assessed by ICAO and FAA thresholds in GCR scenario.
- As MAIRE+ logic is used for particle spectra computation for GLE, isotropy is assumed, which is not at all accurate for the initial part of a GLE. Therefore, doses might be overestimated during part of the GLE, which leads to a conservative approach. Nevertheless, it is important to notice that real-time determination of the anisotropy of the GLE requires a complex implementation like in WASAVIES model.

Therefore, future improvements that can be included in the tool might be:

- As D-Index is only defined for solar contribution to effective dose, during non-detected GLE or increased solar activity without a GLE, it won't be available. Therefore, an adaptation of D-Index to assess all contributions to effective dose shall be developed.
- Including a logic to detect whether Forbush decreases are taking place before a GLE. This could be easily implemented by comparing neutron count rates before the increase of the GLE with the previous ones.
- Machine Learning developments could be interesting to improve the performance of GLE detection, assessing Forbush decreases, high solar activity periods and detecting patterns that are not perceived by simple algorithms. Other details such as geomagnetic indices or characteristic of the current solar cycles could be implemented this way into the detection logic.
- Particle spectra are computed by using AniMAIRE functions that use neutron count rates at Oulu and another station as proxies. AniMAIRE also offers functions to manually introduce the particle spectra for computations. Another approach would be to estimate the full spectra of particles from all the neutron count data and/or GOES data. This is done in WASAVIES and NAIRAS according to [58] and [41] by fitting real-time data to pre-calculated databases or analytical functions. Therefore, an estimation of the spectra of particles from experimental data could be included to improve accuracy. Furthermore, anisotropy of the GLE could also be estimated from that data with procedures like the ones used by WASAVIES in [58].

4 | Internal and surface charging in geostationary orbit

As introduced in Section 2.4, high energy electrons penetrating into the satellite can pose a risk in GEO orbit, causing internal charging with diverse failures as consequences. Meanwhile, surface charging risk is driven by the presence of low energy electrons and also entails diverse potential failures.

In the present chapter, a number of instruments on board different missions studying particle populations in GEO will be explained (Section 4.1) and their electron flux data will be processed and compared (Sections 4.2 and 4.3). The objective is to know whether data from the different satellites can be used for risk assessment of internal and surface charging in GEO, as well as to understand the variation of particle populations along the orbit and therefore the dependence of risk with GEO position.

The conclusions of the mentioned studies will be used to develop a tool for charging risk assessment in GEO in Section 4.4, designed to assess internal charging risk in real time and both internal and surface charging risk for post-mission analysis.

4.1. Particle flux monitoring in GEO and data availability

First, the considered instruments for particle flux monitoring in GEO missions will be explained, as well as their data availability and applicability.

4.1.1. Instruments for particle detection in GEO

The instruments that have been considered to retrieve integral electron fluxes in GEO, measured in particle flux units, pfu (particles $cm^{-2}s^{-1}sr^{-1}$), as well as differential electron fluxes, measured in particles $cm^{-2}s^{-1}sr^{-1}keV^{-1}$, are the following ones:

- **SEISS/MPS in GOES-R series (GOES 16, 17, 18, 19)**: The Magneto-

spheric Particle Sensor (MPS), which is part of the Space Environment In-Situ Suite (SEISS), monitors electrons and protons through fluxmeters [70]. The segment of the instrument dedicated to high energy particles is called MPS-HI and covers directional fluxes, particularly differential electron fluxes between 50 and 4000 keV in 10 different channels, plus integral electron flux of more than 2 MeV. It covers as well differential proton fluxes between 80 keV and 12 MeV in 11 channels [51]. On the other hand, MPS-LO monitors low energy protons and electrons, from 0.03 to 30 keV. MPS-HI data is provided both in one minute and five minutes averages and consists on Level 2 data, that is, fully validated data and ready to use. Meanwhile, MPS-LO data is only provided as provisional validated data with a one second cadence [50]. NOAA warns that the >2 MeV channel might be contaminated by very high energetic protons during solar proton events [53].

- **Next Generation Radiation Monitor (NGRM)**: NGRM is part of ESA's Distributed Space Weather Sensor System (D3S) and flies on board of four different satellites at the time of writing: European Data Relay System - C (EDRS-C), Meteosat Third Generation-Imager (MTG-I1) and Meteosat Third Generation-Sounder (MTG-S1) in GEO orbit, and Sentinel-6 Michael Freilich (S6-MF) in LEO. It integrates electron detectors and stacked detectors and the measurements are processed to provide omnidirectional differential and integral fluxes. Only the NGRM on board the EDRS-C spacecraft measures integral electron flux of more than 2 MeV, while differential electron flux channels cover from 180 keV to 4 MeV and differential proton flux from around 5 to 90 MeV [18]. Level 1 data of EDRS-C/NGRM is provided with a 1 minute cadence and shows good agreement with third party measurements, but can overestimate electron fluxes of higher energy (from 2-2.5 MeV) by a factor that can reach a factor of 2 or 3, and contamination is expected during solar particle events [15].

- **ICARE-NG² (Influence sur les composants avancés des radiations de l'environnement)**: It is also part of ESA's D3S and the third generation of the CNES-ONERA-EREMS (Centre National d'Études Spatiales - Office National d'Études et de Recherches Aérospatiales - Environnement Radiatif de l'Espace Multi-Satellites) radiation monitors, flying on board of the Hotbird-13F and Hotbird-13G GEO satellites. It includes three sensors composed by silicon detectors that provide omnidirectional fluxes, particularly integral electron fluxes from >0.65 to >2 MeV, as well as differential proton fluxes from 15 to 98 MeV in six channels [17]. The level 1 data is provided with a 1 minute cadence and is in line with EDRS-C/NGRM and may suffer statistical issues for high energy levels. Electron channels

may also suffer proton contamination during solar particle events [8].

ESA data (particularly EDRS-C/NGRM and ICARE-NG² will be used) can be retrieved using HAPI (Heliophysics API) which is a community standard API designed for Space Weather and solar physics data downloading. It allows programmatic access to data through requests and requires the credentials of a registered ESA Space Weather account [57].

The mentioned instruments are collected in Table 4.1, including the host satellite, the mission launch date, the GEO position and the measured flux type, directional or omni-directional. It shall be noticed that GOES 16 and 17 remain as back-up satellites since the introduction of GOES 18 and 19, and their particle flux data is only available until April 2025 and end of 2022 respectively. Currently, GOES 18 is appointed by NOAA as the primary source for protons fluxes, while GOES 19 is the primary source for electron fluxes.

Table 4.1: Overview of particle flux monitors on GEO satellites.

Satellite	Instrument	Launch date	Longitude (GEO)	Flux Type
NOAA / NASA (GOES-R Series)				
GOES-16	SEISS/MPS-HI	Nov 2016	75.2°W	Directional
GOES-17	SEISS/MPS-HI	Mar 2018	104.7°W	Directional
GOES-18	SEISS/MPS-HI	Mar 2022	137°W	Directional
GOES-19	SEISS/MPS-HI	Jun 2024	75°W	Directional
ESA Distributed Space Weather Sensor System				
EDRS-C	NGRM	Aug 2019	142.5°E (31°E until May 2025)	Omnidirectional
Hotbird-13F	ICARE-NG²	Oct 2022	13°E	Omnidirectional
Hotbird-13G	ICARE-NG²	Nov 2022	13°E	Omnidirectional

4.1.2. Data applicability for operational service

The applicability of the electron fluxes data, in terms of nowcasting and posterior analysis for operational services, is summarized in what follows.

NOAA offers near-real time data (with 5-10 minutes of delay) in .json format [1] from the

[1] https://services.swpc.noaa.gov/json/goes/

7 previous days. The last data point corresponds to few minutes before the current time instant. This way, the >2 MeV integral electron flux [pfu = particles cm^{-2} s^{-1} sr^{-1}] in 5 minute averages and the differential electron fluxes [particles cm^{-2} s^{-1} sr^{-1} keV^{-1}] in 5 minute averages in 10 different values of energy (79 keV, 134 keV, 186 keV, 271 keV, 378 keV, 548 keV, 865 keV, 1509 keV, 2205 keV, 2894 keV) are available.

Meanwhile, data from ESA's D3S is reachable by HAPI with a less than 5 minutes delay and for any period of existing data. The data explained for NGRM and ICARE-NG[2] are then available, including >2 MeV integral electron fluxes from EDRS-C and differential electron fluxes from 180 keV to 4 MeV.

Nowcast can therefore be supplied for internal charging risk assessment in GEO as near real time data of >2 MeV integral electron flux is available from many instruments.

On the other hand, in terms of historical data, it is retrievable with 1 day of delay for GOES in .nc files[2] and includes all the high and low energy electron fluxes data from SEISS/MPS-HI and SEISS/MPS-LO instruments, respectively. Therefore, low energy electrons between 10 and 50 keV can be retrieved and surface charging can be analyzed a posteriori from GOES data, while none of the ESA instruments offer such low energies. Similarly, the posterior analysis can also be applied for internal charging from the >2 MeV electron fluxes. This analysis is useful in case an anomaly is detected in a GEO satellite and the plasma environment has to be studied to understand whether the anomaly is related to internal or surface charging.

4.2. Data analysis for internal charging

As described in Section 2.4, internal charging in GEO satellites is produced by the accumulation of high energy electrons (more than 2 MeV) and risk criteria can be defined in terms of instantaneous flux and fluence. Therefore, data from the different instruments can be compared to consider if they can be equally used for internal charging risk assessment.

For this scope, integral electron flux data of more than 2 MeV from all the instruments will be downloaded, processed, represented and statistically compared for different periods of time, including quiet time (no solar activity) and intense solar activity.

The reference data is the one from GOES 19, as it is the primary source of electron fluxes for NOAA and all the risk level thresholds are defined from GOES data. It is provided with a 5 minutes average, so to compare a similar structured data from ESA's

[2] https://data.ngdc.noaa.gov/platforms/solar-space-observing-satellites/goes/

D3S instruments, the fluxes from the latter will be also averaged every 5 minutes (it is originally provided with a 1 minute cadence). The minimum value for electron flux is set to 4 pfu according to NOAA's representations (see [53]).

Figure 4.1 shows the integral electron fluxes (>2 MeV) from GOES 19 and 18/SEISS/MPS-HI, EDRS-C/NGRM, Hotbird (HB) 13F and 13G/ICARE NG[2] instruments during the first five days of January 2026. The SWPC threshold for electron flux alerts is also represented (see Section 2.4 and particularly Table 2.3) as a dashed red line at a flux value of 1000 pfu. The fluxes are represented over Local Solar Time rather than UTC to better compare the daily variations of fluxes. As it is immediate to see, the flux maxima happens at around local noon for all the instruments, while flux minima takes place around local midnight. This period was quiet in terms of S Scale (solar radiation storms) and almost all of it was also quiet in G scale, only showing minor geomagnetic activity (Kp=5) from 2026/1/2 at 18:00 to 2026/1/3 at 00:00UTC. No strong activity took place therefore, so it can be considered a quiet time period. GOES and Hotbird instruments measure fluxes over the SWPC alert threshold of 1000 pfu around every local noon, while EDRS-C remains at lower values during the first two days.

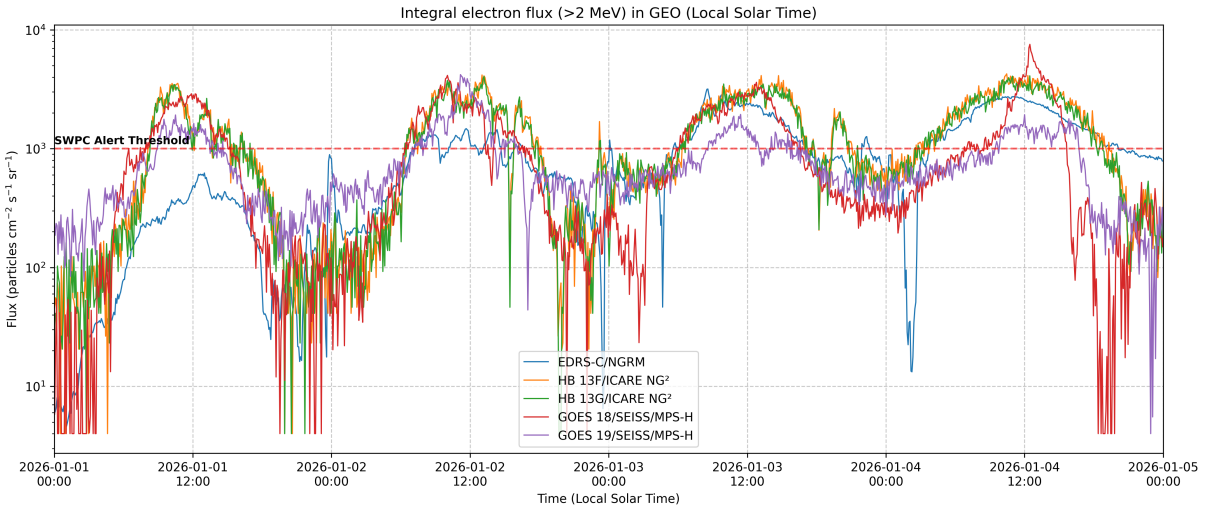

Figure 4.1: Integral electron flux (>2 MeV) in GEO (Local Solar Time) during 1 to 6 January 2026.

Meanwhile, Figure 4.2 shows the high energy electron fluxes from the 9th to the 19th of November 2025, including the most intense geomagnetic and solar radiation storms registered that year during days 12 and 13[3]. For this case, fluxes are represented in UTC as

[3]It can be consulted in https://www.spaceweatherlive.com/en/solar-activity/top-solar-radiation-storms/solar-cycle/25.html and https://www.spaceweatherlive.com/en/auroral-activity/top-50-geomagnetic-storms/year/2025.html

it allows to see the increase in electron fluxes produced by the increase in very energetic protons at the 11$^{\text{th}}$ of November at around 10:30 UTC (that corresponds with the proton flux increase seen in Figure 3.5). From the technical information of the instruments, that warn of contamination in high energy electron channels due to very energetic protons, these increases shall be attributed to such contamination rather than an increase in electron population.

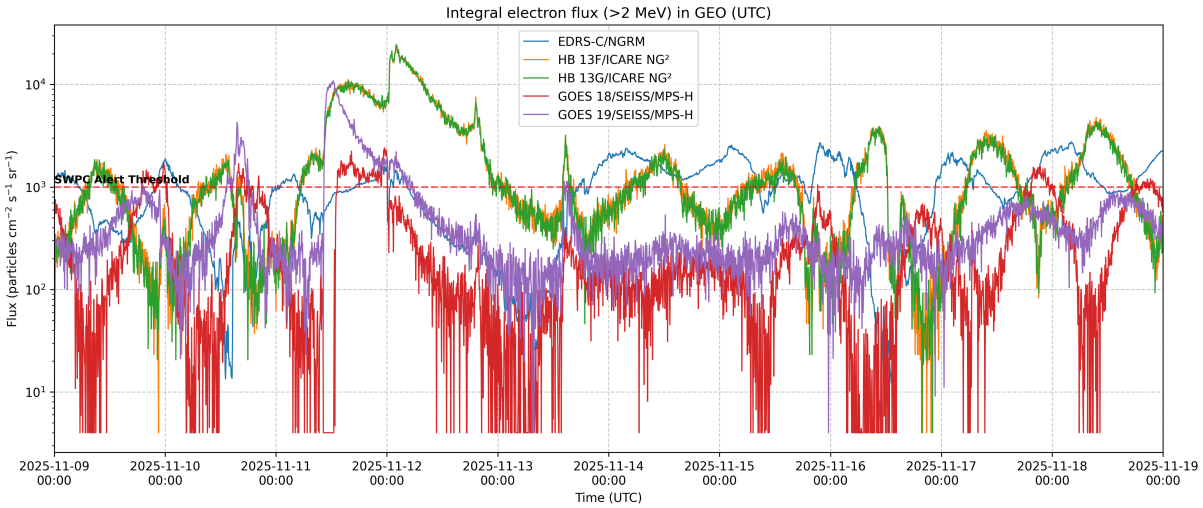

Figure 4.2: Integral electron flux (>2 MeV) in GEO (Local Solar Time) during 9 to 19 November 2025.

To quantify the consistency between the electron flux measurements by the different instruments, the Pearson and Spearman correlation coefficients ([68]) can be computed to assess the strength of the linear relationship between the data and the similarity in temporal evolution, respectively.

The Pearson correlation coefficient, r, quantifies the strength of the linear relationship between two time series of electron flux measurements, x_i and y_i, obtained from different instruments. It is defined as

$$r = \frac{\sum_{i=1}^{N}(x_i - \bar{x})(y_i - \bar{y})}{\sqrt{\sum_{i=1}^{N}(x_i - \bar{x})^2}\sqrt{\sum_{i=1}^{N}(y_i - \bar{y})^2}}, \tag{4.1}$$

where $\bar{x}$ and $\bar{y}$ are the mean values of the respective datasets and N is the number of common observations. The coefficient ranges from -1 to 1, with values close to 1 indicating a strong positive linear correlation, values close to -1 indicating a strong negative linear correlation, and values near zero indicating weak or no linear relationship.

The Spearman rank correlation coefficient, ρ, is used to evaluate the similarity in the temporal evolution of the electron flux measurements independently of their absolute values. To compute this coefficient, each dataset is first transformed into a ranked series, $R(x_i)$ and $R(y_i)$, by replacing the original values with their corresponding ranks after sorting the data in ascending order, with tied values assigned the average of the corresponding ranks. The coefficient is then obtained by applying the Pearson correlation formula to the ranked variables and can be equivalently expressed as

$$\rho = 1 - \frac{6 \sum_{i=1}^{N} d_i^2}{N(N^2 - 1)}, \tag{4.2}$$

where $d_i = R(x_i) - R(y_i)$ represents the difference between the ranks of the paired observations. The coefficient varies between -1 and 1, with larger absolute values indicating stronger monotonic agreement in the temporal behavior of the measurements.

The correlation coefficient values are depicted in Table 4.2 for the period from September to December 2025 (both included), which experienced both quiet and more active periods, during the decay of the Solar maxima of the 25$^{\text{th}}$ Solar Cycle. The table represents a matrix with the correlation coefficients between every pair of instruments, with the Pearson coefficient values in the upper right part, over the main diagonal, and the Spearman coefficient values in the lower left triangle, under the diagonal. The results show high correlation values, greater than 0.7 in all the cases, implying a strong agreement in linear correlation and temporal evolution for the data measured by all the instruments.

Table 4.2: Combined Correlation Matrix for Electron Flux Measurements. Upper Triangle: Pearson Coefficient (Linear Magnitude). Lower Triangle: Spearman Coefficient (Monotonic Trend).

Instrument	**EDRS-C** (NGRM)	**Hotbird 13F** (ICARE NG^2)	**Hotbird 13G** (ICARE NG^2)	**GOES 18** (MPS-H)	**GOES 19** (MPS-H)
EDRS-C	**1**	0.805	0.806	0.724	0.737
Hotbird 13F	0.842	**1**	0.995	0.846	0.763
Hotbird 13G	0.843	0.982	**1**	0.843	0.760
GOES 18	0.743	0.835	0.832	**1**	0.815
GOES 19	0.755	0.815	0.815	0.849	**1**

Both Hotbird satellites obtain almost the same values when compared to each other, with

the highest correlation coefficients (0.995 for Pearson and 0.982 for Spearman), which is due to the same position in 13°E and the similar instrument carried. The GOES satellites correlate to each other better than with the other satellites and EDRS-C correlates better with the Hotbirds than with GOES. The fact that different instruments do not measure the exact same values is due to their physical differences, calibration, processing algorithms, noise, localized variations in the plasma environment, etc, apart from the flux definition itself, that is directional for GOES and omnidirectional for the ESA satellites.

Furthermore, the high energy electron fluence (expressed in particles cm^{-2} s^{-1} sr^{-1}), which is the flux integrated over time, can be computed from the flux values. The latter are expressed in 5 minutes averages, so they can be integrated by multiplying the flux values by the 5 minutes periods and summing along the integration time. This way, doing this every day, the 1-day fluence can be computed. The fluence also possesses risk indicators as explained in Section 2.4 and collected in Table 2.3, so it is useful to monitor internal charging risk in GEO. Internal charging typically needs more than 30 hours of charging, so the high risk indicator would be a warning to monitor the satellite for the next day, as internal charging can be expected.

Figure 4.3 shows the 1-day fluence along four months (September to December 2025) for the different instruments, with a grid spacing in x axis corresponding to 1 day, expressed in Local Solar Time. It also shows the two thresholds for medium and high risk alert level for 1-day fluence, which respectively are 5×10^7 and 5×10^8 particles cm^{-2} sr^{-1} (see Table 2.3). Similarly to the flux plots, the temporal variation is the same for all instruments, but differences are more noticeable in terms of the daily values of fluence. The Hotbird instruments show almost similar values and are close to EDRS-C, whose values are lower. Meanwhile, GOES 19, which is the primary satellite for electron fluxes as appointed by NOAA, measures lower peak values and unchains less alert levels than the ESA satellites. It has to be noticed the effect of the strong solar activity during the 12-13 November 2025, that, as seen for the fluxes, affected the measurements presumably due to contamination by very energetic protons.

One of the objectives of this study is to identify whether the instruments can be interchangeable according to the fluence measurements for risk assessment. Therefore, by looking at the moments where fluxes cross the risk thresholds it can be seen that Hotbirds and EDRS-C enter medium risk levels during the same days, while Hotbirds stay longer at high risk levels. Those high risk levels are not always reached by GOES 19. As the risk indicators are designed for GOES data satellites and GOES 19 is assigned by NOAA as the primary satellite for electron fluxes, it can be concluded that using the other satellite data can lead to overestimated fluence values.

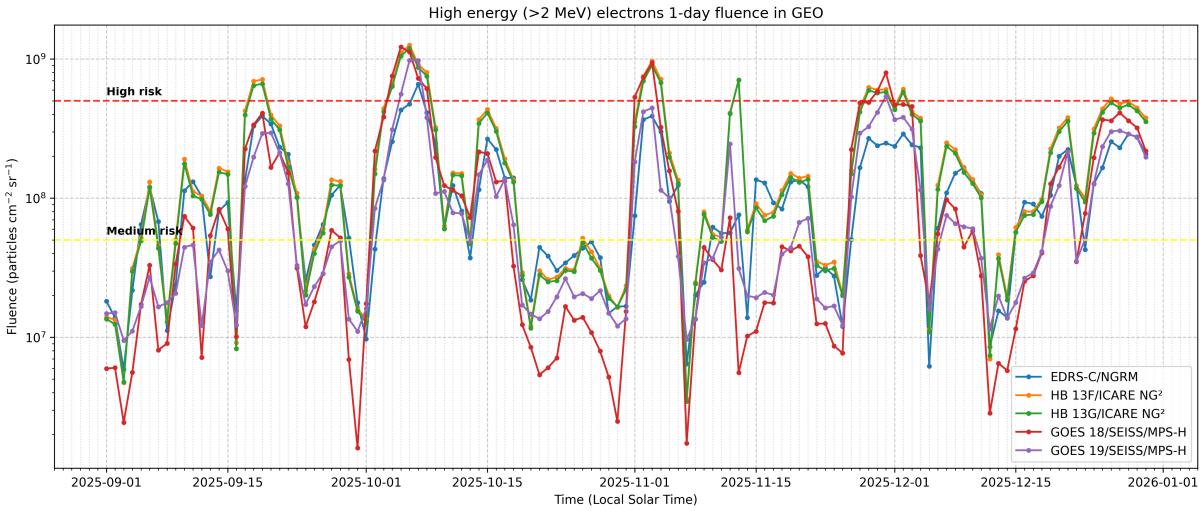

Figure 4.3: Electron fluence (>2 MeV) in GEO (Local Solar Time) during September to December 2025.

The results allow to form a picture of the plasma environment concerning high energy electrons (>2 MeV) in GEO. All the instruments show a similar evolution in Local Solar Time, with daily considerable variations of around one order of magnitude in flux intensity, which evinces that the energetic electron population in GEO is not uniform and depends strongly on the longitude and therefore on the Local Solar Time.

Therefore, directly using the GOES flux data to monitor high energy electron fluxes and the associated internal charging risk is not accurate for satellites that are distant from GOES in the GEO region and data should be particularized to the Local Solar Time.

Some instruments are available to retrieve >2 MeV fluxes (EDRS-C / NGRM, Hotbird 13F and 13G / ICARE NG^2, GOES-R / MPS-HI) and they experiment similar time evolution but with some differences in magnitude. The GOES 19 data is considered as reference data as it is NOAA's appointed spacecraft as primary for electron fluxes and the risk thresholds used are based in GOES data. The other instruments show good consistency but overestimate the fluxes in many cases, specially in terms of risk assessment, so their use would need the implementation of scaling factors to enhance accuracy. The fact that the time evolution is the same for the same day at all the instruments allows to use the data from one of the instruments and estimate the flux values at distant GEO satellites from identifying the fluxes with their Local Solar Time. The assumption of little changes along the same day in electron fluxes is therefore supported by this study.

Furthermore, it is to be noticed that the used thresholds for internal charging risk are based in GOES data (from older GOES satellites) and may overestimate the flux val-

ues considering that new instruments may have a higher sensitivity. An update of the thresholds could be done by studying anomaly databases and current GOES data.

4.3. Data analysis for surface charging

Surface charging in GEO satellites is due to low energy electron in the order of tens of keV, as seen in Section 2.4 and risk criteria have been defined based on 10 to 50 keV (see Table 2.4). Only GOES satellites offer data of such low energy electron fluxes from the instrument SEISS/MPS-LO in 15 differential channels from 0.03 keV to 30 keV and 14 angular views (12 of them are independent, while there are two redundant angular views) [52].

According to literature, as seen in Section 2.4, low energy electron fluxes are expected to increase with geomagnetic activity in the nightside of Earth, due to particle injection in the magnetotail. Therefore, quiet and active periods in geomagnetic activity will be analyzed.

The GOES 19 data is used for the study as it is the primary source of electron fluxes for NOAA. As explained in Section 2.4, the expected range of electron energies related to surface charging is from 10 to 50 keV, so the closest data provided by GOES instruments consists on the 11.3 keV, 18.2 keV and 30 keV differential channels from MPS-LO and the 50-80 keV channel from MPS-HI.

Those four channels are expressed in particles cm^{-2} s^{-1} sr^{-1} keV^{-1}, so in order to retrieve the integral fluxes from the available data, the 11.3, 18.2 and 30 keV channels will be integrated to compute the integral flux from 10 to 30 keV, while the 50-80 keV channel will also be integrated to compute the integral flux from 50 to 80 keV.

The comparison of those two different integral fluxes is interesting in order to understand their behavior and decide how to use them for surface charging assessment. While the lower energy data is only available with 1 day of delay, the 80 keV channel is offered in near real time, so it is the only one that could be used for surface charging risk nowcast.

The integration to obtain the integral flux for 10-30 keV is done by assuming effective energy widths computed using the geometric mean (i.e. the midpoint in logarithmic space) between adjacent channel centers. This way, the first energy window centered logarithmically around 11.3 starts in 10, which is the lower bound of the energy interval and finishes in $\sqrt{11.3 \cdot 18.2} = 14.34$ keV; the second one starts in 14.34 and finishes in $\sqrt{18.2 \cdot 30.0} = 23.37$ and the last one starts in 23.37 and finishes in 30.0. Therefore, the integral flux is retrieved from the sum of the product of the differential flux in each

channel and the assumed effective width of each channel:

$$\phi_{10-30\text{ keV}} = F_{11.3\text{ keV}} \cdot 4.34 + F_{18.2\text{ keV}} \cdot 9.03 + F_{30\text{ keV}} \cdot 6.61 \tag{4.3}$$

Where the integral flux in pfu is denoted by ϕ and the differential flux in pfu keV^{-1} is denoted by F. This assumption is done to model the integral flux and is based on the logarithmic distribution of the energy channels of the instrument (30.0 keV, 18.2 keV, 11.3 keV, 6.588 keV, 4.94 keV, etc [52]). It implies that the electron flux measured for each channel of energy is expected to be similar for the surrounding energies respecting the mentioned logarithmic distribution.

On the other hand, as directly indicated in the technical information of the SEISS/MPS-HI instrument, the width of the channel 50-80 is 30 keV [51] and therefore the integration is directly done by multiplying the differential flux and such width.

This integration is done for each of the independent views of the instrument and then all of them are summed to provide the total integral flux as seen from the GOES satellite. Normally, one of the views measures fluxes around one order of magnitude higher than the rest (the figures with differential electron fluxes and a short analysis about them is located in Appendix A.5). It is also to notice that data from SEISS/MPS-LO is level 1b and therefore has some caveats, like negative flux values due to noise subtraction and gaps of data [52].

The low energy fluxes are represented in Figure 4.4 during the first days of January 2026, which was a mostly quiet period in terms of geomagnetic storms. The represented thresholds show significant and high superficial electrostatic discharge (ESD) risk from 10-50 keV electron flux as introduced from [36] in Section 2.4. It can be seen that the peak fluxes of 10-30 keV take place from midnight to 6 AM approximately for every day, which coincides with the expected behavior of the low energy electron population. The flux enhanced in the local midnight region corresponds to the magnetotail, due to particle injection. Meanwhile, the 50-80 keV flux experiences two higher peaks during those periods and a less localized evolution the rest of the time. Almost all of the peaks of 10-30 keV flux show a significant risk of ESD. As noticed in the mentioned analysis in Appendix A.5, it can be seen that there is missing data from many angular views on 4 January which leads to apparent low flux.

Figure 4.5 also represents the low energy fluxes over Local Solar Time but corresponding to the period from 9 November 2025 to 16 November 2025. This period is chosen as a strong solar storm took place during 12 and 13 November 2025 (see Appendix A.6). The

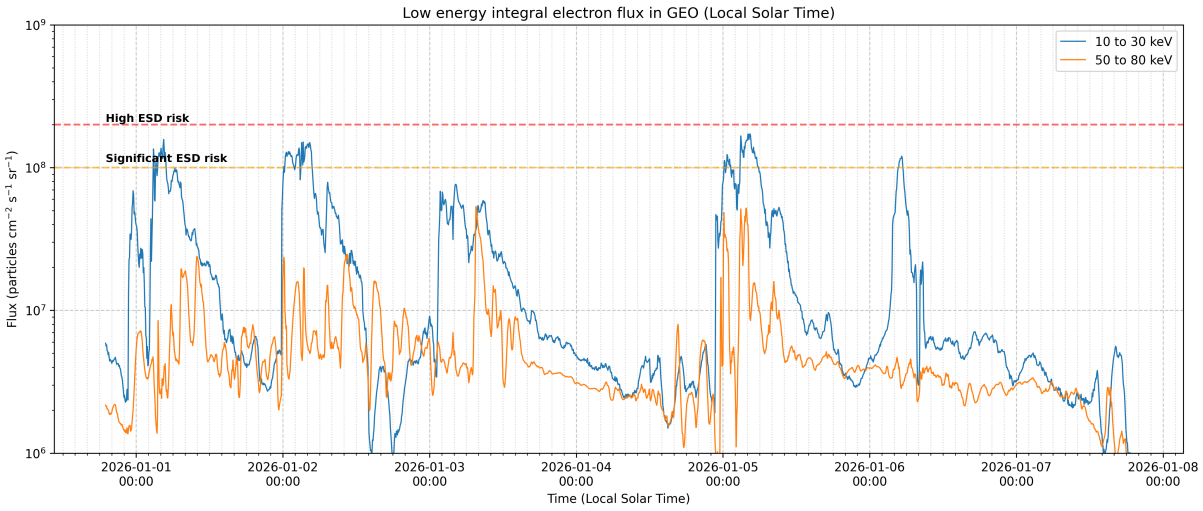

Figure 4.4: Low energy integral electron flux in GEO (Local Solar Time) from 1 to 6 January 2026.

peak fluxes of 10-30 keV flux during the storm reach high risk values and are wider than the other peaks, implying longer risk periods. It can also be seen that the 50-80 keV shows a great enhancement during the storm, reaching as well ESD risk levels, while the other peaks of that flux remain much lower, as it happened in Figure 4.4. Notice that data is missing during 14 November (see Appendix A.5), as can be seen reflected in the low values of 10-30 keV flux.

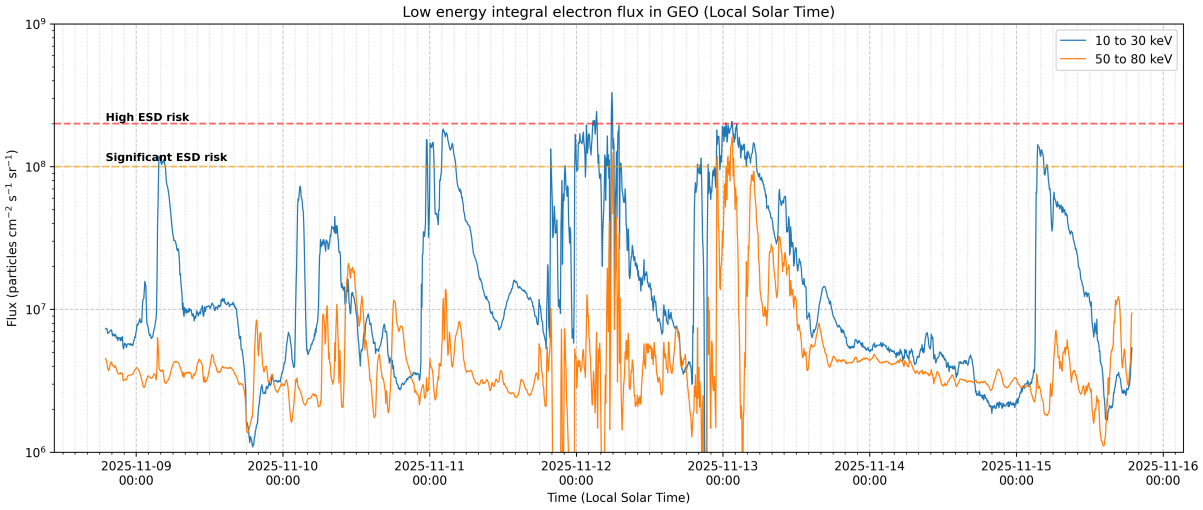

Figure 4.5: Low energy integral electron flux in GEO (Local Solar Time) from 9 to 19 November 2025.

From the analyzed periods of data, it can be concluded that 10-30 keV flux shows a clear evolution in time according to Local Solar Time, peaking from midnight to 6 AM and

increasing its value during high geomagnetic activity. Surface risk charging, associated to such low energy electron fluxes will be therefore higher during the local night time.

Meanwhile, the 50-80 keV flux shows a softer dependence on local time, but still with peaks during local night time, and experiments a much higher relative increase due to geomagnetic activity.

The risk thresholds are designed for 10-50 keV flux, which is not totally measured by GOES or any of the other studied instruments, and seem to be too conservative when applied to 10-30 keV fluxes, as they are continuously reached even during quiet time. More detailed studies concerning real detected anomalies would be needed to enhance the threshold accuracy. Those thresholds should be also adapted to available data, designing both 10-30 keV and 50-80 keV electron flux risk assessment values. The latter seem to be specially useful during geomagnetic storms due to its big increase.

4.4. Method

From the GEO electron flux data analysis carried out through the previous studies, it was concluded that the distribution of both high and low energy electron flux follows a very localized pattern and therefore is extremely dependent on the satellite position in GEO. The different instruments located in GEO show a good agreement in time evolution but some differences in magnitude. A tool for charging risk assessment in GEO orbit can be then developed to provide such information using data from one of the instruments and particularizing it for the whole GEO ring.

The tool is designed to operate in two different modes: real time operation and long term analysis. Real time operation aims at plotting over the world map the instantaneous risk of internal charging based on flux and fluence criteria. Meanwhile, the long term analysis mode is planed to study the internal and surface charging risks during a provided period of time, which can help to characterize experienced anomalies in GEO satellites.

The data from both cases come from the GOES 19 satellite, as it is the primary GOES satellite for electron fluxes as assigned by NOAA. It provides high electron flux data in near-real time (with around 5-10 minutes of delay) in .json format and also .nc data uploaded with one day of delay and containing all the information from the SEISS/MPS-HI instrument about high and low energy electron fluxes (see Section 4.1.2). This data availability implies that only internal charging, related to high energy electrons, can be assessed in real time, while surface charging, mostly due to low energy electrons, is only possible to study afterwards.

The main assumption of the tool is that the electron distribution in GEO does not change much along one day, so knowing the flux measured by GOES 19 at a specific local time allows to estimate that another satellite in a different longitude would experiment the same flux at the same local time for the same day. This assumption is supported by the previous studies.

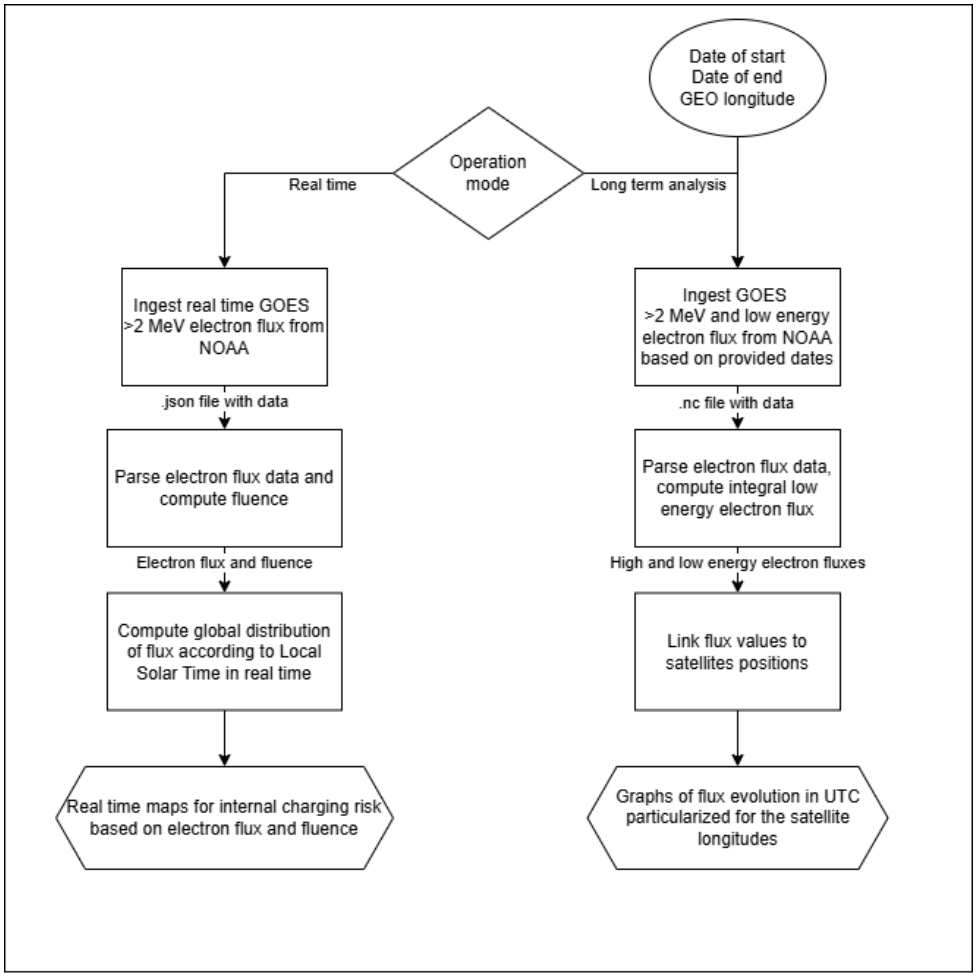

Figure 4.6: Scheme of the GEO charging risk tool.

The real time operation mode (only available for internal charging risk calculations) implements the following steps (see the tool scheme in Figure 4.6):

- Download of near-real time GOES 19 data (>2 MeV electron flux).
- Parsing of the electron fluxes and computation of the electron fluence (flux integrated over time) for the last 24 hours.
- Averaging of flux and fluence for every local hour and computation of the longitudes associated to every local hour for the last day. Computation of the risk indicators

associated to the averaged flux values.

- Plot at the current time of the fluxes and fluences along the GEO ring for the last day, with the associated risk indicators for internal charging. These plots have a validity of around one hour, due to Earth's and GEO satellite rotation, that makes the electron population apparently move to the West, due to their dependence with Local Solar Time.

Therefore, this real time operational mode is designed to monitor the risk status associated to internal charging at any GEO longitude. The output are the described maps and shall be computed at least every hour to update the GEO positions in relation to the electron populations. As the data comes from GOES 19, any satellite located closer to it by the West side will receive more accurate information as GOES measurements would be more recent.

On the other hand, the long term analysis mode requires a desired period under study as well as the target satellite(s) longitude(s) as inputs, and it works as follows:

- Download of several days of GOES data from the SEISS/MPS-HI and SEISS/MPS-LO instruments according to the input period.
- Parsing of the electron flux data (>2 MeV integral flux and low energy differential fluxes). Computation of the fluence for high energy electrons.
- Computation of the integral electron flux between 10 and 30 keV from the differential fluxes.
- Relate the fluxes to the longitudes of the target satellites.
- The outputs are graphs of electron flux along time (expressed in UTC format) for high energy flux and fluence, and low energy flux, including the risk thresholds.

From the output graphs, it is possible to identify the time periods at which a given satellite experienced charging risks. In case an anomalous behavior has been noticed, it can be easily linked to surface or internal charging if the flux levels were high at that time.

It is to be noticed that the downloaded data for low energy electrons (from the SEISS/MPS-LO instrument on GOES 19) consist on heavier files (around 200 MB) than the ones for high energy electron fluxes (around 800 kB). Therefore, the calculation time for this operational mode will be higher and very dependent on the duration of the studied period.

4.5. Results

In this section, the outputs of the tool are presented for both operational modes.

4.5.1. Real time operation (internal charging)

Real time operation mode outputs consist on the world maps shown in Figures 4.7 and 4.8, representing 16 and 21 January 2026 at time 16:05 UTC as examples, respectively. Over the left maps, two data belts are plotted, the upper one concerning flux averaged every hour and the lower one translating such flux levels into internal charging risk. Meanwhile, the right maps are similarly built but using fluence instead of flux. The risk levels are the ones introduced in Table 2.3 for flux (SeNMEs' E Scale) and 1-day fluence. For both maps, the chosen hourly windows are centered every 15° of longitude, starting from 75°W, where GOES 19 is located. These maps can be used to assess the internal charging risk based on instantaneous flux and 1-day fluence for a satellite located at a specific longitude in GEO. Nevertheless, no real time output can be obtained for surface charging risk, as the low energy electron fluxes are only available with 1 day of delay from GOES data.

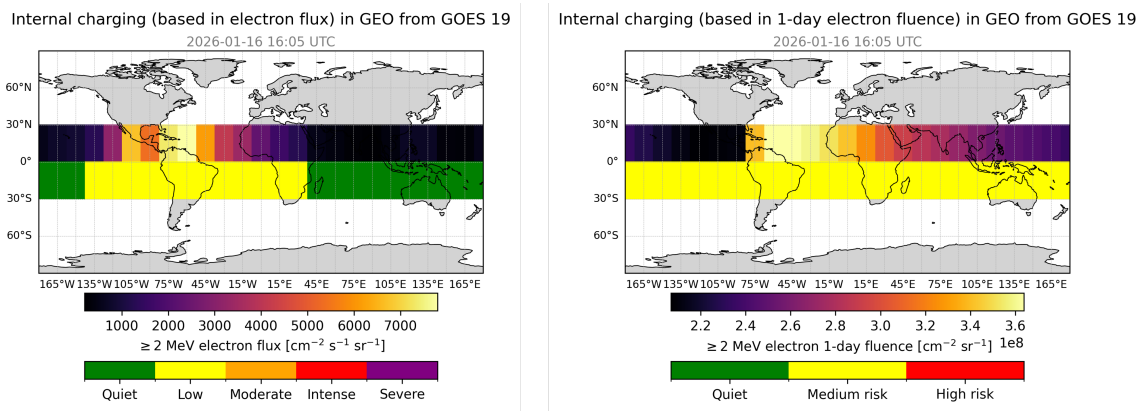

Figure 4.7: Real time operation output for 2026/01/16 at 16:05 UTC.

From Figure 4.7, it can be seen that it was a day with high >2 MeV electron flux levels as measured by GOES 19, which is reflected in the yellow band covering half of the map. Furthermore, the 1-day fluence also shows high values, which means that the previous day the flux values had also been elevated. On the other hand, Figure 4.8 shows lower electron flux levels, with all the longitudes in green, while fluence denotes a higher risk coming from last day higher flux levels.

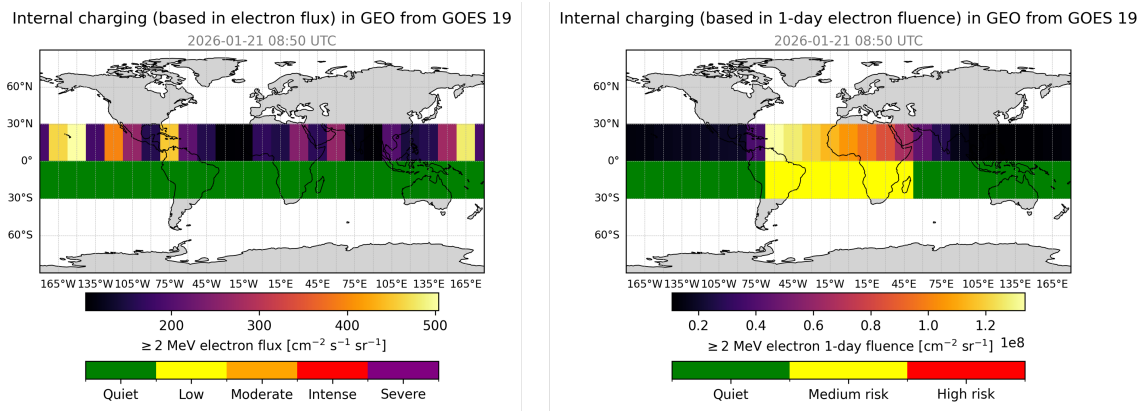

Figure 4.8: Real time operation output for 2026/01/21 at 8:50 UTC.

4.5.2. Long term analysis (internal and surface charging)

Long term analysis outputs include the figures representing high energy electron flux and fluence (internal charging related) in Figures 4.9 and 4.10, and low energy electron flux (surface charging related) in Figure 4.11. These examples of the output of the tool have been calculated for the period of time between 14 to 22 January 2026, which covers the days used for real time analysis. Time is expressed in UTC in all of them, and the measurements, that come from GOES 19, are located according to the GEO longitude of the target satellites (located in these examples at longitudes of 13°E and 136.9°W). This way, a satellite located at the East of GOES 19 will have seen the same fluxes as GOES but some time before, while satellites located at the West of GOES 19 will see the same fluxes later. This allows to locate in UTC time the high fluxes that the target satellite experienced and relate them to possible anomalies whose UTC event time is known, in order to easily identify the possible origin of the anomaly.

The risk thresholds used for these outputs are the corresponding to Tables 2.3 and 2.4, which are the SeNMEs E Scale, whose low threshold is coincident with NOAA's electron flux alert threshold; the 1-day fluence thresholds and the surface charging threshold for 10-50 keV electron flux.

The comparison with the real time mode outputs allows to identify the risk levels shown in the maps from the selected timestamps in real time operation, both in flux and fluence. It is important to notice that in real time operation the information is only available up to the last position of GOES 19 and therefore, as previously explained, the flux at 16:05 UTC on 16 January 2026 (see Figure 4.7) for the longitude of the satellite located at 13°E is assumed to be the one that GOES 19 saw at 16:05 (averaged for that hour) during the previous day. Meanwhile, for the long term plot (Figure 4.10) it can be seen that at 16:05

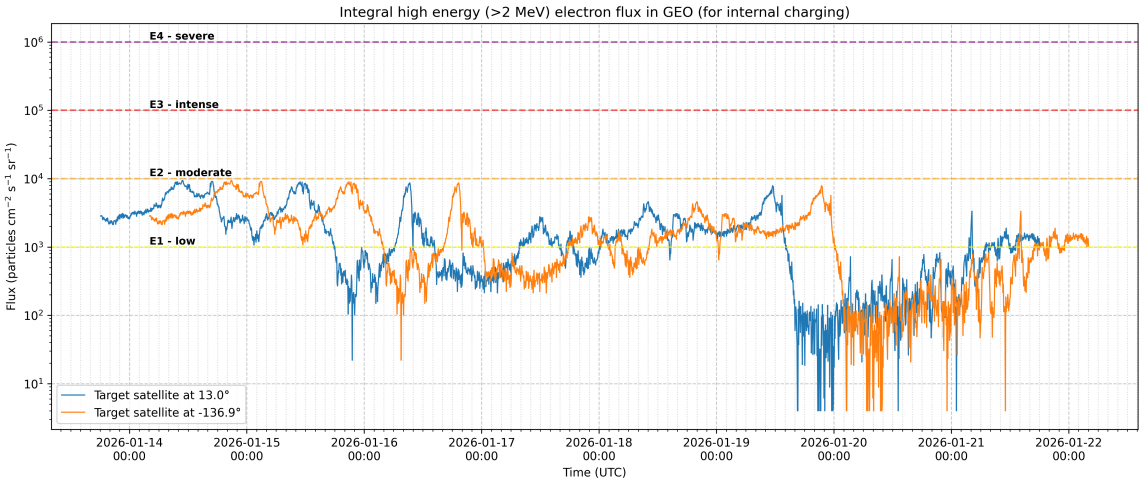

Figure 4.9: Long term analysis output for internal charging risk based in flux during 14 to 19 January 2026.

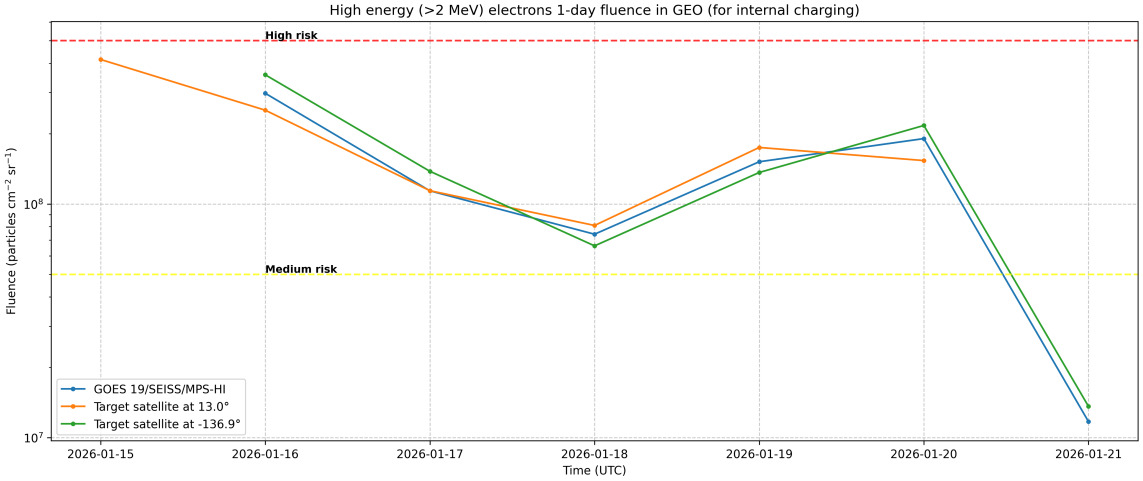

Figure 4.10: Long term analysis output for internal charging risk based in fluence during 14 to 19 January 2026.

UTC for the satellite located at 13°E the flux did not happen to be that high finally, but that information did not exist during the real time plot. Fluence in Figure 4.10, on its side, shows a good agreement with the real time outputs.

Furthermore, referring to the surface charging output (Figure 4.11), it has to be noted that a strong solar storm took place on 19 January 2026 and Kp index shew very high values until the 21 January (it can be consulted in Appendix A.6). This can be seen on Figure 4.11 as a great increase overall in duration of the high values of the flux, clearly reflecting the influence of Kp in low energy electron fluxes. Meanwhile, the high energy fluxes show a decrease during those days (Figure 4.9) but also shew a different behavior

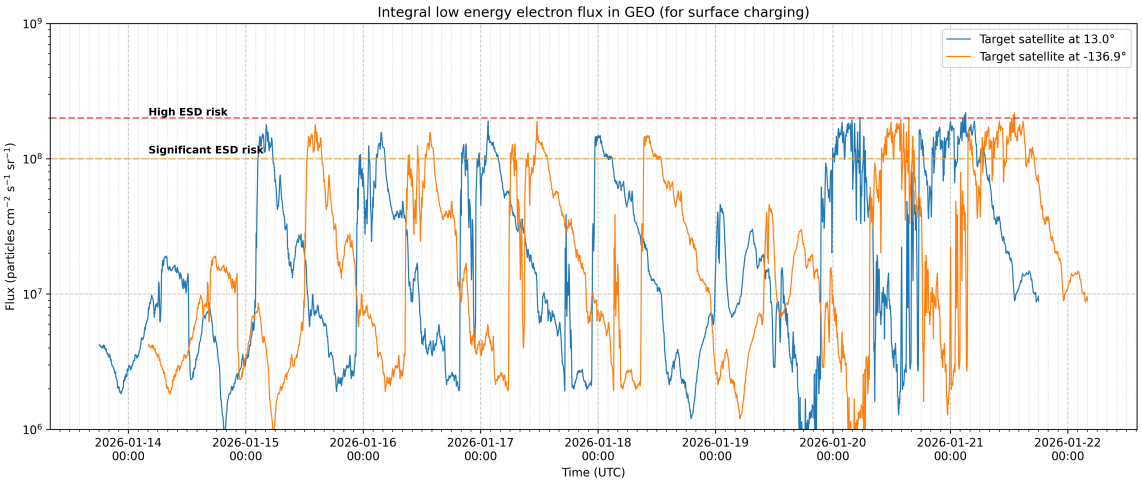

Figure 4.11: Long term analysis output for surface charging risk based in flux during 14 to 19 January 2026.

during the November 2025 storm (Figure 4.2), with an initial high peak, correlated with high energy protons increase and considered as originated by contamination of the electron channels, with a posterior decrease. Therefore, no clear relations can be done between solar radiation and geomagnetic storms (indicated by high energy proton fluxes and Kp) and internal charging risk in the satellite.

4.6. Conclusions

From the tool development and the previous studies about internal and surface charging in GEO, the following conclusions are reached, implying possible future improvements:

- Internal charging is mainly driven by high energy electron fluxes (>2 MeV), that peak around local noon and have their minima around local midnight. The internal charging risk can be assessed through flux level thresholds, as well as fluence values, which are based in older data. Future studies on newer data about anomalies could improve the accuracy of the thresholds and improve their operational effectiveness.
- The data of only one satellite (GOES 19) has been assumed to be valid for risk assessment for the last 24 hours. This is acceptable as a operational assumption, but data from the other studied satellites could be selected and used according to the proximity to the target satellites, as a future expansion of the tool. Nevertheless, that data shows some differences overall in magnitude with GOES 19, presumably due to its omnidirectional character, instead of directional as in GOES, and the intrinsic instrument differences. As time evolution is similar for all the instruments,

some scaling factors could be defined to improve the agreement between instruments for operational use.

- Surface charging is mostly due to low energy electron fluxes (10-50 keV) and shows a high correlation with geomagnetic activity defined by the Kp index. Its nowcast is not possible from GOES data, as it is available with around one day of delay, but its correlation with Kp could lead to an expansion of the tool including alerts that relate Kp to surface charging.
- The used risk thresholds for surface charging seem to frequently imply some risk during local midnight, which gives a very conservative approach. Furthermore, such thresholds are defined for 10-50 keV electron fluxes, while GOES data includes 10-30 keV electron fluxes, but not data between 30 and 50 keV. Nevertheless, they are used as purely indicative thresholds for posterior long term analysis, rather than an alert trigger. As for internal charging, studies concerning recent anomaly data in GEO could lead to the improvement of the accuracy of those thresholds.
- The 50-80 keV electron flux from GOES seem to show increases due to the geomagnetic activity and could lead as well to new risk thresholds, with the advantage that such data is available in real time from GOES. This relation could be studied together with anomalies to define new risk thresholds and expand the tool with nowcast based in that data.

5 | Local geomagnetic disturbance indices

As introduced previously, geomagnetic storms can have strong effects in diverse technologies that are classified using the NOAA's G Scale, which is based in the planetary K index, Kp (see Section 2.2.1 and Section 2.5.3). Furthermore, a local K index can be computed for any observatory that measures the geomagnetic field, as seen in Section 2.5, which might offer more accurate information than the planetary Kp index when referring to specific locations on ground. The objective of this section will be to develop a tool to compute local K indices in a particular position, ingesting data from INTERMAGNET, applying a FMI algorithm version for K computation and estimating the K values in that position based on the ones from the nearby stations.

5.1. Geomagnetic observatory data studies

First of all, a study will be conducted to find out some general limits of validity for the stations' data, with the objective of defining the guidelines for station selection in the tool. The study will be centered in strong solar activity periods, as good behavior of the tool is particularly critical during that time.

The geomagnetic observatories selected for this study belong to the INTERMAGNET network, offering data via the Heliophysics data API (HAPI)[1]. The magnetic field components measured by the stations can be retrieved this way. The X and Y components (the horizontal components) are the inputs needed by the FMI algorithm to compute the local K index associated to the station, using also the station's characteristic K9 limit (see Section 2.5).

[1] See https://imag-data.bgs.ac.uk/GIN_V1/hapi

5.1.1. Local K results calculation

The FMI algorithm implemented version consists on the one available in [6], that needs at least 4 days of data and is based in a procedure where preliminar 3-hour K indices are computed directly from the magnetic data (X and Y components of the magnetic field), and the quiet curve is estimated from those indices and subtracted from the geomagnetic data. The process is repeated two more times starting from the resulting geomagnetic vectors, to finally obtain the estimation of the K indices. This method shows good consistency with the local K indices computed by different national institutes, with typical maximum differences of 1 unit of K (K indices vary between 0 and 9).

Figure 5.1 shows the different geomagnetic observatories used for these preliminary studies over the world map, denoted in the legend by their official three letters codes.

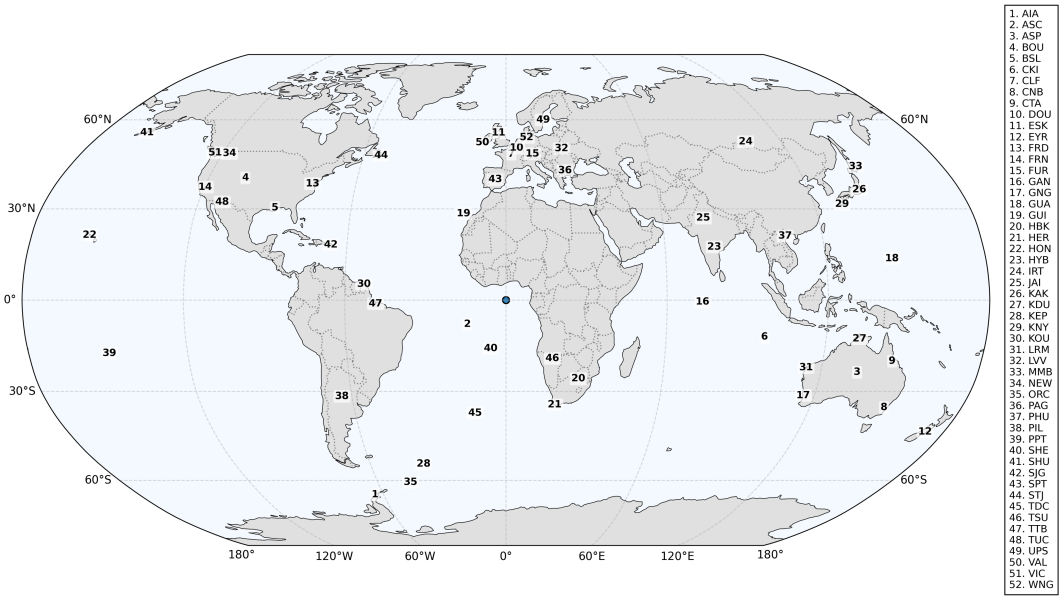

Figure 5.1: Selected geomagnetic observatories over the world map for the November 2025 study.

Data of the two Spanish observatories, one located in Toledo, near the center of the Iberian Peninsula (SPT, with label 43 in Figure 5.1) and the other one in Tenerife, in the Canary Islands (GUI, with label 19 in Figure 5.1) is used. Figure 5.2 shows the K indices for those sites computed during the solar storm of January 2026 using this version of the algorithm.

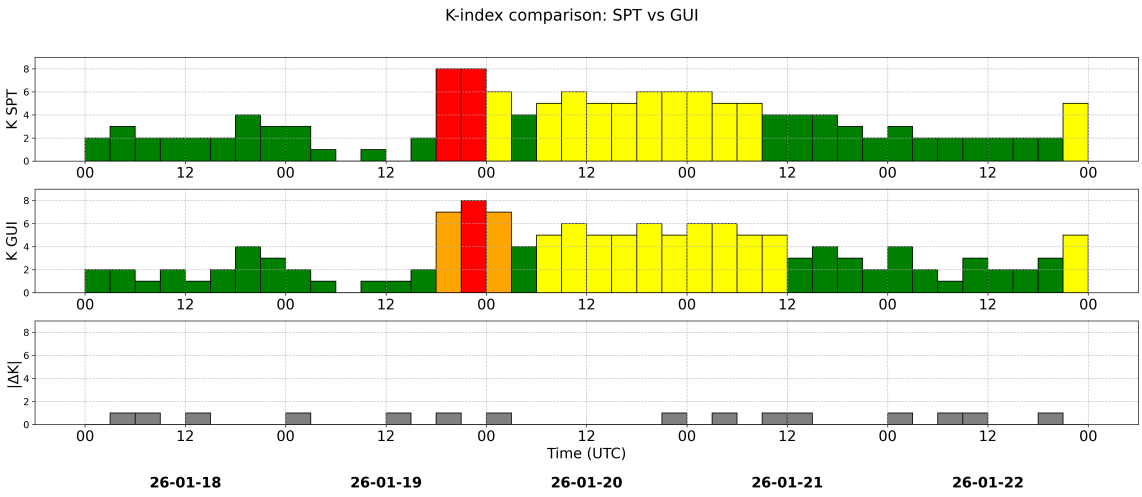

Figure 5.2: Comparison between local K indices in Spain from 18 to 22 January 2026.

The upper plot shows the K index at the SPT site over time in UTC while the middle plot shows the K index at the GUI station. The lower plot shows the difference between them, which can be seen that is always less or equal to one unit of K. Due to the geographical proximity between both observatories, the measurements provide very similar values of K.

5.1.2. Correlation between local K results

As mentioned, this study will address data from several stations located throughout the world, in order to understand the relationship between the distance among stations and the similarity in their K index values.

Therefore, 52 stations have been selected, depicted in Figure 5.1, according to their position and their availability during November 2025. Such month has been selected for the study as there was a strong solar storm that produced very high values of Kp (this can be consulted in Appendix A.6), so quiet and very disturbed time can be then compared for the stations. It is to notice that not all the INTERMAGNET stations were used for the study, as some of them did not provide data during the whole month, entailing data gaps, while other ones have been excluded due to over-representation in the European and North American regions. Furthermore, very high latitude stations (more than 60° North and South) cannot be used either as they do not have an associated K9 limit due to their location, where they are more sensitive to magnetic perturbations, and other indices better fit their measurements, like PC indices (see Section 2.5).

For every station, the 3-hour K index values have been computed during the mentioned

month of November 2025. The K index values of every station is then compared: for every unique pair of stations, two correlation metrics have been calculated. The first chosen metric is the Pearson correlation coefficient, also used and defined in Section 4.2, that addresses the strength of the linear relationship between the measurements from both stations in a pair, which will provide information about the similarities in the time evolution of the K values. To also assess the equality of the K indices from different stations, the second chosen metric is the percentage of same values of K.

Figure 5.3 shows all the points corresponding to each unique pair of stations, located on the grid according to their separation in km along longitude and latitude and colored in relation with the Pearson correlation coefficient (left plot) and the percentage of same K values (right plot). The representation of the separation of the stations in both geographical coordinates has been decided to study variations in both directions and possible different effects associated to them. For latitude, such distance is simply computed like the product of the Earth radius and the difference in latitude in absolute value. Meanwhile, for longitude, as a division of one degree in longitude is different according to the latitude, it has been decided to consider the mean latitude between the stations, so the distance in km along longitude can be computed as the product of the Earth radius, the cosine of the mean latitude and the difference in longitude. It can be seen that distance in longitude does not overcome 20000 km, which is almost half of the Earth's equatorial perimeter, while distance in latitude does not overcome 14000 km, which corresponds to a maximum difference of around 126°. This is consistent with the stations' location, as they are located between approximately 60° North and South. Geographical coordinates have been used instead of geomagnetic ones to compute physical meaningful quantities, as geomagnetic coordinates are not spherical so distances in km cannot be computed along the coordinates without inaccuracies and angular differences in coordinates do not represent real separation between stations in longitude, as just explained. Furthermore, close stations will have close geographical and geomagnetic coordinates, so differences would not be high. In total, 240 values of K are computed per station, corresponding to the 8 daily values of K (expressed in 3-hour intervals) and the 30 days of November.

The results displayed in this Figure 5.3 show that the highest values in correlation coefficient and percentage of same values are gathered in the quadrant from 0 to 2000 km in both directions. Outside that region, results suggest that correlations show a higher variation along longitude for a given lapse of latitude than vice versa. That is, two stations separated by a fixed longitude are not likely to experiment a big variation in their correlations when changing their latitudinal separation, but two stations separated by a fixed latitude are more likely to experiment bigger variations in their correlations when

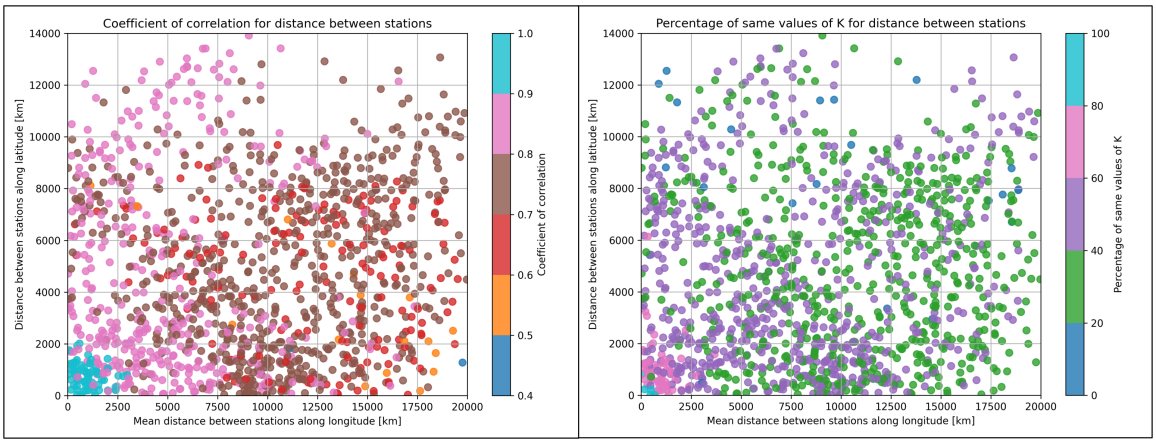

Figure 5.3: Correlation metrics for geomagnetic observatories around the globe for distances along geographical longitude and latitude. Left: Pearson correlation coefficient. Right: Percentage of same K values.

changing their longitudinal separation (excluding in both cases the highest correlation quadrant). This can be attributed to the variation of the local indices with local time, as seen in Section 2.5.

Two other metrics of the comparison of the calculated K index values between two stations have been chosen: the number of more than 2 and 3 units of K differences between datasets, in order to characterize the number of big errors that can be expected. Figure 5.4 shows the percentages of compared K values that show a disagreement in 2 or more and 3 or more units of K, respectively for the left and right plots.

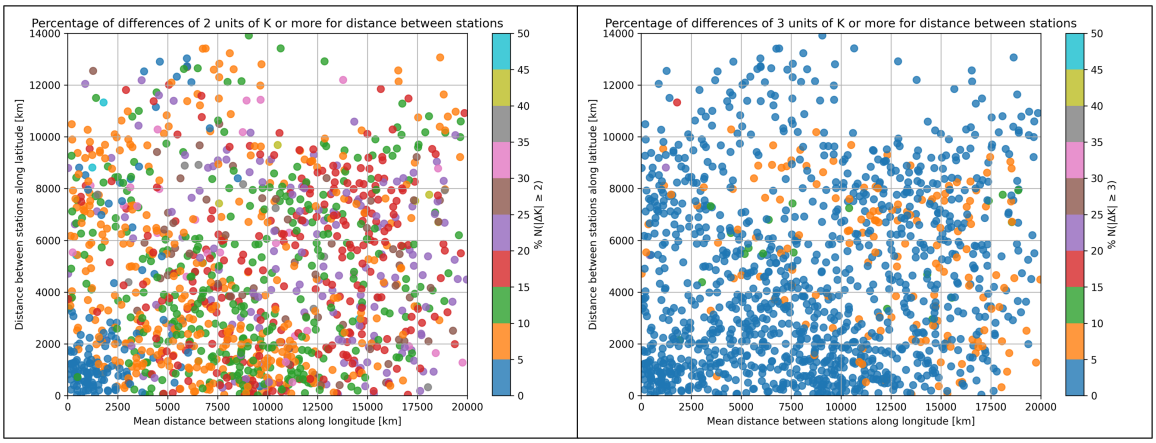

Figure 5.4: Correlation metrics for geomagnetic observatories around the globe by difference in magnetic coordinates. Left: Percentage of differences greater than 2 units of K. Right: Percentage of differences greater than 3 units of K.

Again, the values that imply good correlation, that is, very low percentages, congregate in

the 0 to 2000 km distance values for both directions. Furthermore, the differences in 3 or more units of K remain relatively low for almost all the station pairs. Figure 5.3 showed that the greatest results in percentage of same K values are mainly between 60 and 80 %, which together with the results from Figure 5.4, indicates that for many pairs of values there is a difference of 1 unit of K. This difference can also be seen in the lower plot of the Figure 5.2. Those small differences in K cannot be avoided and can be considered as a minimal uncertainty when assuming the values of K from one station to assess a nearby location.

The present results show therefore that when the distance along longitude and latitude is among 0 and 2000 km, the pairs of stations correlate very well, showing similar results in terms of temporal evolution and small differences in numeric values. As the distance values coincide for the accepted interval along both coordinates, the range of accepted stations around the location where K needs to be computed can be determined by a circle of 2000 km of radius.

5.1.3. Averaging of local K values

After having studied the correlation between stations according to their relative positions, it is interesting to study whether the values of K from different stations can be averaged in order to produce an estimation of K at some location where there is not a clear closest station (for example, for the case in which the distance between the location and the closest station is higher than the 2000 km distance established in the previous study).

Therefore, a new study is conducted with the data from November 2025 for different sets of stations. A location is chosen coincident with a certain station for validation, so K values are computed by averaging a number of chosen nearby stations, such that the validation station is approximately located at the center of them. Those averaged K values are compared with the values from the selected central station, using the same correlation metrics that were previously chosen, that is, the Pearson correlation coefficient, the percentage of same K values, the percentage of differences of 2 units of K or more, and the percentage of differences of 3 units of K or more. The total number of K values for this period is again 240, as the same time period analysis has been selected. To calculate the K at the location, the following approach has been followed: the weights for the averaging of K are chosen as inversely proportional to the distance from the central location to each station. That distance is computed as a great circle distance between the geographic coordinates of both locations through the Haversine formula:

$$d = 2R \arcsin\left(\sqrt{\sin^2\left(\frac{\varphi_2 - \varphi_1}{2}\right) + \cos(\varphi_1)\cos(\varphi_2)\sin^2\left(\frac{\lambda_2 - \lambda_1}{2}\right)}\right) \tag{5.1}$$

where (φ,λ) are the set of latitude and longitude and R is the Earth's radius. This formula assumes sphericity of Earth.

The results are gathered in Table 5.1, where the same procedure has been followed for five different cases. All the used stations can be seen over the world map in Figure 5.1.

Table 5.1: Results of averaging K for different sets of stations. Corr denotes the Pearson correlation coefficient, % Same K the percentage of values of K that are equal in the comparison, % N($\Delta K \geq 2$) and % N($\Delta K \geq 3$) the percentage of differences greater or equal than 2 and 3 units of K, respectively, in the comparison.

Set of stations	**Corr**	**% Same K**	**% N($\Delta K \geq 2$)**	**% N($\Delta K \geq 3$)**
North America (around BOU) with close stations (less than 2500 km)				
TUC	0.92	66.67	0.83	0
TUC, FRN	0.92	66.67	0.83	0
TUC, FRN, NEW, BSL	0.93	70.83	0.42	0
TUC, FRN, NEW, BSL, VIC, FRD	0.94	72.92	0	0
North America (around BOU) with far stations (from 4000 to 6500 km)				
STJ	0.85	28.75	16.67	1.25
STJ, SHU	0.87	53.75	9.58	0.42
STJ, SHU, HON, KOU	0.88	52.92	4.17	0.42
Atlantic Ocean (around GUI) with far stations (from 2500 to 5000 km)				
VAL	0.88	46.22	5.42	0
VAL, STJ	0.88	57.92	1.25	0
VAL, STJ, PAG, SJG	0.89	61.67	0.42	0
Pacific Ocean (around HON) with far stations (from 3500 to 6000 km)				
SHU	0.76	39.33	13.33	3.75
SHU, FRN	0.76	38.91	12.08	2.5
SHU, FRN, PPT, GUA	0.90	57.74	1.25	0
Atlantic Ocean (around GUI) with very far stations (from 8000 to 10000 km)				
PIL	0.77	27.92	25.42	4.17
PIL, IRT	0.81	32.08	16.25	2.01
PIL, IRT, GAN, SHU	0.84	48.75	10	0.42

Firstly, the average K index at a location with the same coordinates as BOU station is computed and compared to the BOU K index values. For the average calculation, six close stations (less than 2500 km) are used. K values are computed by assuming only the closest station (TUC), and by averaging 2, 4 and all the 6 stations, chosen by proximity order. From the results it can be seen that the correlation coefficients remain very close for

all the combinations, slightly improving when adding more stations, while the percentage of same K values is also increased. The percentages of 2 or more units of K are very small and eventually reduced to zero by using the six stations, while no differences equal or bigger than 3 units happen.

The same study is repeated but selecting 4 further stations, from 4000 to 6500 km of distance. The results show that, even if correlation is still high and slightly improves with the number of stations, the percentage of same values does increase more than a 20% and the number of differences in K units is also reduced. The averaging results show a better performance here than only using the closest station.

Those results are repeated in the two following studies, with locations selected around stations GUI and HON and with chosen stations for the k index average calculation located from 2500 to 5000 km and from 3500 to 6000 km, respectively. Using 4 stations for averaging can considerably improve the correlation and the percentage of same K values, while reducing the number of differences of 3 units or more of K to zero.

Finally, the last study has been done using a location around GUI station and selecting very far stations for the averaging (from 8000 to 10000 km). The study still shows an improvement when using two and four stations to average, but the errors in 2 units or K or more cannot be as reduced as in the previous studies. This suggests a distance of around 6000 km as the maximum one that should be used to include the stations for averaging, considering the reduction to a negligible percentage of big error as the cut off criteria.

The maximum distance from any point on the Earth's surface to the closest station can be retrieved by using a spherical Voronoi diagram [3], generated from all the stations included in the database. Notice that those stations are not only the ones depicted in Figure 5.1, but all the stations available in INTERMAGNET that regularly provide data. The biggest difference between both sets is a much higher number of stations in Europe and some stations in other regions that did not offer data during the whole month of November 2025 and were therefore not included in the study. The mentioned Voronoi diagram divides the world in regions such that every region includes the closer points to a certain station. The segments composing the diagram indicate an equal proximity from two stations and the vertices indicate the intersection of three or more segments, and therefore the equal proximity of three or more stations. The maximum distance from any point to the closest station will be in one of those vertices, which can be found by computing the distance from all the vertices to all the stations, keeping the smallest distances for every vertex and retrieving the maximum one from those distances. This

way, the nominal most isolated location on Earth would be (51.53°S, 69.08°E), with a distance to the closest stations of 4363.8 km.

Therefore, the nominal worst case would imply stations being located from 4363.8 km. Furthermore, it can be studied the worst case for the 10^{th} closest station to each Voronoi vertex, which is 6703.8 km. This implies that, when all the considered stations are operative, and even if some of them are not, there should be enough stations around any point to do the averaging of K and obtain good results, according to the previous studies.

5.1.4. Conclusions from the studies

To summarize, the previous studies throw the following conclusions about the station selection and the computation of the K indices, which will be considered for the tool development:

- When there is a station in a range of less than around 2000 km of distance from a certain point, it is possible to estimate the K indices in such point as equal to the ones from that station, without assuming major errors.
- In a range that can be considered from 2000 km to around 7000 km for the distances from the points to the closer stations, estimating the K indices by averaging the ones from those nearby stations, preferably located around the point such that it remains in the center among them, gives good results in terms of increasing the percentage of similar K values and reducing big errors to a negligible percentage of the values.
- The expected cases when a reasonable number of stations are operative is to have many close stations less than 6000-7000 km away from any point, so the averaging method should bring good results in nominal operation.
- The geographical limitations about where the computation of K indices is possible are determined by the K9 limits of the stations, which is needed to apply the FMI algorithm for K computation. This reduces the region where such indices are possible to compute and more physically meaningful between $\pm 60°$ of latitude. In the polar regions other indices shall be considered to assess geomagnetic activity instead of K indices, due to the more sensitive to the magnetic perturbations nature of these zones.

5.2. Method

From the conclusions reached by the previous studies, a tool can be designed to estimate the local values of the K index from the stations belonging to the INTERMAGNET network. The stations stored in the tool comprise all regularly operational INTERMAGNET stations with known values of the K9 limit (located between around ±60° of latitude).

The scheme of the tool is presented in Figure 5.5. The required inputs are a location, given by geographical longitude and latitude, and a period of time given by a start and end date. It is recommended that this period covers at least 4 days for the optimal performance of the FMI algorithm. The outputs of the tool are the estimated local K indices for the introduced location, expressed in the 3-hour intervals used for Kp (0-3, 3-6, 6-9, 9-12, ...) in UTC time.

The tool integrates the following workflow, as described in Figure 5.5:

- Organization of the list of stations according to the great circle distance between the location and the stations.
- When there are available stations closer than 2000 km, as determined previously, the K indices can be estimated as equal to the ones from the closest station. This so-called Closest Station Approach aims at computing those indices for the first station in the ordered list if it is closer than 2000 km to the location. If the data for the station is not valid (see valid data criteria after this summary), the next station is considered, until a station provides valid data or there are no stations closer than 2000 km.
- When no stations closer than 2000 km are operative or offering valid data, the tool skips to the second approach, called the Averaging Stations Approach, which consists of averaging the K indices from the four nearest stations (considering distances up to 7000 km), weighting with the inverses of their distances to the location. If one of those stations do not offer reliable data, the next station in the list is considered, as far as it is located less than 7000 km from the location.
- If no stations closer than 7000 km offer reliable data, or less than 2 stations are available for the Averaging Stations Approach, the tool won't be able to retrieve meaningful values for the local K, so no results can be obtained.

It is to notice that according to the previous studies, the Averaging Stations Approach can provide good results when using stations located from 0 to around 6000-7000 km to the location. In the tool, when stations closer to 2000 km are available and offer valid data,

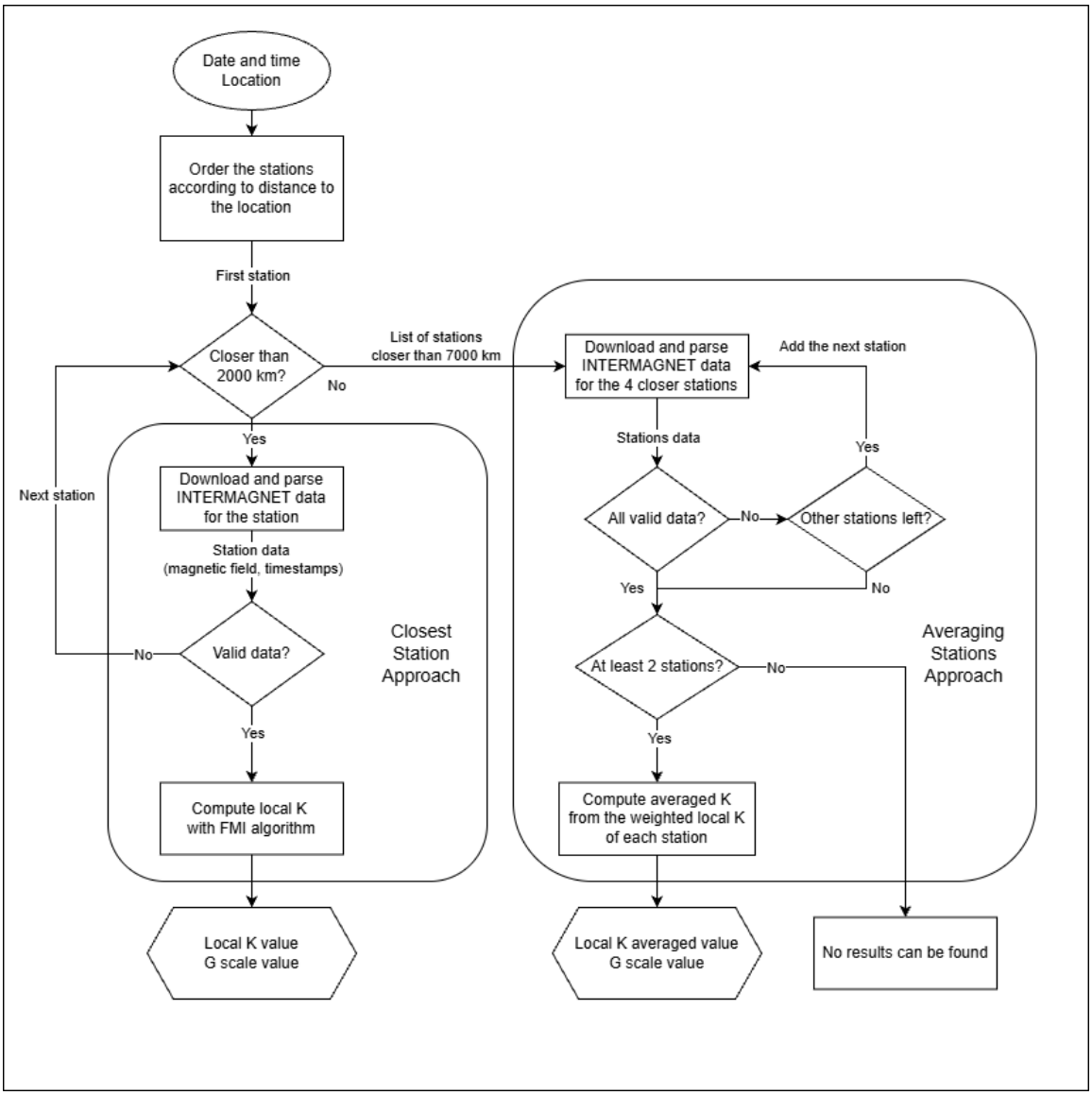

Figure 5.5: Scheme of the tool for geomagnetic disturbance risk assessment.

it has been decided to assume their indices as representative for the location in order to improve performance and keep a simple logic, as results are expected to be very accurate with only one station, and they only slightly improve when averaging within that range of distances.

About the retrieved magnetic field data for a station, every data gap of 15 minutes or less is linearly interpolated, as is done in [35]. Following that same reference, the required minimum values of samples in each 3-hour interval (180 samples, one per minute) is at least 90 samples, which is half of the samples. If the valid samples are not enough, the corresponding time interval is considered of bad quality. The non valid samples are indicated in INTERMAGNET data by a fill value, typically 99999.0, which is indicated

and retrieved from the metadata from each station. If the initial time and/or the final time do not align with the 3-hour intervals, the expected number of samples will be lower than 180, and therefore, according to the interval duration, that quantity is computed and at least half the samples must be reliable to consider the interval valid. This implies some caution at the time of setting the interval times, as it will be more reliable and the value of K more representative if they coincide with the 3-hour intervals.

Within the Closest Station Approach, the dataset from the current station is only considered valid if all the intervals included are valid, to provide fully coverage of all the introduced period. Meanwhile, for the Averaging Stations Approach, a station can be used even with some non valid periods, as far as the number of valid periods is greater than half the total number of periods. Those non valid periods are filtered to not be considered. This is done as the eliminated periods will likely be covered by any of the other three stations. This implies that even if a station was not used for the first approach as it didn't offer full coverage of the data, it can still be used for the second one as its proximity can improve the averaging results. If any of the used stations offer data for a coincident interval, the output would show a lack of results for such interval.

5.3. Results

The outputs of the tool are a first plot, representing the calculated K index values for the specified time interval, and a second one showing the introduced location and the used stations on the map.

Figure 5.6 shows the first output for the coordinates of Milan during the storm of January 2026, as an example of the Closest Station Approach. The closest station is the Black Forest Observatory in Germany, whose K index is computed from its retrieved geomagnetic data as explained in the tool's method. Both locations are shown on the left plot of the Figure 5.8 represented over a regional map, with the introduced location as a red dot and the used stations as yellow dots with their names indicated.

Figure 5.7 shows the corresponding output for the coordinates of the most isolated point described in Section 5.1.3, that is (51.53°S, 69.08°E), during the storm of November 2025, obtained with the tool by the Averaging Stations Approach. The location and the stations used for this analysis are shown in the right plot of Figure 5.8. For the averaging process, the stations used due to the distance and availability as explained are Hartebeesthoek (HBK) and Hermanus (HER) stations in South Africa, Neumayer station in Antarctica (VNA) and Gingin (GNG) in Australia.

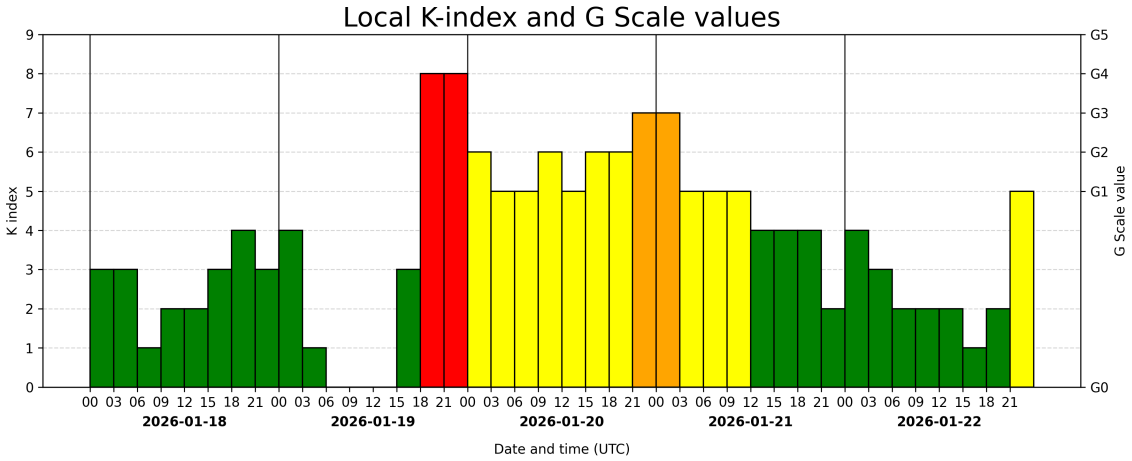

Figure 5.6: Local K index and G scale values output from the Closest Station Approach.

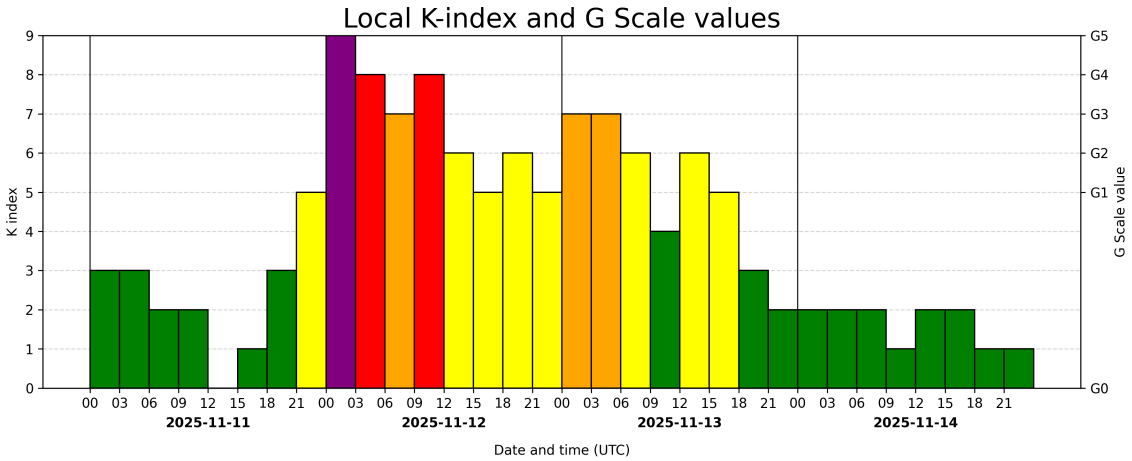

Figure 5.7: Local K index and G scale values output from the Averaging Stations Approach.

In both examples (Figures 5.6 and 5.7), the outputs show similar graphs, with the K index value in the left vertical axis, the corresponding G Scale value in the right vertical axis and the days and time intervals in UTC in the horizontal axis. The G Scale can be related to the various effects of geomagnetic disturbances as collected in Section 2.5.3. A color code completes the graph, coloring the bars in green for K between 0 and 4, in yellow for K of 5 and 6, in orange for K equal to 7, in red for K equal to 8 and purple for K equal to 9. This code is inspired in the one used by the Spanish Space Weather Service (SeNMEs, [59]) to characterize different levels of activity: quiet, low, moderate, intense and severe, respectively.

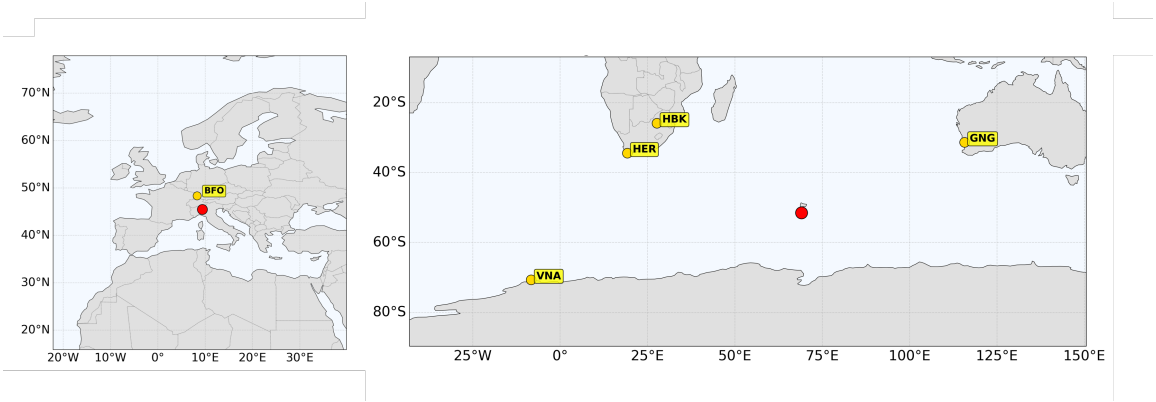

Figure 5.8: Specified location and used stations output for both the Closest Station Approach (left) and the Averaging Stations Approach (right).

5.4. Conclusions

Finally, some conclusions and future development concerning the local geomagnetic disturbances tool are listed:

- The developed tool is able to retrieve geomagnetic data from INTERMAGNET and compute the local K indices at any position during a certain period of time, as far as there are enough operative stations. When there are stations closer than 2000 km a Closest Station Approach is followed to assume the indices as equal to the closest station, only if it is offering enough valid data. If no stations are that close to the location, but there are enough station available closer than 7000 km the Averaging Stations Approach estimates the K indices by an averaging process based on the distances from the stations to the location.
- The tool can operate in near-real time as the majority of the stations update their data continuously. Nevertheless, some stations offer their data with some days or delay, so results can vary when applying the tool to near-real time or studying the period some time later. All the dates are managed in UTC.
- The tool uses data from stations located from approximately 60°N to 60°S, as higher latitude stations do not have K9 limits defined. Therefore, locations used as inputs should not be located outside that range as the results would not be representative.
- If all the stations included in the tool are operative, every location in the mentioned region of Earth (±60°) could be assessed with the tool by one or another approach. If some stations are not operative or offering reliable data, it can happen that a specified location cannot be assessed at all and in that case no results can be

returned. An alternative in this case would be to use the planetary K index (Kp) to assess the geomagnetic disturbances.

- Further developments associated to the tool could consist in covering the missing regions (from $\pm 60^{\circ}$ to the poles) by including different geomagnetic indices or ways to quantify the geomagnetic perturbations.

6 | Conclusions and future work

The general conclusions of the work concerning the developed tools and their possible future expansions are included in this final chapter. More specific conclusions about the tool parameters and design are collected in their own chapters, together with the specific conclusions from their complementary studies.

6.1. Radiation dose estimation at flight altitudes

The first tool consists on estimating the effective dose rates related to ionizing radiation at flight levels caused by galactic cosmic rays (GCR) and solar activity, with ground level enhancements (GLE) as atmospheric consequences of solar radiation storms, as described in Chapter 3. This tool can operate in near-real time to detect whether a GLE is on going or the atmospheric radiation scenario is dominated by GCR, by processing neutron count rates in several stations from the Neutron Monitor Database (NMDB) through the GLE Alert+ algorithm. Depending on the detected scenario, GCR or GLE, the AniMAIRE model is applied in two different modalities for the effective dose rates computation, using the neutron count rates at some specific stations as input, and a D-Index and ICAO/FAA alerts about risky radiation levels are calculated for operational use. Apart from near-real time, the tool can also deal with specified periods of data for post-flight analysis.

The limits of the tool are set to 30 km of altitude for GCR scenario and 20 km for GLE scenario. Moreover, the GLE detection algorithm is expected to work for strong GLE events, which are the ones that produce a radiation environment worth to analyze with the AniMAIRE model for GLE. Weaker GLEs which cannot be detected would produce similar results when assessed with AniMAIRE model for GCR and GLE, so their detection is not essential. Nevertheless, the algorithm can be easily modified to detect weaker GLEs by reducing the stations threshold for alert identification and introducing the GOES proton flux of 100 MeV as a secondary GLE indicator. A tricky situation for the tool occurs if a Forbush decrease reduces the neutron count rates before a GLE takes place, so the increase in neutron count rate between the regular baseline and the GLE levels is not representative as input for the particle spectra. This limitation remains

unresolved and should be addressed in future developments.

Another important limitation of the model is that the used AniMAIRE functions depend on the neutron count rate from Oulu station. The rate is needed to compute the particle spectra involved in the effective dose estimation for GCR and GLE modes. Furthermore, GLE mode also needs the neutron count rate from another station, with the results becoming dependent on the availability of the second station. As a future development, to solve this dependence on specific stations, the particle spectra could be calculated following different procedures like other models implement, from all the available neutron stations or satellite data like GOES. This can be implemented to compute the spectra as the input for AniMAIRE, that offer other functions to compute the effective dose rates from such spectra. Anisotropy of the GLEs can also be introduced in the tool by analyzing the particle data to determine an arrival direction, which is also accepted as input by AniMAIRE functions. The current tool assumes isotropy of the GLE, being a more conservative approach for radiation estimation.

6.2. Internal and surface charging in GEO

The second developed tool, described in Chapter 4, aims to provide a nowcast for internal charging risk and a post-mission analysis for both internal and surface charging risk for GEO satellites, based in GOES 19 data. Internal charging risk can be related to high energy electron fluxes (>2 MeV) and their integration in time (fluence), while surface charging corresponds to low energy electron fluxes (10-50 keV), through well established risk thresholds described in Literature. Studies have been conducted to compare the fluxes as measured from different instruments during several days of quiet and high solar activity, concluding that high and low energy fluxes have a strong dependence on Local Solar Time. Therefore, both charging risks can be inferred for specific locations in GEO by particularizing the measurements of one single instrument according to the Local Solar Time of each GEO position. GOES 19 has been decided to be used for that purpose as it is NOAA's primary satellite for electron flux data.

The tool therefore operates in two different modes, real time and long term analysis. Real time mode does not need any input and produces a map of the internal charging risk in GEO based in GOES 19 more than 2 MeV electron flux data (using its last 24 hour measurements averaged in one hour bins) and 1-day fluence computed from the flux integration (needing therefore the last 48 hours of GOES 19 data). Meanwhile, long term analysis mode is designed to retrieve GOES 19 data (both >2 MeV and 10-50 keV electron fluxes) and particularize it to a target satellite characterized by its GEO longitude. This

way, it produces plots of the data (for high and low energy fluxes) indicating the UTC time at which each satellite has seen the corresponding flux, together with the risk thresholds. This way, detected anomalies can be easily characterized as internal or surface charging if their respective associated fluxes experienced unusual high values. This tool is therefore based in the assumption that the electron flux in GEO does not experiment a great variation during a one day period, which is supported by the conducted studies.

A possible future development for the tool would be including the data from other instruments apart from GOES 19, which would need some scaling process, as even if time evolution is similar for all the instruments, the magnitude of the measurements differs. Furthermore, the used risk thresholds could be updated with more recent anomaly data, as they come from older satellite measurements and anomaly databases. A nowcast approach to surface charging could also be introduced in relation with the Kp index, as well as with the 50-80 keV electron flux which is offered in real time by GOES satellites.

6.3. Local geomagnetic disturbance indices

The last developed tool, from Chapter 5, consists on the estimation of local K indices to assess geomagnetic disturbances, related to their various effects with the G Scale. The local K index for a certain station (from the INTERMAGNET network) can be computed from its geomagnetic measurements, particularly the horizontal components of the magnetic field, by applying the FMI algorithm. Local K indices have a validity of around 2000 km of distance from a central point, as concluded from one of the conducted studies.

The tool can apply two different approaches to estimate the local K index for a given position at a certain period of time. The first one, called Closest Station Approach, consists on using data from the closest station within a range of 2000 km from the location and the estimated values are equal to the retrieved K values for that station. Meanwhile, if there are no stations that close or data is not fully valid, the Averaging Stations Approach is applied instead. It takes the data from the four closest stations in a range from 2000 to 7000 km and computes an averaged K index, weighting each station indices according to the inverse of its distance to the location. According to the conducted studies, this gives accurate results for the mentioned range of distances. The use of one or another approach depends on the operative stations at the specified period and near the location, and it could happen that no approach can be followed due to those factors, so no results can be retrieved. Nevertheless, this case is supposed to be extremely unusual as the number of current operative stations is high and they are well distributed around the world.

The limitations of the tool consist mainly on the areas where it can be used, between 60° North and South, as the K indices are only meaningful in such latitudes. As a future development, Polar Cap indices could be introduced to measure geomagnetic activity in the polar regions.

Bibliography

[1] Airbus. Airbus update on a320 family precautionary fleet action, Nov. 2025. URL https://www.airbus.com/en/newsroom/press-releases/2025-11-airbus-update-on-a320-family-precautionary-fleet-action. Press Release.

[2] M. Anzorena, E. de la Fuente, K. Fujita, R. Garcia, Y. Hayashi, K. Hibino, N. Hotta, G. Imaizumi, Y. Katayose, C. Kato, S. Kato, T. Kawashima, K. Kawata, M. Kobayashi, S. Kobayashi, T. Koi, H. Kojima, P. Miranda, S. Mitsuishi, A. Mizuno, K. Munakata, Y. Nakamura, M. Nishizawa, Y. Noguchi, S. Ogio, M. Ohishi, M. Ohnishi, A. Oshima, M. Raljevic, H. Rivera, T. Saito, T. Sako, T. K. Sako, S. Shibata, A. Shiomi, M. Subieta, F. Sugimoto, N. Tajima, W. Takano, Y. Takeyama, M. Takita, N. Tamaki, Y. Tameda, K. Tanaka, R. Ticona, H. Tsuchiya, Y. Tsunesada, S. Udo, G. Yamagishi, Y. Yamanaka, K. Yamazaki, and Y. Yokoe. Observation of the forbush decrease on 2024 may 10, using the ALPAQUITA air-shower array at the 70–1000 GV rigidity range. *The Astrophysical Journal*, 998(1):16, feb 2026. doi: 10.3847/1538-4357/ae353c. URL https://dx.doi.org/10.3847/1538-4357/ae353c.

[3] F. Aurenhammer, R. Klein, and D.-T. Lee. *Voronoi Diagrams and Delaunay Triangulations*. World Scientific, Singapore, 2013. ISBN 978-981-4447-63-8.

[4] J. Bartels. The geomagnetic measures for the time-variations of solar corpuscular radiation, described for use in correlation studies in other geophysical fields. *Annals of the International Geophysical Year*, 4:227–236, 1957.

[5] BBC Future. How cosmic rays grounded thousands of aircraft, Dec. 2025. URL https://www.bbc.com/future/article/20251201-how-cosmic-rays-grounded-thousands-of-aircraft. Accessed: 2025-12-05.

[6] S. Blake. K-indexcalculator. https://github.com/TCDSolar/K-IndexCalculator, 2016. Accessed: 2026-02-03.

[7] D. H. Boteler. A 21st century view of the March 1989 magnetic storm. *Space Weather*, 17(10):1427–1441, 2019. doi: 10.1029/2019SW002278.

[8] S. Bourdarie and O. Le Traon. Hotbird 13f and 13g ICARE-NG level 1 data description. Technical note, ONERA, September 2024. URL https://swe.ssa.esa.int/documents/d/guest/hotbird_13f_13g_icareng2_l1_data_description. Data description document for ESA Space Weather Service Network.

[9] N. Buzulukova and B. Tsurutani. Space weather: From solar origins to risks and hazards evolving in time. *Frontiers in Astronomy and Space Sciences*, 9:1017103, 2022. doi: 10.3389/fspas.2022.1017103. URL https://doi.org/10.3389/fspas.2022.1017103.

[10] H. V. Cane. Coronal mass ejections and forbush decreases. *Space Science Reviews*, 93(1):55–77, 2000. doi: 10.1023/A:1026532125747.

[11] H.-S. Choi, J. Lee, K.-S. Cho, Y.-S. Kwak, I.-H. Cho, Y.-D. Park, Y.-H. Kim, D. N. Baker, G. D. Reeves, and D.-K. Lee. Analysis of geo spacecraft anomalies: Space weather relationships. *Space Weather*, 9(6):S06001, 2011. doi: 10.1029/2010SW000597.

[12] C. S. W. Davis, F. Baird, F. Lei, K. Ryden, and C. Dyer. AniMAIRE—a new openly available tool for calculating atmospheric ionising radiation dose rates and single event effects during anisotropic conditions. *Space Weather*, 22:e2024SW003985, 2024. doi: 10.1029/2024SW003985.

[13] C. S. W. Davis, F. Lei, F. Baird, K. Ryden, and C. Dyer. AniMAIRE: Anisotropic model for atmospheric ionising radiation effects. https://github.com/ssc-maire/AniMAIRE-public, 2024. Accessed: 2024-05-03.

[14] European Space Agency. What is Space Weather? https://swe.ssa.esa.int/what-is-space-weather. Accessed: 2025-10-20.

[15] European Space Agency. Next Generation Radiation Monitor (NGRM) on EDRS-C Level 1 Data Description. Technical Note SPARC-EDRSC-NGRM, ESA Space Weather Service Network, February 2022. URL https://swe.ssa.esa.int/documents/d/guest/edrs_c_ngrm_data_description. Issue 1, Revision 0. Released: 2022-02-28.

[16] European Space Agency. Lessons from the November 2025 solar storm. https://www.esa.int/Space_Safety/Space_weather/Lessons_from_the_November_2025_solar_storm, Nov. 2025. Accessed: 2026-02-10.

[17] European Space Agency. ICARE-NG^2 – space weather, 2025. URL https://swe.ssa.esa.int/en/icare-ng. ESA Space Weather Service Network. Accessed: 2026-01-05.

[18] European Space Agency. NGRM – instrument and data level definitions, 2025. URL https://swe.ssa.esa.int/ngrm. ESA Space Weather Service Network. Accessed: 2026-01-05.

[19] European Space Agency. ESA monitoring January 2026 space weather event. https://www.esa.int/Space_Safety/Space_weather/ESA_monitoring_January_2026_space_weather_event, Jan. 2026. Accessed: 2026-02-10.

[20] A. Ficklin, A. Bruno, L. Blum, N. Cannady, T. G. Guzik, R. Kataoka, K. Munakata, Y. Akaike, and S. Torii. Effects of the may 2024 solar storm on the earth's radiation belts observed by CALET on the international space station. *Geophysical Research Letters*, 2026. doi: 10.1029/2025GL120032. URL https://doi.org/10.1029/2025GL120032. Accepted Author Manuscript.

[21] K. A. Firoz, K.-S. Cho, J. Hwang, D. V. Phani Kumar, J. J. Lee, S. Y. Oh, S. C. Kaushik, K. Kudela, M. Rybanský, and L. I. Dorman. Characteristics of ground-level enhancement-associated solar flares, coronal mass ejections, and solar energetic particles. *Journal of Geophysical Research*, 115:A09105, 2010. doi: 10.1029/2009JA015023.

[22] GFZ German Research Centre for Geosciences. Geomagnetic Kp index, n.d. URL https://kp.gfz.de/en/. Accessed: 2026-02-02.

[23] A. D. P. Hands, F. Lei, C. S. Davis, B. J. Clewer, C. S. Dyer, and K. A. Ryden. A new model for nowcasting the aviation radiation environment with comparisons to in situ measurements during GLEs. *Space Weather*, 20(8):e2022SW003155, 2022. doi: 10.1029/2022SW003155.

[24] R. B. Horne, S. A. Glauert, N. P. Meredith, D. Boscher, V. Maget, D. Heynderickx, and D. Pitchford. Space weather impacts on satellites and forecasting the earth's electron radiation belts with spacecast. *Space Weather*, 11(4):169–186, 2013. doi: 10.1002/swe.20023.

[25] ICRP. The 2007 Recommendations of the International Commission on Radiological Protection (ICRP Publication 103). *Annals of the ICRP*, 37(2-4):1–332, 2007. doi: 10.1177/ANIB_37_2-4. URL https://journals.sagepub.com/doi/pdf/10.1177/ANIB_37_2-4.

[26] Institut de Recherche en Astrophysique et Planétologie. All about the solar flare of january 18, 2026, Jan. 2026. URL https://www.irap.omp.eu/en/2026/01/all-about-the-solar-flare-of-january-18-2026/. News release.

[27] INTERMAGNET. International Real-time Magnetic Observatory Network, n.d. URL https://intermagnet.org/. Accessed: 2026-01-30.

[28] International Civil Aviation Organization. *Manual on Space Weather Information in Support of International Air Navigation*. International Civil Aviation Organization, Montréal, Quebec, Canada, first edition, 2019.

[29] International Service of Geomagnetic Indices. ISGI Reference Service for Geomagnetic Indices, n.d. URL https://isgi.unistra.fr/. Accessed: 2026-01-30.

[30] T. Kuwabara, J. W. Bieber, J. Clem, P. Evenson, and R. Pyle. Development of a ground level enhancement alarm system based upon neutron monitors. *Space Weather*, 4(10):S10001, 2006. doi: 10.1029/2006SW000223.

[31] N. Larsen and A. Mishev. Relationship between NM data and radiation dose at aviation altitudes during GLE events. *Space Weather*, 22:e2024SW003885, 2024. doi: 10.1029/2024SW003885.

[32] N. Larsen, A. Mishev, and I. Usoskin. A new open-source geomagnetosphere propagation tool (OTSO) and its applications. *Journal of Geophysical Research: Space Physics*, 128(3):e2022JA031061, 2023. doi: 10.1029/2022JA031061.

[33] Y. Lu, Q. Shao, H. Yue, and F. Yang. A review of the space environment effects on spacecraft in different orbits. *IEEE Access*, 7:93473–93488, 2019. doi: 10.1109/ACCESS.2019.2927811.

[34] D. Matthiä, M. Schaefer, and M. M. Meier. Economic impact and effectiveness of radiation protection measures in aviation during a ground level enhancement. *Journal of Space Weather and Space Climate*, 5:A17, 2015. doi: 10.1051/swsc/2015014.

[35] J. Matzka, C. Stolle, Y. Yamazaki, O. Bronkalla, and A. Morschhauser. The geomagnetic Kp index and derived indices of geomagnetic activity. *Space Weather*, 19 (5):e2020SW002641, 2021. doi: 10.1029/2020SW002641. URL https://doi.org/10.1029/2020SW002641.

[36] J.-C. Matéo-Vélez, A. Sicard, D. Payan, N. Ganushkina, N. P. Meredith, and I. Sillanpää. Spacecraft surface charging induced by severe environments at geosynchronous orbit. *Space Weather*, 16(1):89–106, 2018. doi: 10.1002/2017SW001689.

[37] H. Mavromichalaki, G. Souvatzoglou, C. Sarlanis, G. Mariatos, A. Papaioannou, A. Belov, E. Eroshenko, and V. Yanke. Implementation of the ground level enhancement alert software at NMDB database. *New Astronomy*, 15(8):744–748, 2010. doi: 10.1016/j.newast.2010.05.009. For the NMDB team.

[38] H. Mavromichalaki, A. Papaioannou, C. Plainaki, M. Sarlanis, G. Souvatzoglou, M. Gerontidou, M. Papailiou, E. Eroshenko, A. Belov, V. Yanke, et al. Applications and usage of the real-time Neutron Monitor Database. *Advances in Space Research*, 47:2210–2222, 2011. doi: 10.1016/j.asr.2011.02.019.

[39] J. Medina, J. J. Blanco, O. García, R. Gómez-Herrero, E. J. Catalán, I. García, M. A. Hidalgo, D. Meziat, M. Prieto, J. Rodríguez-Pacheco, and S. Sánchez. Castilla-la mancha neutron monitor. *Nuclear Instruments and Methods in Physics Research Section A: Accelerators, Spectrometers, Detectors and Associated Equipment*, 727: 97–103, 2013. ISSN 0168-9002. doi: https://doi.org/10.1016/j.nima.2013.06.028.

[40] M. M. Meier and D. Matthiä. Classification and communication of aviation related space weather radiation events. *SF Journal of Aviation and Aeronautical Science*, 1 (1):1002, 2018.

[41] C. J. Mertens, G. P. Gronoff, Y. Zheng, J. Buhler, E. Willis, M. Petrenko, D. Phoenix, I. Jun, and J. Minow. NAIRAS atmospheric and space radiation environment model. *IEEE Transactions on Nuclear Science*, 71(4):618–625, April 2024. doi: 10.1109/TNS.2023.3330675.

[42] C. J. Mertens, G. P. Gronoff, and D. B. Phoenix. NAIRAS version 3 atmospheric ionizing radiation validation: Comparisons to RaD-X measurements. *Space Weather*, 23:e2024SW004296, 2025. doi: 10.1029/2024SW004296.

[43] A. Mishev and I. Usoskin. Numerical model for computation of effective and ambient dose equivalent at flight altitudes – application for dose assessment during gles. *Journal of Space Weather and Space Climate*, 5:A10, 2015. doi: 10.1051/swsc/2015011.

[44] A. Mishev, S. Tuohino, and I. Usoskin. Neutron monitor count rate increase as a proxy for dose rate assessment at aviation altitudes during GLEs. *Journal of Space Weather and Space Climate*, 8:A46, 2018. doi: 10.1051/swsc/2018032.

[45] Y. Miyoshi and R. Kataoka. Solar cycle variations of outer radiation belt and its relationship to solar wind structure dependences. *Journal of Atmospheric and Solar-Terrestrial Physics*, 73(1):77–87, 2011. ISSN 1364-6826. doi: 10.1016/j.jastp.2010.09.031.

[46] National Aeronautics and Space Administration. What is solar activity?, mar 2015. URL https://www.nasa.gov/image-article/what-solar-activity/. Accessed: 2026-02-09.

[47] National Institute of Information and Communications Technology (NICT). WASAVIES (Warning System for Aviation Exposure to Solar Energetic Particles). https://wasavies.nict.go.jp/WorldDose_e.html, 2025. Accessed: 2025-11-27.

[48] National Oceanic and Atmospheric Administration. NOAA Space Weather Scales, n.d. URL https://www.swpc.noaa.gov/sites/default/files/images/NOAAscales.pdf.

[49] National Oceanic and Atmospheric Administration, Space Weather Prediction Center. Space Weather Phenomena. https://www.swpc.noaa.gov/phenomena. Accessed: 2025-10-20.

[50] NOAA National Centers for Environmental Information. GOES-18 SEISS MPS-LO level 1b (L1b) data release provisional data quality: Read-me for data users. Technical report, NOAA National Centers for Environmental Information, November 2022. URL https://data.ngdc.noaa.gov/platforms/solar-space-observing-satellites/goes/goes18/l1b/docs/GOES-18_SEISS_MPS-LO_L1b_Provisional_Maturity_ReadMe.pdf.

[51] NOAA National Centers for Environmental Information. GOES 16-19 SEISS MPS-HI level-2 1-minute and 5-minute flux averages: Read-me for data users. Technical report, NOAA National Centers for Environmental Information, June 2025. URL https://data.ngdc.noaa.gov/platforms/solar-space-observing-satellites/goes/goes18/l2/docs/GOES-R_SEISS_L2_MPS-HI.ReadMe.pdf. Last modified: June 3, 2025.

[52] NOAA National Centers for Environmental Information. GOES-R series SEISS MPS-LO sci-level-1b data readme. Technical report, NOAA National Centers for Environmental Information, May 2025. URL https://data.ngdc.noaa.gov/platforms/solar-space-observing-satellites/goes/goes16/l1b/docs/GOES-R_SEISS_MPS-LO_L1b_Science_Data_ReadMe.pdf.

[53] NOAA Space Weather Prediction Center. GOES electron flux, n.d. URL https://www.swpc.noaa.gov/products/goes-electron-flux.

[54] E. Normand. Single event upset at ground level. *IEEE Transactions on Nuclear Science*, 43(6):2742–2750, 1996. doi: 10.1109/23.556861.

[55] S. V. Poluianov, I. G. Usoskin, A. L. Mishev, M. A. Shea, and D. F. Smart. Gle and sub-gle redefinition in the light of high-altitude polar neutron monitors. *Solar Physics*, 292(11):176, 2017. doi: 10.1007/s11207-017-1202-4.

[56] Y. Quadros de Aguiar, F. Wrobel, J.-L. Autran, and R. García Alía. *Single-Event Effects, from Space to Accelerator Environments: Analysis, Prediction and Hardening by Design*. Springer Nature Switzerland, Cham, Switzerland, 2025. ISBN 978-3-031-71723-9. doi: 10.1007/978-3-031-71723-9.

[57] S2P Data Systems and Space Weather Teams. Programmatic access to SWE data from ESA's Distributed Space Weather Sensor System (D3S) within the SWE Data Centre using HAPI. Technical Note SSA-SWE-HAPI-TN-0001, European Space Agency, January 2025. URL https://swe.ssa.esa.int/documents/d/guest/ssa_swe_hapi_tn_0001. Issue 1, Revision 7.

[58] T. Sato, R. Kataoka, D. Shiota, Y. Kubo, M. Ishii, H. Yasuda, S. Miyake, I. C. Park, and Y. Miyoshi. Real time and automatic analysis program for WASAVIES: Warning system for aviation exposure to solar energetic particles. *Space Weather*, 16 (7):924–936, 2018. doi: 10.1029/2018SW001873.

[59] Servicio Nacional de Meteorología Espacial. Spanish space weather service, n.d.. URL https://www.senmes.es/section/2.

[60] Servicio Nacional de Meteorología Espacial. Radiation environment, n.d.. URL https://www.senmes.es/section/10.

[61] J. A. Simpson. The cosmic ray nucleonic component: The invention and scientific uses of the neutron monitor. *Space Science Reviews*, 93:11–32, 2000. doi: 10.1023/A:1026567706183.

[62] G. Souvatzoglou, A. Papaioannou, H. Mavromichalaki, J. Dimitroulakos, and C. Sarlanis. Optimizing the real-time ground level enhancement alert system based on neutron monitor measurements: Introducing gle alert plus. *Space Weather*, 12(11): 633–649, 2014. doi: 10.1002/2014SW001102.

[63] M. F. Thomsen, M. G. Henderson, and V. K. Jordanova. Statistical properties of the surface-charging environment at geosynchronous orbit. *Space Weather*, 11(5): 237–244, 2013. doi: 10.1002/swe.20049.

[64] B. T. Tsurutani, W. D. Gonzalez, G. S. Lakhina, and S. Alex. The extreme magnetic storm of 1–2 September 1859. *Journal of Geophysical Research: Space Physics*, 108 (A7):1268, 2003. doi: 10.1029/2002JA009504.

[65] B. T. Tsurutani, G. P. Zank, V. J. Sterken, K. Shibata, T. Nagai, A. J. Mannucci, et al. Space plasma physics: A review. *IEEE Transactions on Plasma Science*, 51 (7):1595–1655, 2023. doi: 10.1109/TPS.2022.3208906.

[66] University of Colorado Boulder and Space Weather Technology, Research, and Education Center. SWx TREC space weather data portal. Laboratory for Atmospheric and Space Physics, 2019. URL https://lasp.colorado.edu/space-weather-portal/. Accessed: 2026-01-15.

[67] University of Oulu. International GLE database. https://gle.oulu.fi/.

[68] R. S. Witte and J. S. Witte. *Statistics*. Wiley, 11th edition, 2017. ISBN 978-1-119-38605-6.

[69] World Data Center for Geomagnetism, Kyoto, M. Nose, T. Iyemori, M. Sugiura, T. Kamei, A. Matsuoka, S. Imajo, and T. Kotani. Geomagnetic Dst index, 2015. URL https://doi.org/10.17593/14515-74000.

[70] World Meteorological Organization. Instrument: SEISS/MPS, 2021. URL https://space.oscar.wmo.int/instruments/view/seiss_mps. OSCAR – Observing Systems Capability Analysis and Review Tool. Last updated: 2021-11-10.

[71] G. L. Wrenn, D. J. Rodgers, and K. A. Ryden. A solar cycle of spacecraft anomalies due to internal charging. *Annales Geophysicae*, 20(7):953–956, 2002.

A | Appendix A

A.1. GCR maps from WASAVIES and AniMAIRE

In this Section the results for 30, 56 and 94 km for AniMAIRE in GCR mode and WASAVIES are displayed for comparison as a complementary study for Section 3.1.1. The color scales used in the Figures are similar to ease the comparison and it can be concluded that both models throw comparable results up to 30 km, while the higher the altitude, the more AniMAIRE underestimates the dose rates, so it shall not be used at those high altitudes.

A.1.1. 30 km of altitude

At 30 km of altitude, both models reach similar ranges of effective dose rates values at similar ranges of latitudes. AniMAIRE seems to underestimate the values of the dose rates in relation to the latitude, with the same value bands a bit displaced towards higher latitudes in relation with WASAVIES. Orders of magnitude can be considered to be respected, even if the WASAVIES approach is more conservative.

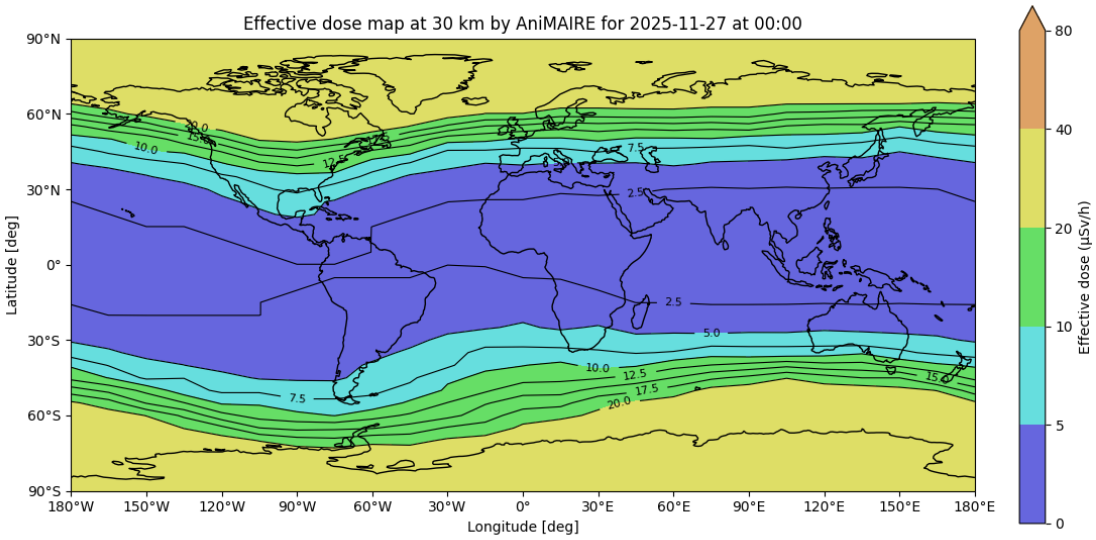

Figure A.1: Effective radiation dose at 30 km from AniMAIRE model

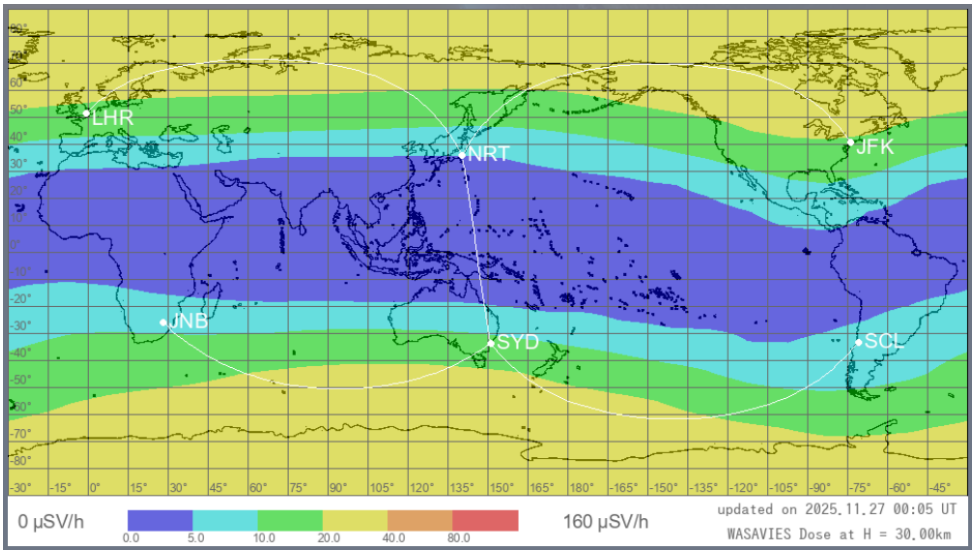

Figure A.2: Effective radiation dose at 30 km from WASAVIES model. Source: WASAVIES, NICT [47].

A.1.2. 56 km of altitude

At 50 km of altitude, differences are bigger between both models, with very similar results in AniMAIRE, while in WASAVIES, the lowest values of effective dose rates are confined in a equatorial reduced zone, higher values located at lower latitudes in comparison with 30 km and maximum values reaching the next range of values in the color scale with respect

to the 30 km map. AniMAIRE clearly cannot reproduce the dose rates distribution in comparison to WASAVIES and should be avoided to be used at such high altitudes.

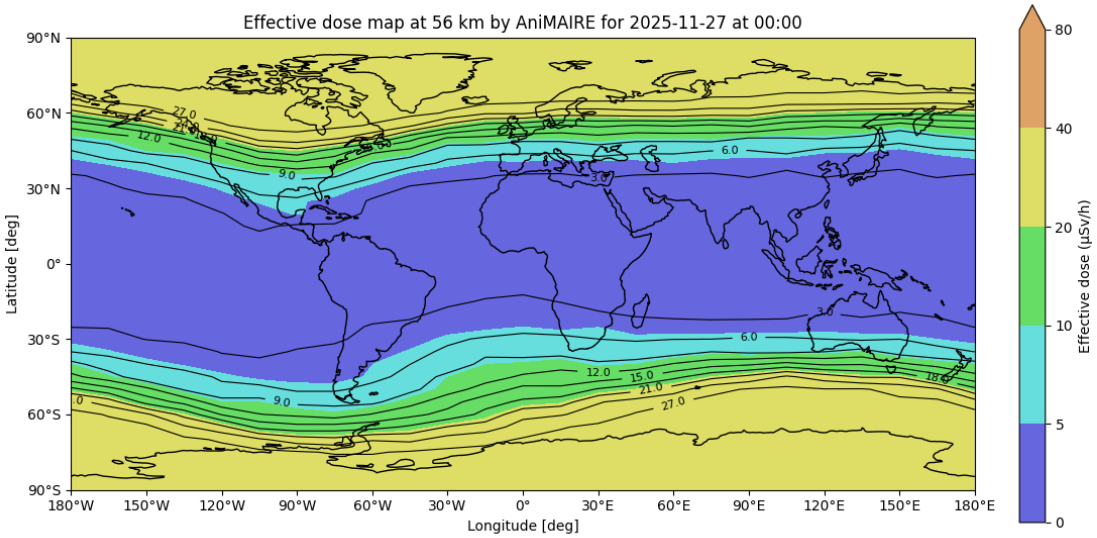

Figure A.3: Effective radiation dose at 56 km from AniMAIRE model

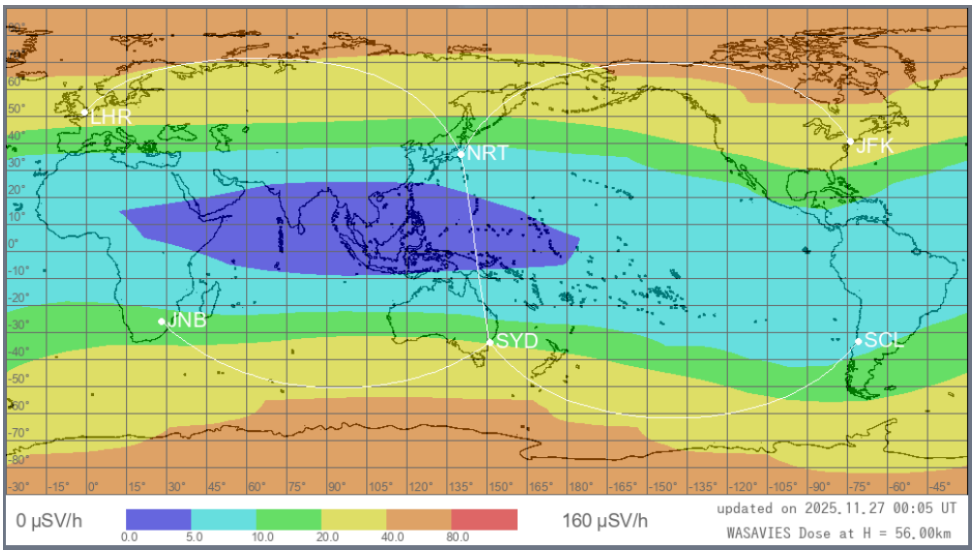

Figure A.4: Effective radiation dose at 56 km from WASAVIES model. Source: WASAVIES, NICT [47].

A.1.3. 94 km of altitude

At 94 km, maximum altitude offered by WASAVIES, AniMAIRE keeps displaying similar results to the previous ones, while the WASAVIES effective dose rate bands are displaced

to lower latitudes. This confirms the bad behavior of AniMAIRE at very high altitudes, which is far from its validity limits.

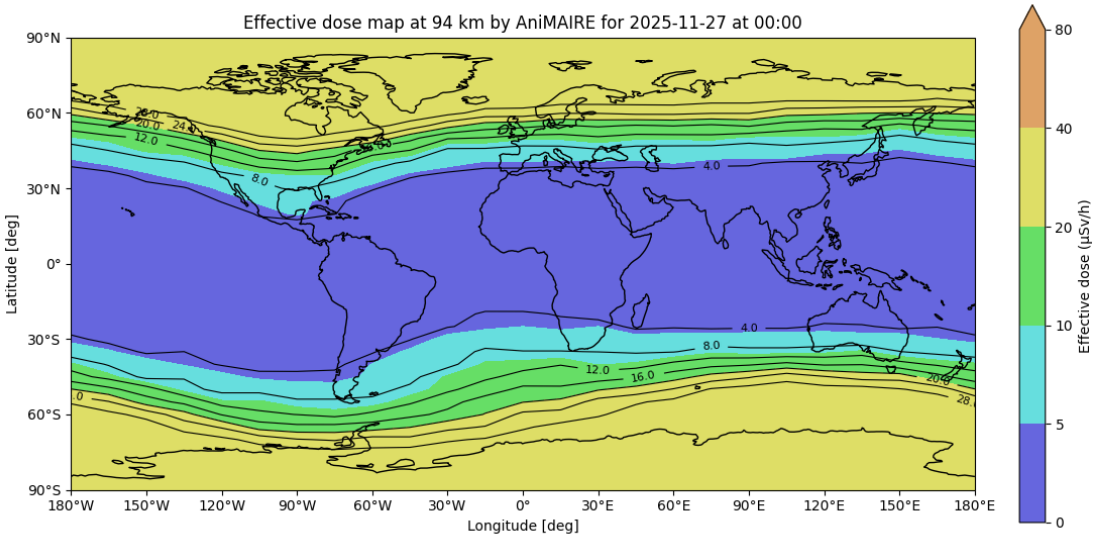

Figure A.5: Effective radiation dose at 94 km from AniMAIRE model

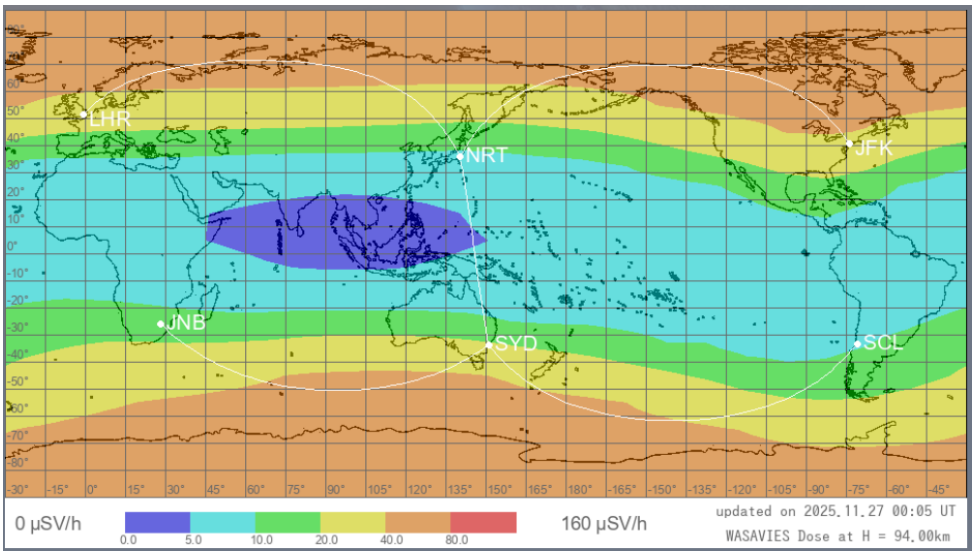

Figure A.6: Effective radiation dose at 94 km from WASAVIES model. Source: WASAVIES, NICT [47].

A.2. Figures from GLE detection studies

Figures showing the GLE detection results for GLEs 72, 73, 74, 75 and 76 are displayed in this Section as a complement for Section 3.1.2, where results are summarized and

commented. The figures show the number of stations in alert by using the GLE Alert+ algorithm in two different versions (Long Previous Time, LPT, and Real-Time, RT) at the upper part of each graph and the GOES proton fluxes of >10, >50, >100 and >500 MeV a the lower part. The algorithm detects a GLE event when 3 or more stations are in alert mode simultaneously. In all the cases the GOES >100 MeV proton flux overcomes the 1 pfu threshold condition for GLE events. The behavior of the other fluxes also depends on the event, with >10 and >50 MeV fluxes varying between different orders of magnitude, while >500 MeV flux does not reach enough significant values in order to define a threshold.

GLE 72 is not able to be detected by the RT version of GLE Alert+, without enough stations in alert, while the LPT version would start detecting the event too soon, due to prior strong activity, even if the start of the event can be clearly distinguished as a great increase in the number of stations in alert. After the detection, the LPT could track the duration of the GLE event, until no stations were still in alert mode.

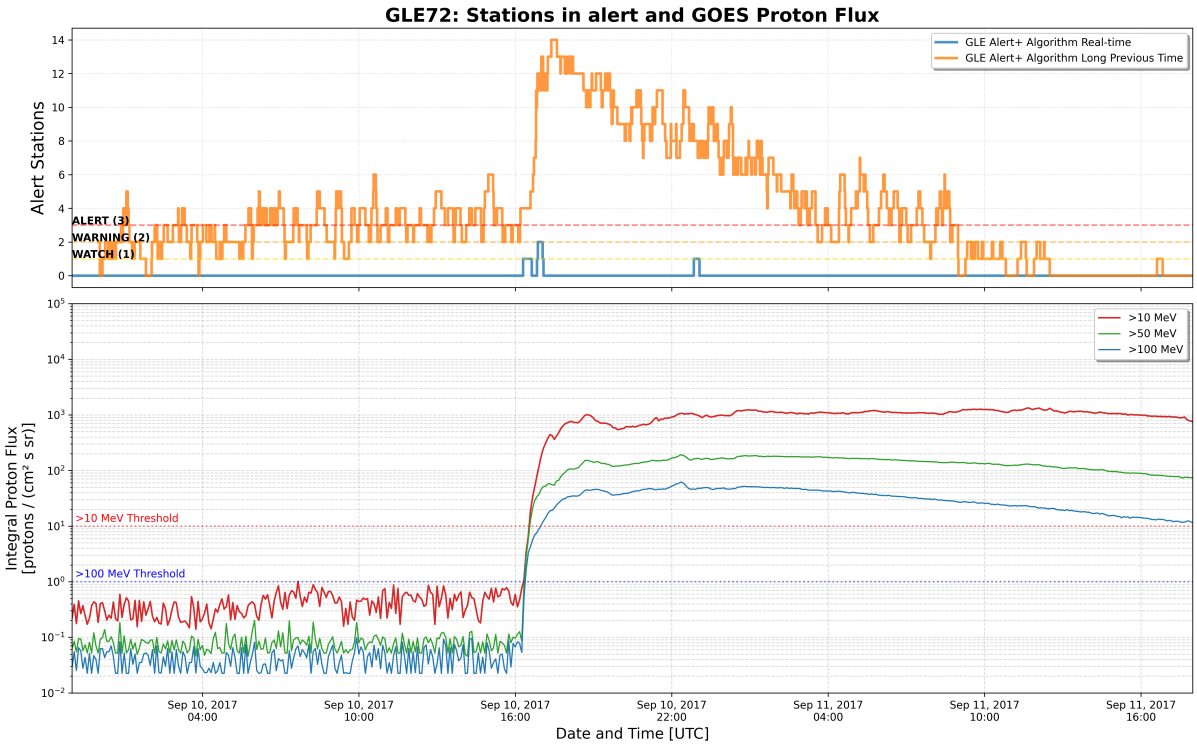

Figure A.7: GLE detection and GOES proton flux during GLE 72

GLE 73 could be detected with the RT algorithm, with exactly the three stations in alert needed for the event detection, and also by the LPT version, with a wider range of stations in alert, that also kept the alert during the following day.

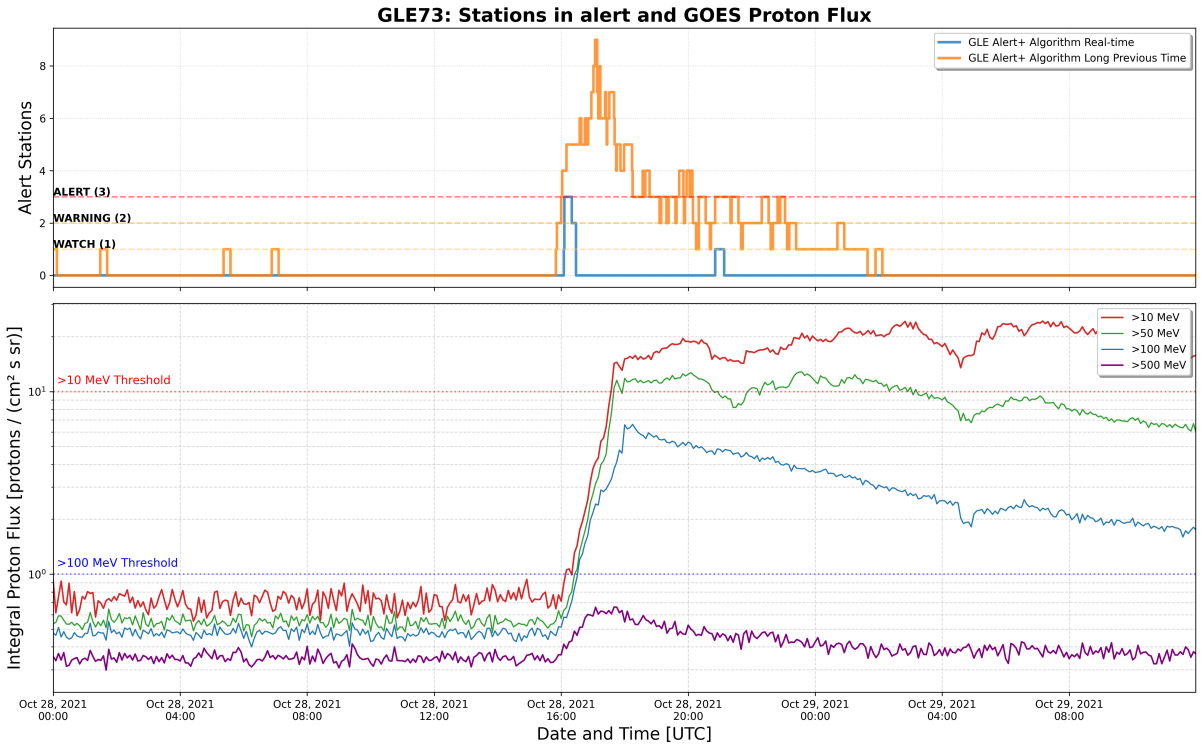

Figure A.8: GLE detection and GOES proton flux during GLE 73

GLE 74 could also be detected by RT with the minimum required number of stations in alert, while LPT failed to catch any alert. This is due to the Forbush decrease event that preceded the GLE, causing the previous levels of neutron counts higher than the counts during the event. In presence of a Forbush decrease, therefore, the GLE might be detected by RT, but its evolution would be missed by LPT.

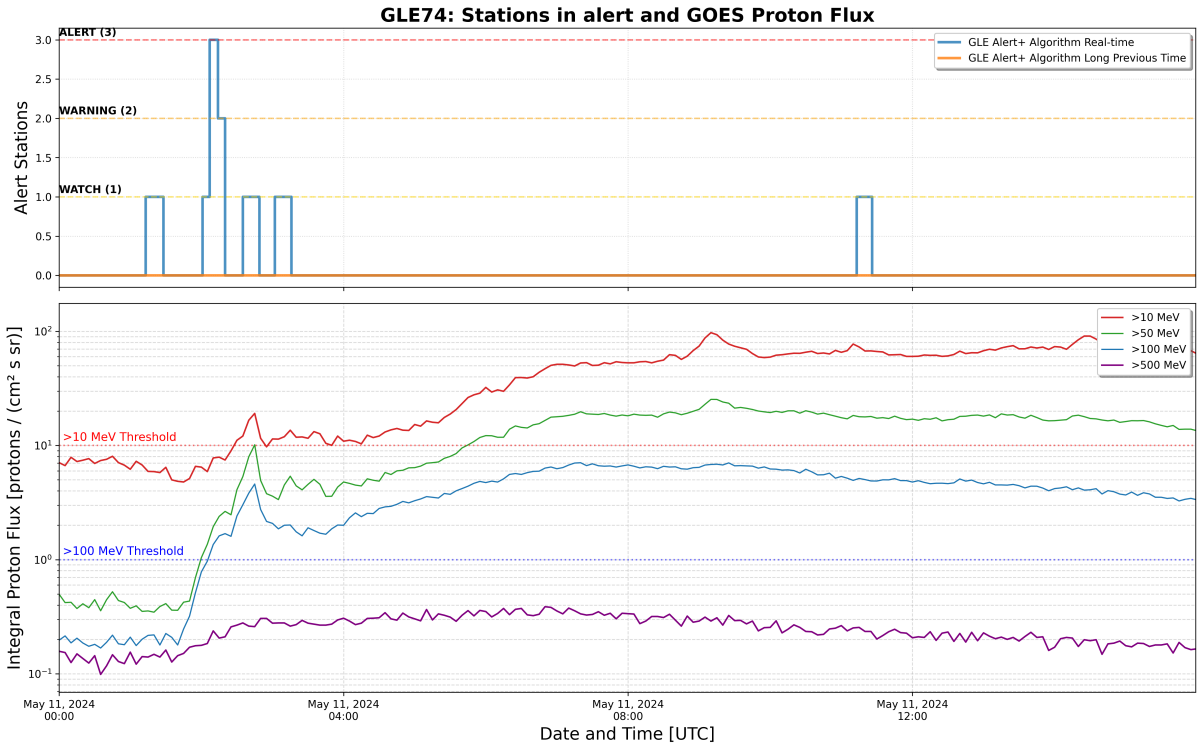

Figure A.9: GLE detection and GOES proton flux during GLE 74

GLEs 75 and 76 were not caught by any of the algorithm versions, not reaching in any case the minimum required number of three stations in alert. This implies a lower increase in neutron count rates in the net of stations, characterizing both events as weaker GLEs.

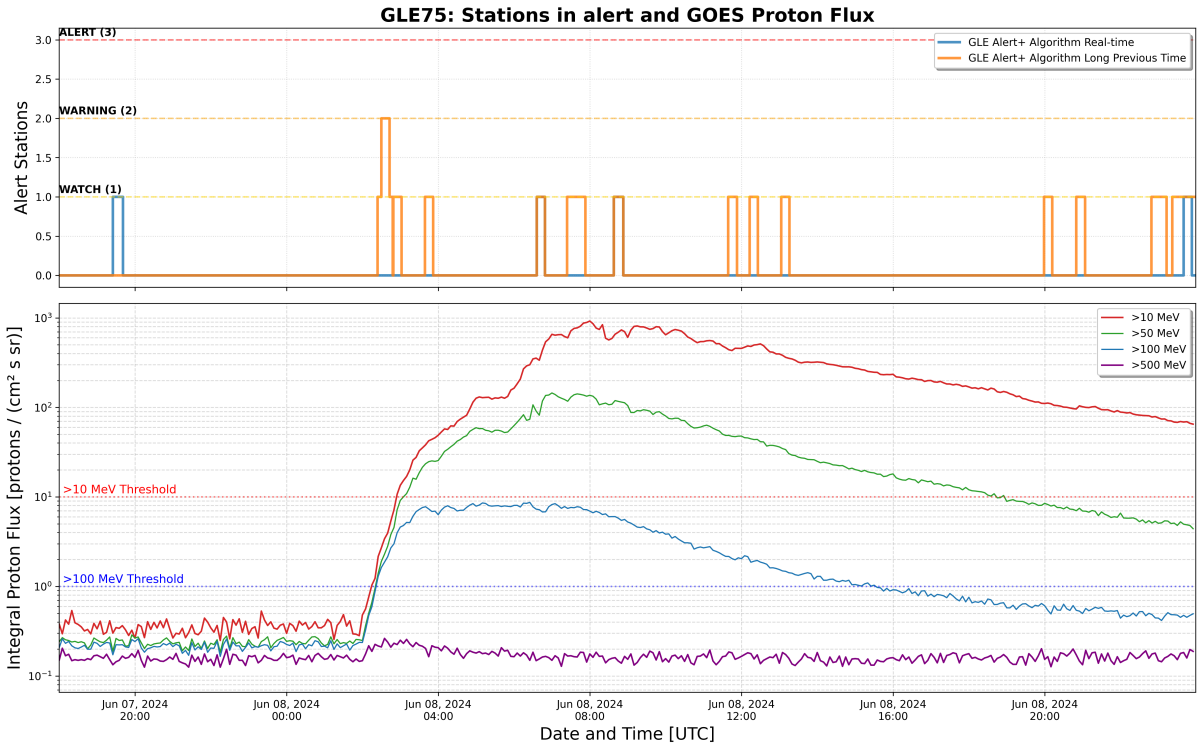

Figure A.10: GLE detection and GOES proton flux during GLE 75

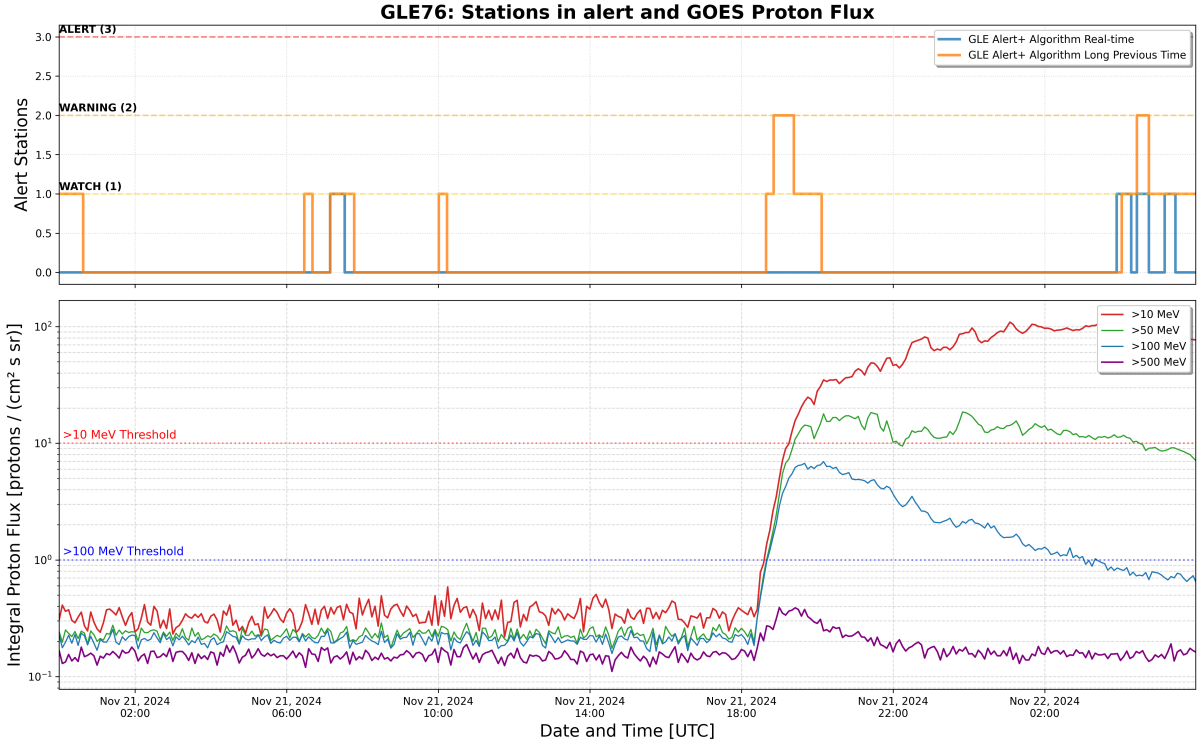

Figure A.11: GLE detection and GOES proton flux during GLE 76

A.3. Figures from Radiation Dose studies

In this section, figures corresponding to the maximum effective radiation dose rates at 11, 15 and 20 km computed by AniMAIRE for GLE (with different combinations of stations), AniMAIRE for GCR, NAIRAS and the Statistical Model based in CRAC:DOMO (only for 11 km of altitude) are collected. These figures are complementary to the study in Section 3.1.3 and the results are commented and summarized in such section.

A.3.1. GLE 73

Figures representing maximum effective radiation dose rates during GLE 73 computed through different models are displayed in this appendix. GLE 73 took place on 2021-10-28. No data at 20 km is offered for this GLE from NAIRAS.

At 11 km, no model reaches alert levels, except for the statistical model which reaches an extremely high peak and lower peaks over the FAA alert. The other levels stay at similar values of dose rates.

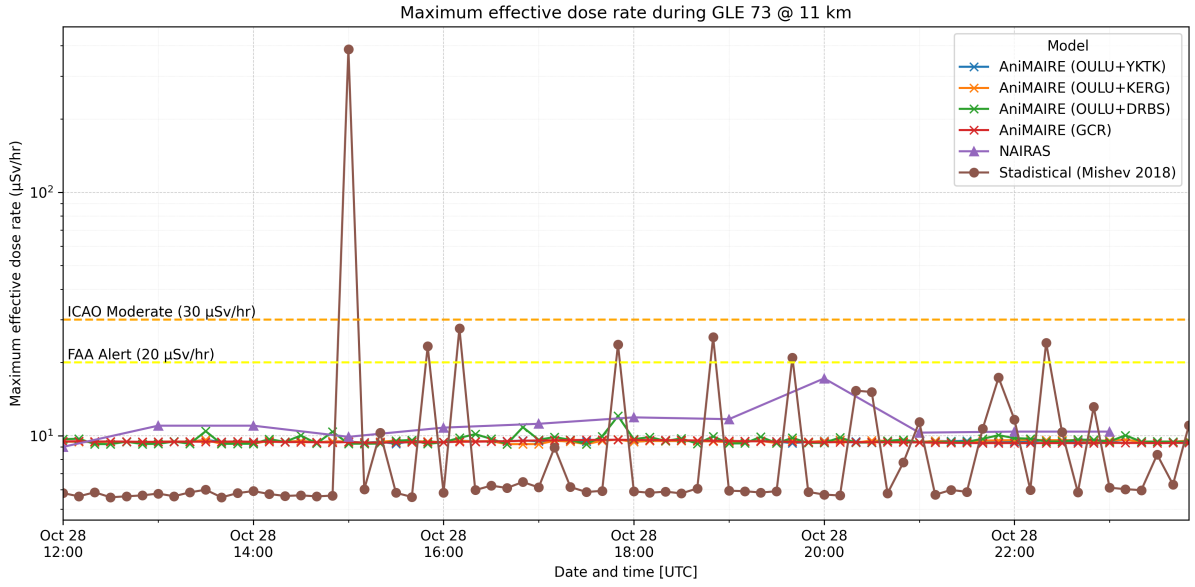

Figure A.12: GLE results comparison at 11 km for various models during GLE 73

At 15 km, OULU+DRBS and NAIRAS reach the 20 $\mu Sv/h$ threshold, with the first one overcoming that value during the whole GLE and the latter only at one specific hour. The other combinations of stations and GCR mode remains close to that threshold but do not cross it.

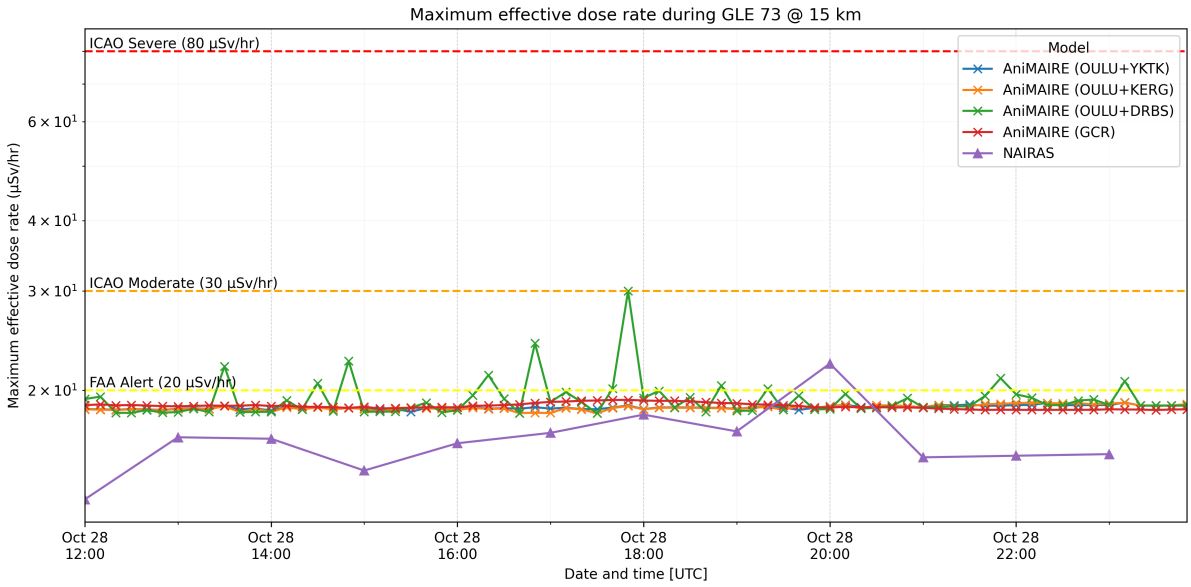

Figure A.13: GLE results comparison at 15 km for various models during GLE 73

A.3.2. GLE 74

Figures representing maximum effective radiation dose rates during GLE 74 computed through different models are displayed in this appendix. GLE 74 took place on 2024-05-11.

This GLE was preceded by a Forbush decrease, so the neutron count rate increases can be negative at some points, as the neutron counts previous to the Forbush decrease were bigger than the ones caused by the GLE. This produces the inverse peaks shown by the results of AniMAIRE in GLE mode.

At 11 km, the rates remain under alert levels for all the models and they reach similar values.

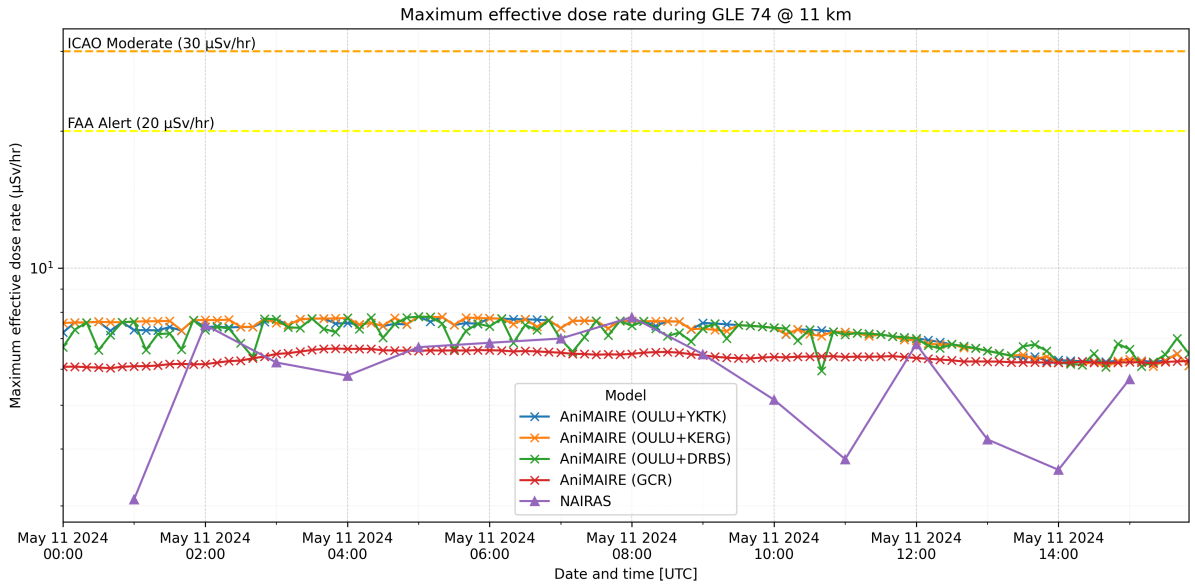

Figure A.14: GLE results comparison at 11 km for various models during GLE 74

At 15 km, no alert levels are reached. The three combinations of stations in GLE mode share the same baseline, with OULU+DRBS catching lower peaks. GCR mode values remain a bit lower than the GLE mode results.

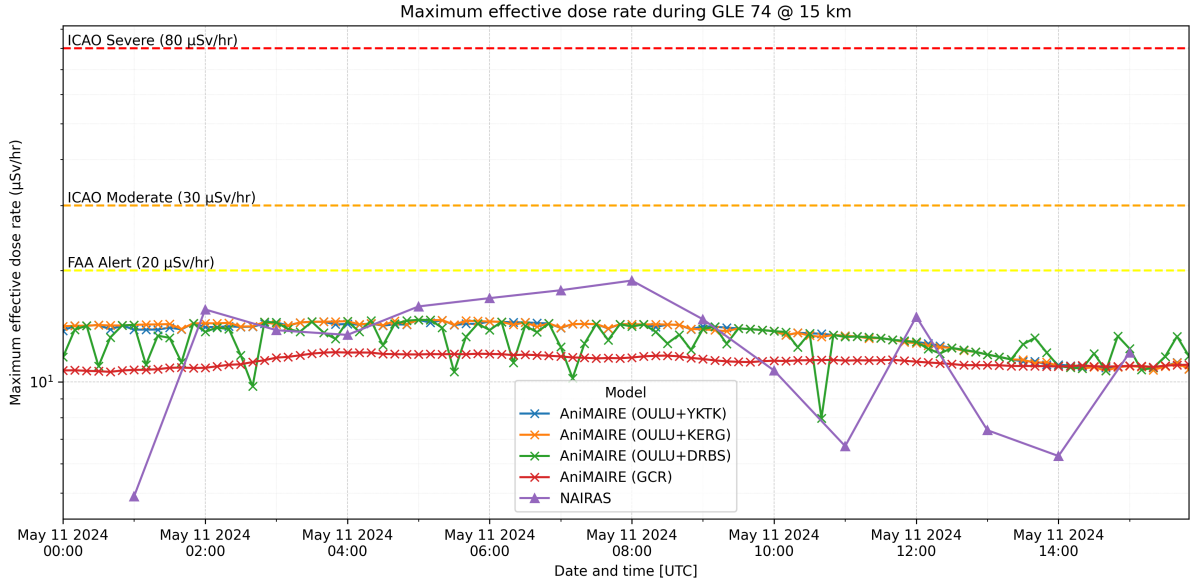

Figure A.15: GLE results comparison at 15 km for various models during GLE 74

At 20 km, NAIRAS overcomes the 30 $\mu Sv/h$ threshold during most of the GLE duration, while the GLE mode results remain over the 20 $\mu Sv/h$ level. The OULU+DRBS combination shows very low punctual peaks and GCR mode remains under alert levels.

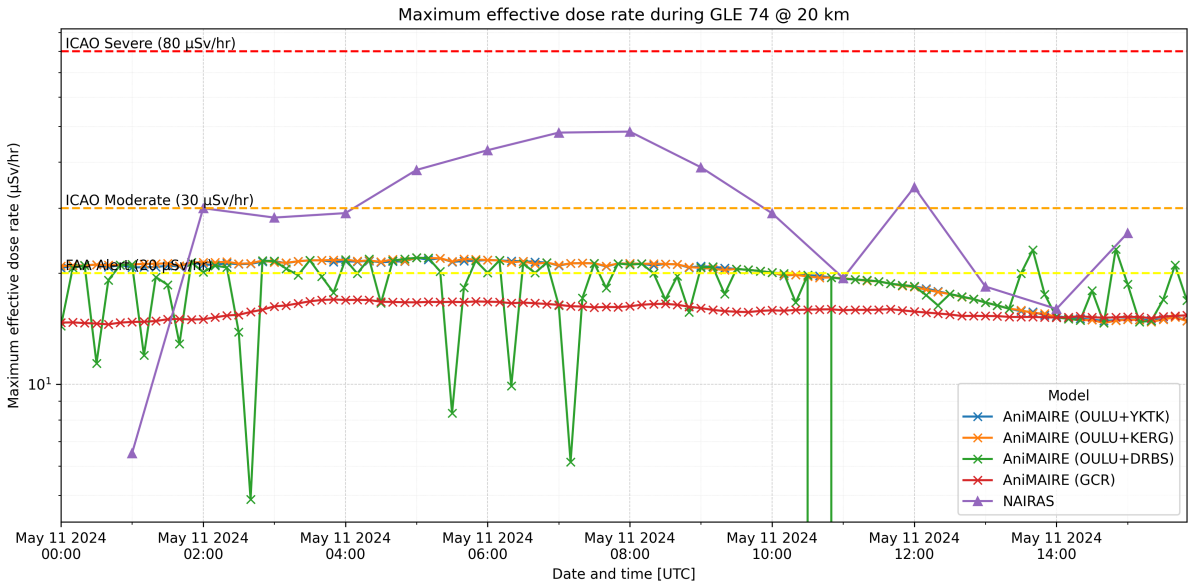

Figure A.16: GLE results comparison at 20 km for various models during GLE 74

A.3.3. GLE 75

Figures representing maximum effective radiation dose rates during GLE 75 computed through different models are displayed in this appendix. GLE 75 took place on 2024-06-08.

At 11 km, any model reaches alert levels. The maximum reached by NAIRAS and GLE mode is similar, and the statistical model remains a bit lower, betwen GLE and GCR mode results.

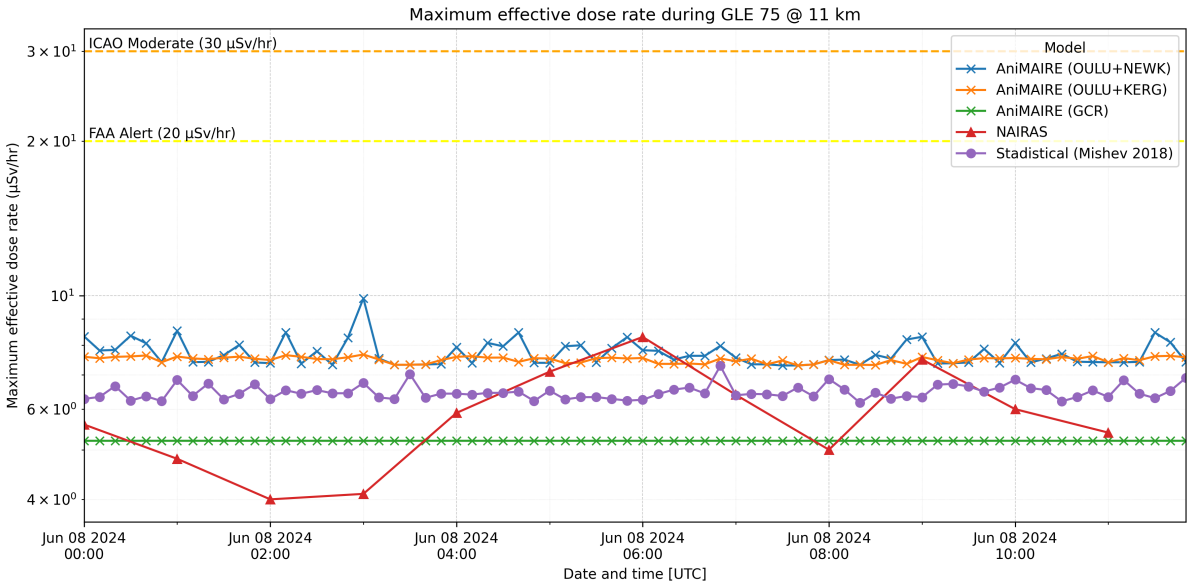

Figure A.17: GLE results comparison at 11 km for various models during GLE 75

At 15 km, GLE mode with OULU+NEWK stations punctually reaches the 20 $\mu Sv/h$ alert, but remains at lower levels during almost the whole GLE, while the other models do not reach any alert level. GCR mode underestimates the values with relation to the GLE mode valus.

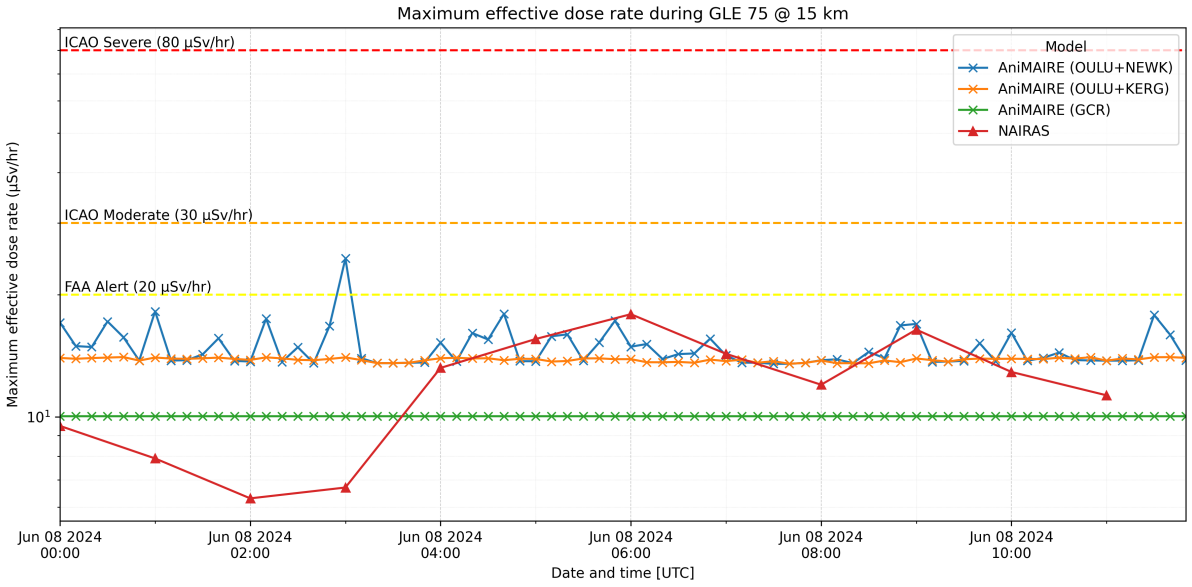

Figure A.18: GLE results comparison at 15 km for various models during GLE 75

A.3.4. GLE 76

Figures representing maximum effective radiation dose rates during GLE 76 computed through different models are displayed in this appendix. GLE 76 took place on 2024-11-21.

At 11 km, no model overcomes any alert level. NAIRAS model remains at similar values as GCR mode.

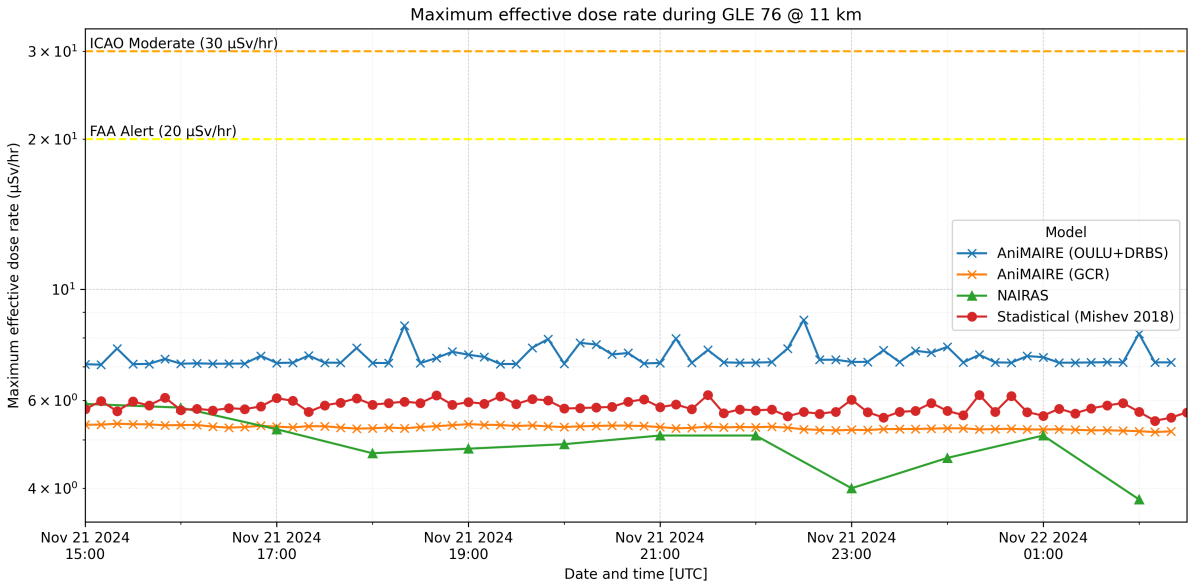

Figure A.19: GLE results comparison at 11 km for various models during GLE 76

At 15 km, OULU+DRBS punctually reaches the 20 $\mu Sv/h$ levels but NAIRAS stays at lower levels than GCR mode.

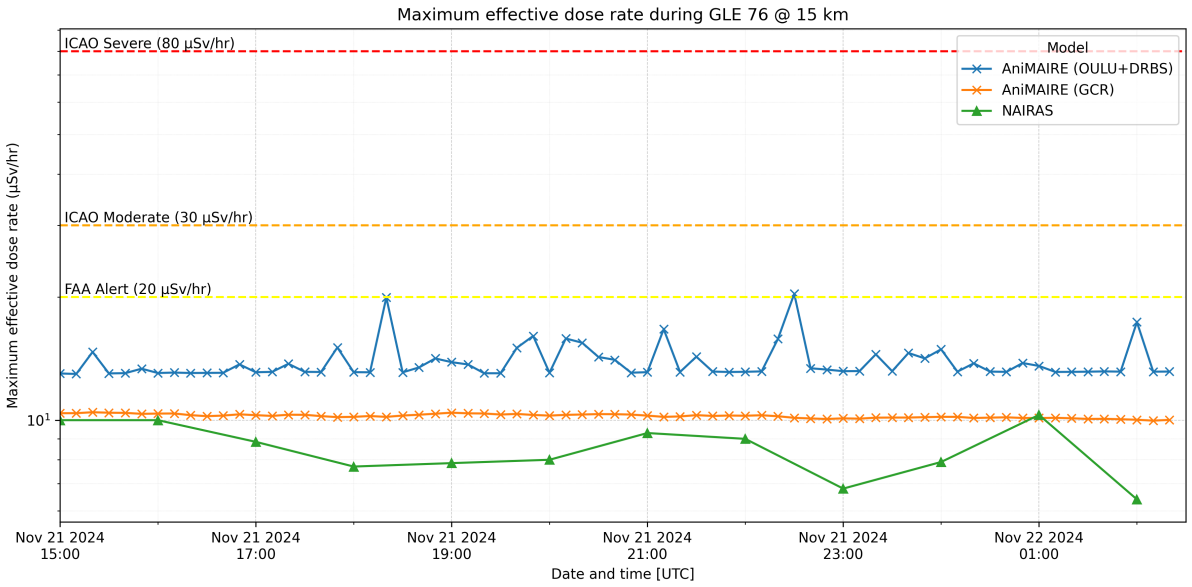

Figure A.20: GLE results comparison at 15 km for various models during GLE 76

At 20 km, OULU+DRBS reach higher levels, unleashing ICAO moderate alerts, while NAIRAS only overcomes the FAA alert and GCR mode remains lower than any alert level.

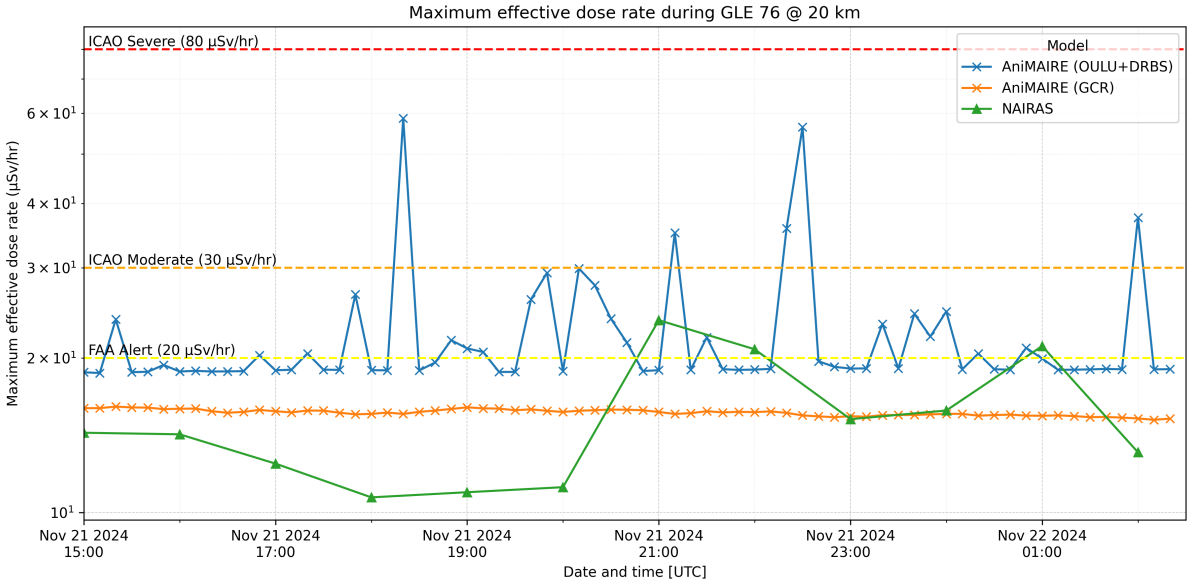

Figure A.21: GLE results comparison at 20 km for various models during GLE 76

A.3.5. GLE 77

Figures representing maximum effective radiation dose rates during GLE 77 computed by different models are displayed in this appendix. GLE 77 took place on 2025-11-11.

At 15 km, OULU+DRBS reaches a ICAO severe alert a the beginning of the GLE, remaining then between ICAO moderate and FAA alert levels. GCR mode does not catch any alert, while NAIRAS reaches alert levels later than GLE mode, with high dose rates values, close to but not fully reaching the ICAO severe alert.

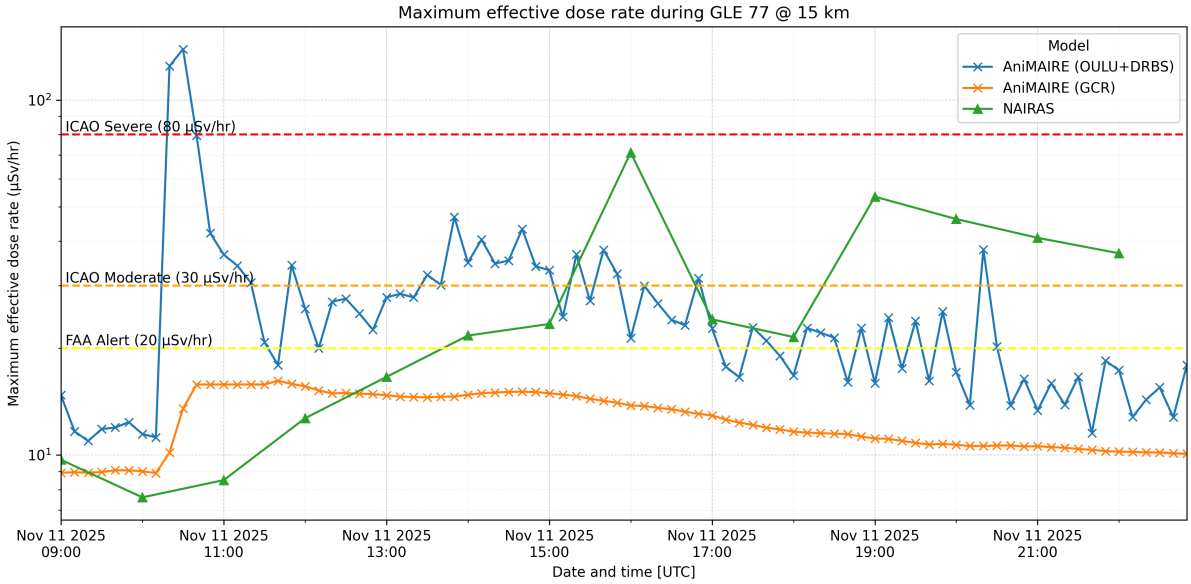

Figure A.22: GLE results comparison at 15 km for various models during GLE 77

At 20 km, OULU+DRBS has a similar shape as for 15 km, reaching even higher values, overcoming the ICAO severe alert during long periods. NAIRAS also reaches that threshold, reaching severe values but starting later than GLE mode. Meanwhile, GCR mode reaches the FAA alert threshold, but remains very low in comparison with the previous models.

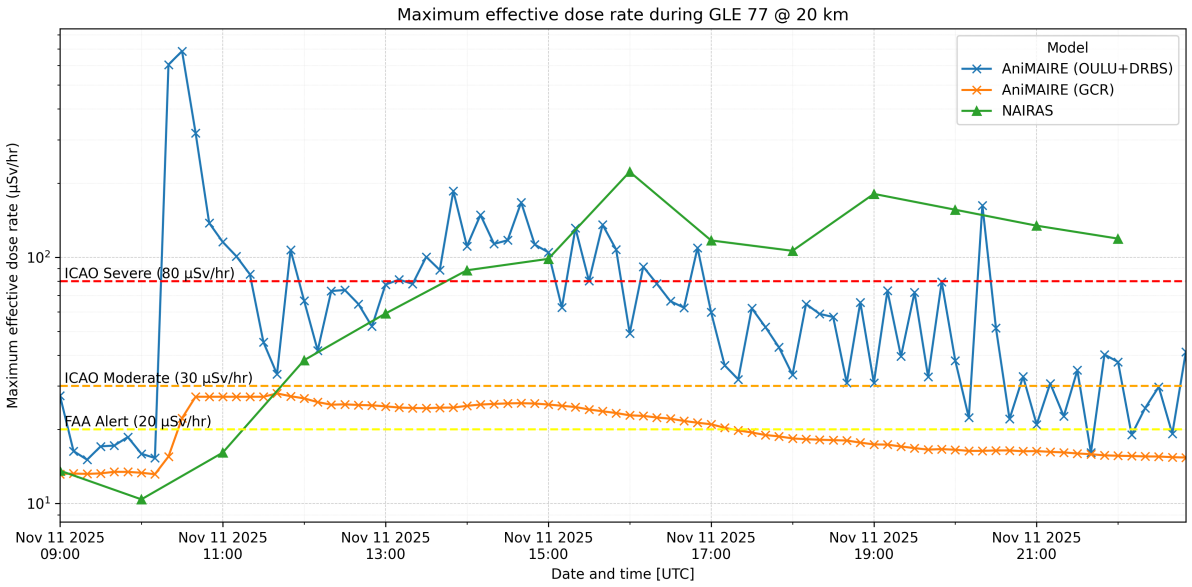

Figure A.23: GLE results comparison at 20 km for various models during GLE 77

A.4. Very energetic solar particle events without GLE

The following figures represent examples of very energetic solar particle events in which the threshold of 1 pfu was exceeded by the >100 MeV integral proton flux but there was no subsequent GLE event (according to the official GLE database in [67]). This shows that the mentioned threshold is only suitable as a necessary condition for GLE events, but not sufficient, as the neutron count rates on ground must also experiment an increase. Those cases show events where very energetic particles were detected but, likely due to the storms' characteristics, they did not unchained energetic enough secondary particle showers to produce a considerable radiation environment enhancement in the atmosphere.

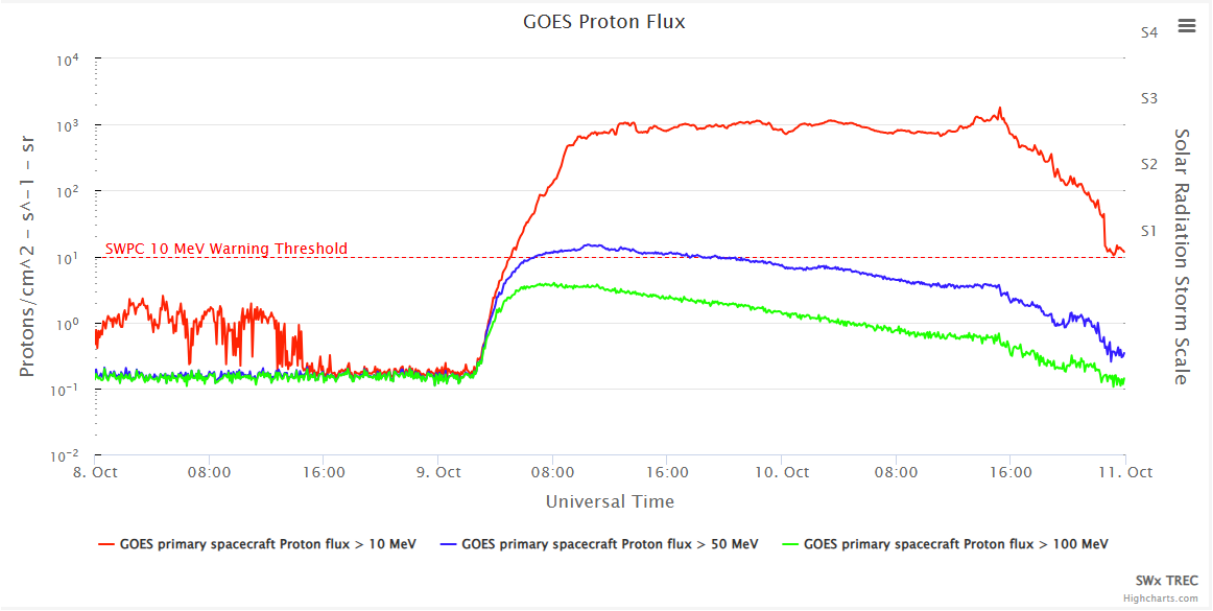

Figure A.24: GOES proton flux during 2024/10/09. Source: [66].

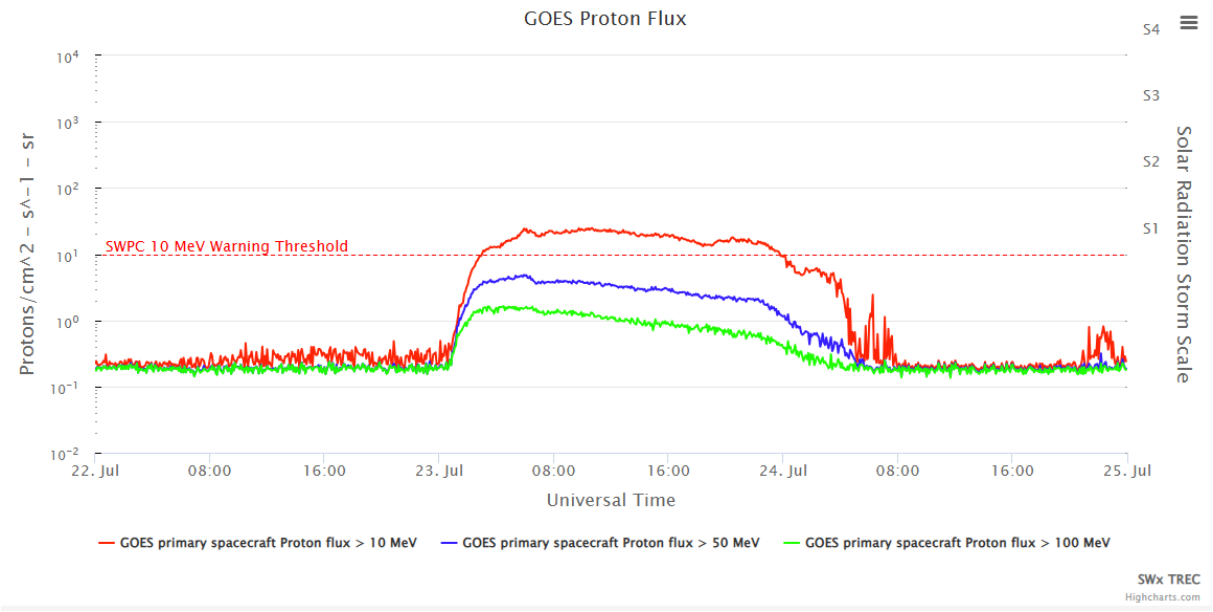

Figure A.25: GOES proton flux during 2024/07/23. Source: [66].

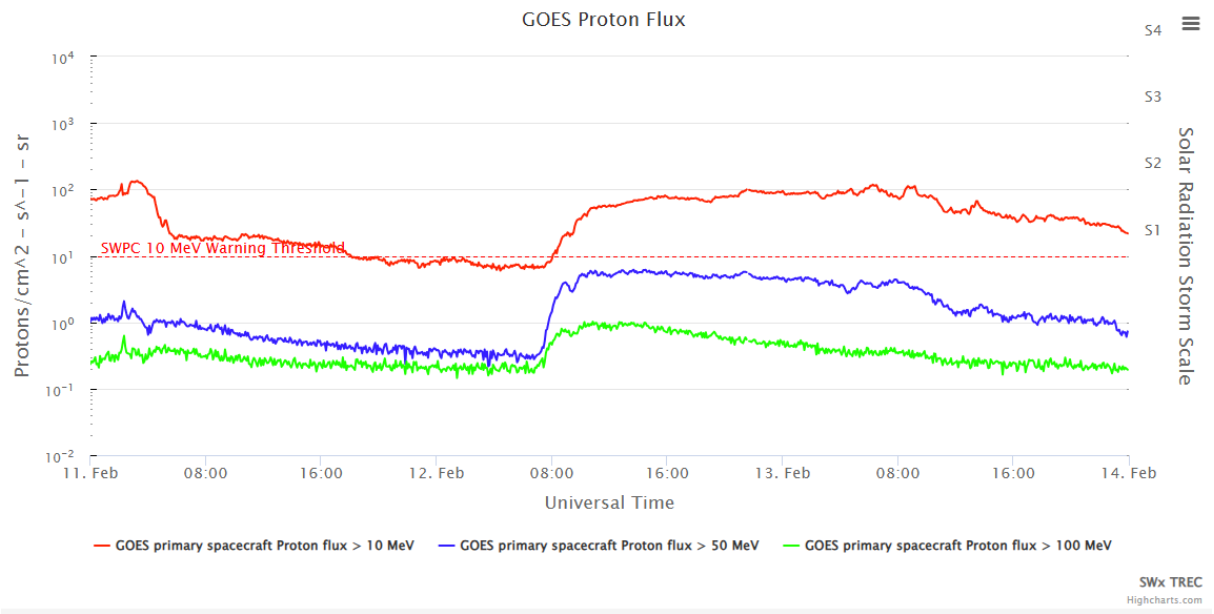

Figure A.26: GOES proton flux during 2024/02/12. Source: [66].

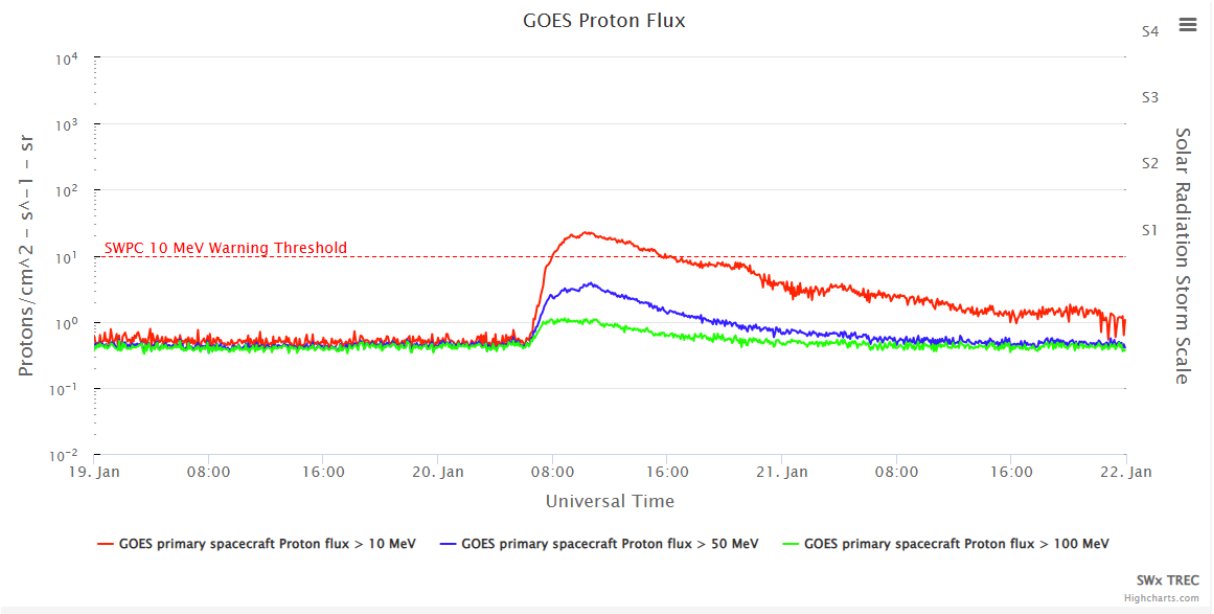

Figure A.27: GOES proton flux during 2022/01/21. Source: [66].

A.5. Low energy differential electron fluxes from GOES 19

The figures collected in this Appendix show the differential electron fluxes for different energies (11.3, 18.2 and 30.0 keV, one per subplot) and angular views (12 zones, all of

them presented in each subplot) from GOES 19 data. From the angular views, only 10 of them are independent, with zones 6 and 7 having two channels.

The figures show that some of the angular views are dominant in order of magnitude, which indicates that the electron populations are located mainly in an angular direction. Furthermore, there are data gaps when most of the angular zones do not detect particles and over the period most of the less populated angular zones perceive a very low flux. Moreover, the lower the energy, the higher values the flux reaches, which indicates a bigger population of lower energy electrons.

The fluxes show a periodical variation with peaks between local midnight and 6 AM at Local Solar Time, with the missing peaks corresponding to missing data. In Figure A.28, the quiet time of 1-7 January 2026 is represented with all the peaks of available data having a similar height and width, while in Figure A.29, with solar storm time during 12-13 November 2025, where peaks can be seen to be wider.

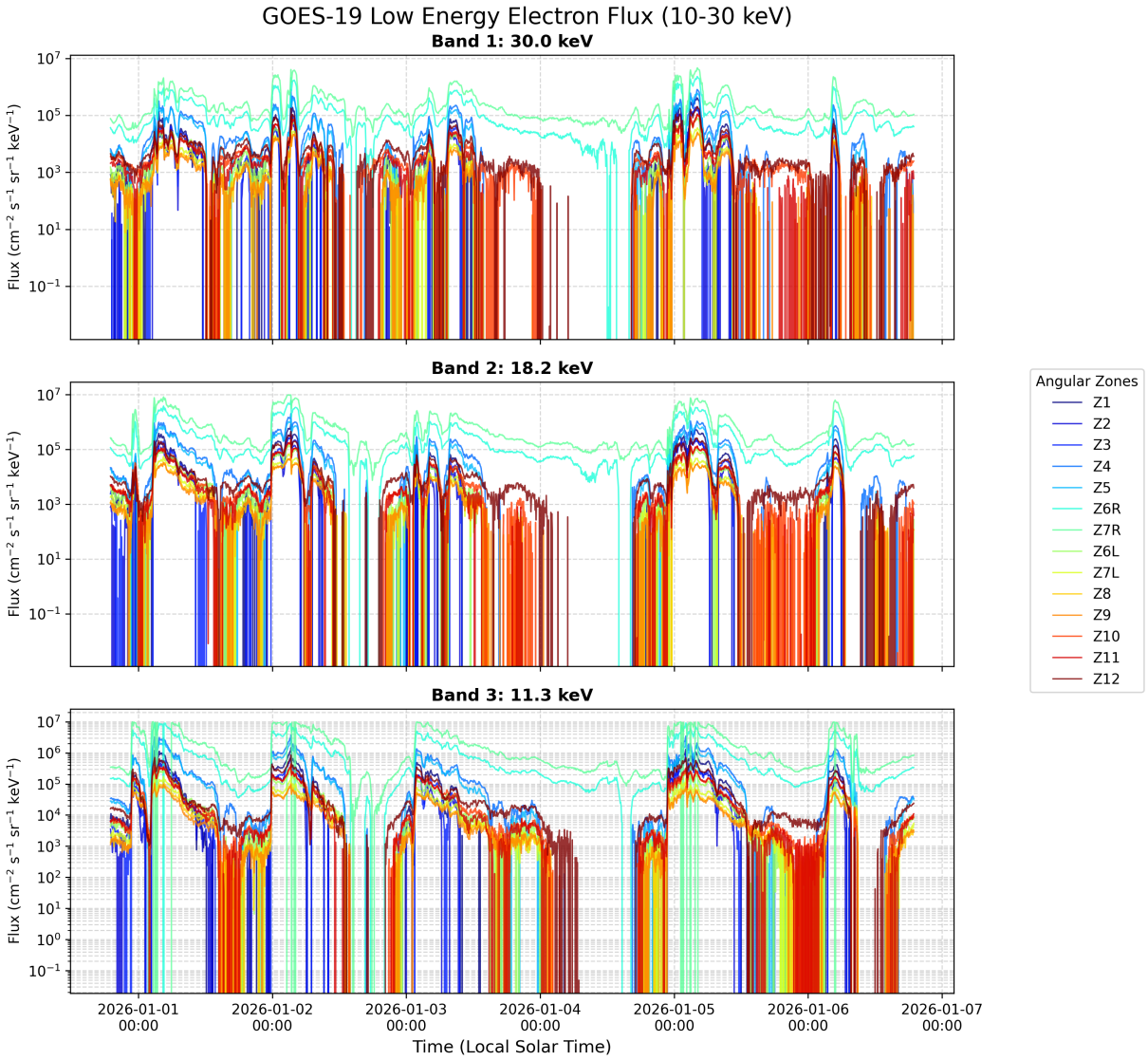

Figure A.28: Differential electron fluxes from GOES 19/SEISS/MPS-LO instruments during January 2026 (quiet time).

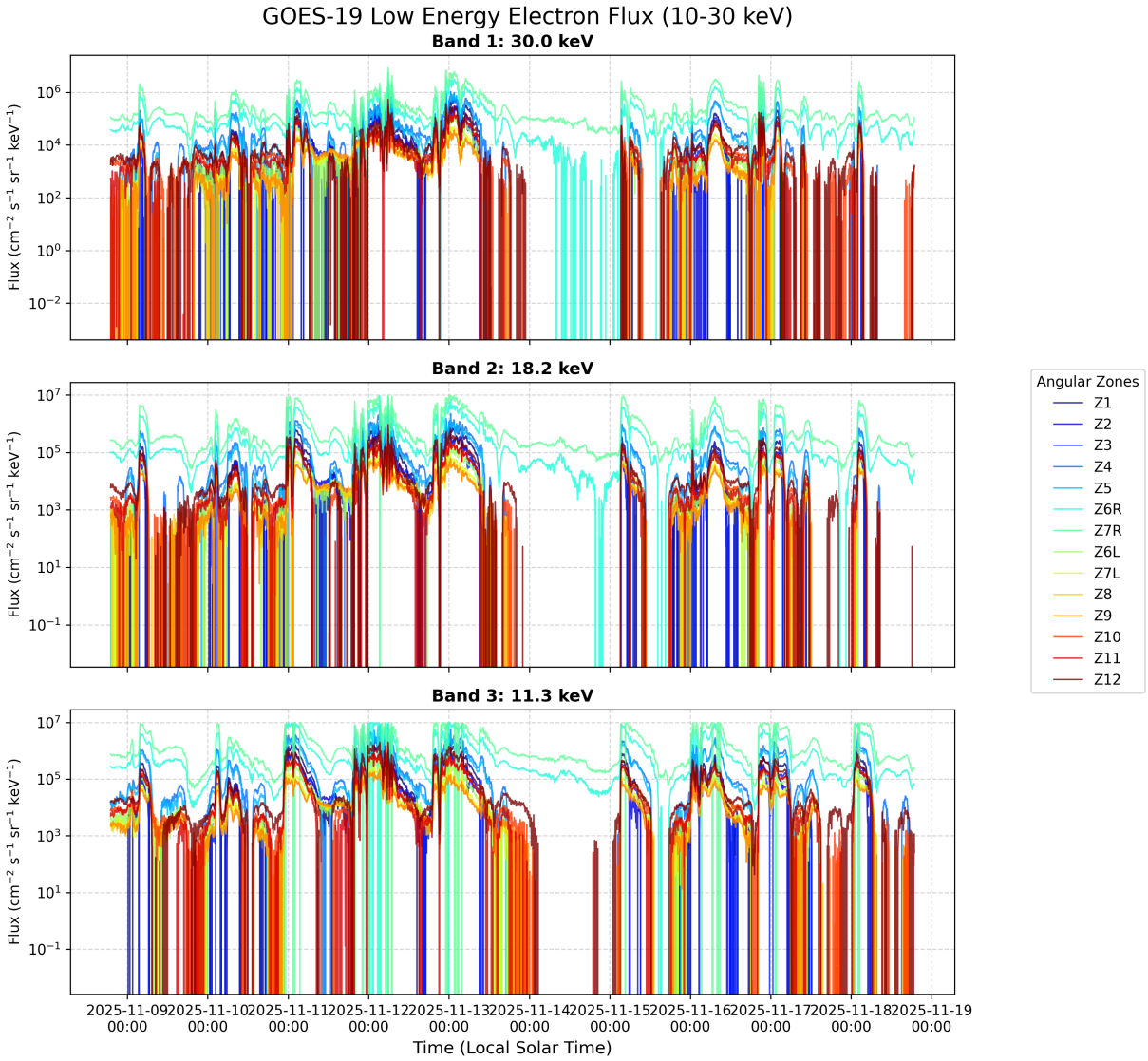

Figure A.29: Differential electron fluxes from GOES 19/SEISS/MPS-LO instruments during November 2025 (solar storm during 12-13).

A.6. Kp values for solar storm periods

Figures corresponding to the Kp index during the solar storms of November 2025 and January 2026 are represented in this section. The enhanced values of Kp can be clearly seen corresponding to the solar storms of 12-13 November 2025 and 19-21 January 2026.

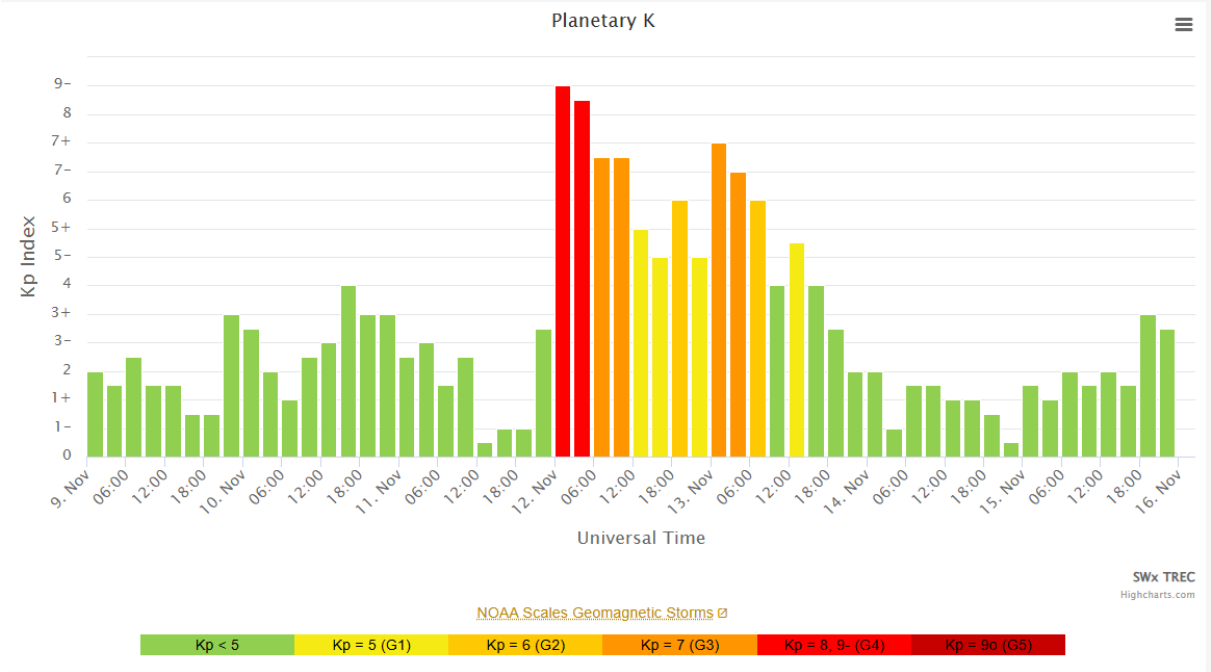

Figure A.30: Planetary K index during 9 to 16 November 2025. Source: [66].

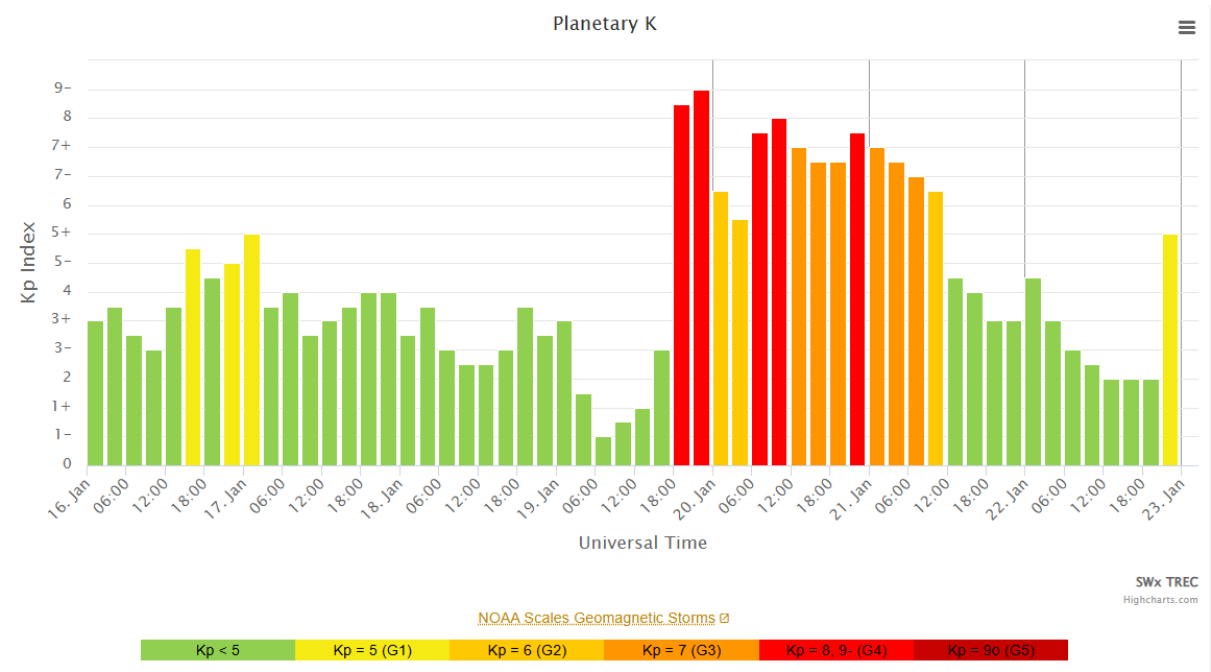

Figure A.31: Planetary K index during 16 to 23 January 2026. Source: [66].

List of Figures

2.1 Solar cycle progression from Solar Cycle 1 to Solar Cycle 25 (until February 2026). Source: NOAA Space Weather Prediction Center (https://www.swpc.noaa.gov/products/solar-cycle-progression). 4
2.2 Structure of Earth's magnetosphere. Reproduced from [65] without changes, licensed under CC BY 4.0 (https://creativecommons.org/licenses/by/4.0/). 6
2.3 Relationships between space weather events and impacts. 8
2.4 Neutron count rates during GLE 74 (2024/05/11) and GLE 77 (2025/11/11). Source: International GLE database ([67]). 12
2.5 Earth radiation belts (electron content) and different orbit locations. Source: Reproduced from [24], with permission from the American Geophysical Union (https://www.agu.org/publications/authors/policies). 23
2.6 Kp values by GFZ during the solar storm of January 2026. Source: [22]. . 27
2.7 K9 limits for different geomagnetic stations according to their corrected geomagnetic latitude. 28
2.8 Geomagnetic data from San Pablo observatory (Toledo, Spain) from 18 to 22 January 2026. Source: INTERMAGNET [27]. 30
2.9 Stations belonging to INTERMAGNET. Red dots denote open stations, while grey dots denote closed ones. Source: INTERMAGNET [27]. 31

3.1 Scheme of the developed tool for continuous operation (nowcast) 34
3.2 Effective radiation dose at 20 km from NAIRAS model 36
3.3 Effective radiation dose at 18 km from WASAVIES model. Source: WASAVIES, NICT [47]. 37
3.4 Effective radiation dose at 20 km from AniMAIRE model 37
3.5 GLE detection and GOES proton flux during GLE 77 40
3.6 GLE results comparison at 20 km for various models during GLE 75 44
3.7 GLE results comparison at 11 km for various models during GLE 77 45
3.8 Effective dose rate map for GCR at 11 km on 2025/12/12 49
3.9 Effective dose rate map for GCR at 20 km on 2025/12/12 49

3.10 Effective dose rate map during GLE 77 (2025/11/11) at 20 km 50
3.11 D-Index map during GLE 77 (2025/11/11) at 20 km 50

4.1 Integral electron flux (>2 MeV) in GEO (Local Solar Time) during 1 to 6 January 2026. 57
4.2 Integral electron flux (>2 MeV) in GEO (Local Solar Time) during 9 to 19 November 2025. 58
4.3 Electron fluence (>2 MeV) in GEO (Local Solar Time) during September to December 2025. 61
4.4 Low energy integral electron flux in GEO (Local Solar Time) from 1 to 6 January 2026. 64
4.5 Low energy integral electron flux in GEO (Local Solar Time) from 9 to 19 November 2025. 64
4.6 Scheme of the GEO charging risk tool. 66
4.7 Real time operation output for 2026/01/16 at 16:05 UTC. 68
4.8 Real time operation output for 2026/01/21 at 8:50 UTC. 69
4.9 Long term analysis output for internal charging risk based in flux during 14 to 19 January 2026. 70
4.10 Long term analysis output for internal charging risk based in fluence during 14 to 19 January 2026. 70
4.11 Long term analysis output for surface charging risk based in flux during 14 to 19 January 2026. 71

5.1 Selected geomagnetic observatories over the world map for the November 2025 study. 74
5.2 Comparison between local K indices in Spain from 18 to 22 January 2026. 75
5.3 Correlation metrics for geomagnetic observatories around the globe for distances along geographical longitude and latitude. Left: Pearson correlation coefficient. Right: Percentage of same K values. 77
5.4 Correlation metrics for geomagnetic observatories around the globe by difference in magnetic coordinates. Left: Percentage of differences greater than 2 units of K. Right: Percentage of differences greater than 3 units of K. 77
5.5 Scheme of the tool for geomagnetic disturbance risk assessment. 83
5.6 Local K index and G scale values output from the Closest Station Approach. 85
5.7 Local K index and G scale values output from the Averaging Stations Approach. 85
5.8 Specified location and used stations output for both the Closest Station Approach (left) and the Averaging Stations Approach (right). 86

A.1 Effective radiation dose at 30 km from AniMAIRE model 102
A.2 Effective radiation dose at 30 km from WASAVIES model. Source: WASAVIES, NICT [47]. 102
A.3 Effective radiation dose at 56 km from AniMAIRE model 103
A.4 Effective radiation dose at 56 km from WASAVIES model. Source: WASAVIES, NICT [47]. 103
A.5 Effective radiation dose at 94 km from AniMAIRE model 104
A.6 Effective radiation dose at 94 km from WASAVIES model. Source: WASAVIES, NICT [47]. 104
A.7 GLE detection and GOES proton flux during GLE 72 105
A.8 GLE detection and GOES proton flux during GLE 73 106
A.9 GLE detection and GOES proton flux during GLE 74 107
A.10 GLE detection and GOES proton flux during GLE 75 108
A.11 GLE detection and GOES proton flux during GLE 76 108
A.12 GLE results comparison at 11 km for various models during GLE 73 109
A.13 GLE results comparison at 15 km for various models during GLE 73 110
A.14 GLE results comparison at 11 km for various models during GLE 74 111
A.15 GLE results comparison at 15 km for various models during GLE 74 111
A.16 GLE results comparison at 20 km for various models during GLE 74 112
A.17 GLE results comparison at 11 km for various models during GLE 75 113
A.18 GLE results comparison at 15 km for various models during GLE 75 113
A.19 GLE results comparison at 11 km for various models during GLE 76 114
A.20 GLE results comparison at 15 km for various models during GLE 76 115
A.21 GLE results comparison at 20 km for various models during GLE 76 115
A.22 GLE results comparison at 15 km for various models during GLE 77 116
A.23 GLE results comparison at 20 km for various models during GLE 77 117
A.24 GOES proton flux during 2024/10/09. Source: [66]. 118
A.25 GOES proton flux during 2024/07/23. Source: [66]. 118
A.26 GOES proton flux during 2024/02/12. Source: [66]. 119
A.27 GOES proton flux during 2022/01/21. Source: [66]. 119
A.28 Differential electron fluxes from GOES 19/SEISS/MPS-LO instruments during January 2026 (quiet time). 121
A.29 Differential electron fluxes from GOES 19/SEISS/MPS-LO instruments during November 2025 (solar storm during 12-13). 122
A.30 Planetary K index during 9 to 16 November 2025. Source: [66]. 123
A.31 Planetary K index during 16 to 23 January 2026. Source: [66]. 123

List of Tables

2.1 NOAA Space Weather Scales (G, S, and R) from [48]. 9
2.2 Values of the Space Weather D-index from D0 to D5, their classification, and corresponding dose rate intervals (from [40]). 15
2.3 Internal charging risk criteria. Top: Fluence-based criteria from [71] and [24]. Bottom: Instantaneous flux-based criteria from [60] and [53]. 24
2.4 Surface charging risk criteria derived from LANL data. Top: Differential flux threshold (8 keV) from [63]. Bottom: Integral flux thresholds (10–50 keV) from [36]. 26

3.1 Summary of detection results for GLEs 72-77. 41
3.2 Summary of Neutron Count Station Parameters. 43
3.3 Comparison of maximum effective dose rates calculated by AniMAIRE (GCR and GLE modes), NAIRAS, and the Statistical model for GLEs 73, 74, 75, 76, and 77. 46

4.1 Overview of particle flux monitors on GEO satellites. 55
4.2 Combined Correlation Matrix for Electron Flux Measurements. Upper Triangle: Pearson Coefficient (Linear Magnitude). Lower Triangle: Spearman Coefficient (Monotonic Trend). 59

5.1 Results of averaging K for different sets of stations. Corr denotes the Pearson correlation coefficient, % Same K the percentage of values of K that are equal in the comparison, % N($\Delta K \geq 2$) and % N($\Delta K \geq 3$) the percentage of differences greater or equal than 2 and 3 units of K, respectively, in the comparison. 79

List of Symbols

Variable	Description	Units (as used in the work)
CME	coronal mass ejection	–
d	great circle distance	km
D index	D index for radiation dose	–
E	effective dose rate	$\mu Sv/h$
E_{sol}	effective dose rate (solar contribution)	$\mu Sv/h$
EDRS-C	European Data Relay System - C	–
ESA D3S	ESA's Distributed Space Weather Sensor System	–
E scale	SeNMEs's scale for >2 MeV electron flux	–
ESD	electrostatic discharge	–
F	differential particle flux	pfu keV^{-1} = cm^{-2}s^{-1}sr^{-1}keV^{-1}
f	fluence	pfu s^{-1} = cm^{-2}sr^{-1}
FAA	Federal Aviation Administration	–
FMI	Finish Meteorological Institute	–
G scale	NOAA's geomagnetic storms scale	–
GCR	galactic cosmic rays	–
GFZ	Helmholtz Centre for Geosciences	–
GLE	ground level enhancement	–
GOES	Geostationary Operational Environmental Satellite	–
HAPI	Heliophysics API	–
HB	Hotbird	–
HSS	solar wind high speed stream	–
ICAO	International Civil Aviation Organization	–
IMF	interplanetary magnetic field	–
K	geomagnetic disturbance index	–
Kp	planetary geomagnetic disturbance index	–

Variable	Description	Units
K9	value for K = 9 in a station	nT
MPS	Magnetospheric Particle Sensor	–
NGRM	Next Generation Radiation Monitor	–
NM	neutron monitor	–
NMDB	Neutron Monitor Database	–
NOAA	National Oceanic and Atmospheric Administration	–
r	Pearson correlation coefficient	–
R scale	NOAA's radio blackouts scale	–
R_c	geomagnetic cut-off rigidity	GV
S scale	NOAA's solar radiation storms scale	–
SEISS	Space Environment In-Situ Suite	–
SEL	single event latch-up	–
SeNMEs	Servicio Nacional de Meteorología Espacial	–
SEP	solar energetic particles	–
SEU	single event upset	–
SWPC	Space Weather Prediction Center	–
UTC	Coordinated Universal Time	–
λ	geographical longitude	rad / deg
ρ	Spearman correlation coefficient	–
ϕ	integral particle flux	pfu = $cm^{-2}s^{-1}sr^{-1}$
φ	geographical latitude	rad / deg

Acknowledgements

I would like to dedicate this final space to express my sincere gratitude to all those who have enabled the completion of this Master's Thesis.

First of all, I want to thank Professor Pierluigi Di Lizia for his willingness to supervise this work. I truly appreciate his availability and kindness throughout this process. A further thanks must go to Politecnico, where I have enjoyed an outstanding academic and personal experience during these two years, acquiring extensive knowledge of Space Engineering from exceptional professionals and allowing me to turn my passion into a career in the space sector.

I would like to extend my gratitude to GMV for giving me the opportunity to develop this Thesis within the company. From the very beginning, I've been warmly welcomed by the entire team, received support and advice of the highest quality, and felt fully integrated. A very special thank and recognition to Aurora, who has friendly and patiently guided me in carrying out this Thesis, being a fundamental help in every step. Another huge thanks goes to Ángel, who has also been an essential help with his continuous insightful advice and supervision, always noticing the real-time nature of the Thesis, with new Space Weather events happening between meetings.

Finally, I owe everything to my family; they deserve the biggest thank for their unconditional love, their constant support, and every sacrifice they have made to provide me with the best possible life; nothing would have been possible without them. I am also deeply grateful to my friends for their affection and support, from the ones who have been by my side for many years, to the ones that I know from not so long ago but it feels like I've known forever. Last but not least, a special note of gratitude goes to my home university, Universidad de Sevilla, where I began this journey into Aerospace Engineering and where I lived so many unforgettable moments.